Contents

Abstract in English iii
Abstract in Japanese v
Acknowledgement vii
List of figures ix
List of tables xiii

Chapter 1 Introduction 1

1.1 Feeding parts 3
1.2 MEMS based feeding microparts 5
1.3 Feeding micropart by asymmetry 9

Chapter 2 Experimental Systems 11

2.1 Microparts feeders 12
2.2 Microparts movement measurement tool 15
2.3 Analysis of microparts movement using particle tracking velocimetry (PTV) 17
2.3.1 Canny Edge Detector 17
2.3.2 Otsu Thresholding 19
2.3.3 Comparison between Canny and Otsu techniques in PTV method 20
2.4 Characteristic of Obtained Surfaces by Technologies Fabrications 22
2.4.1 Fabricated surface by dicing saw 22
2.4.2 Fabricated surface by grinding process 24
2.4.3 Fabricated surface by femtosecond laser process 25
2.4.4 Fabricated surface by etching process 26
2.5 Closing remarks 29

Chapter 3 Principle of Unidirectional Feeding 31

3.1 Introduction 32
3.2 Microparts surface inspection equipment 32
3.3 Microparts surface characteristics 33
3.4 Contact between microparts and saw-tooth surface 38
3.4.1 Slope contact 38
3.4.2 Point contact 39
3.5 Previous feeding experimental results 39
3.6 Closing remarks 42

Chapter 4 Effect of Asymmetric Patterned Profile on Feeding Velocity 43

4.1 Analysis of real surface profiles using scanning laser microscope system 44
4.2 Effect of asymmetric profile on the motion of micropart 46
4.2.1 Particle Tracking Velocimetry 46
4.2.2 Results 48
4.3 Effect of Exciting Frequency on Motion of Microparts 52
4.4 Closing remarks 56

Chapter 5 Effect of Geometry Parameters of Asymmetric Fabricated Surface on Micropart Feeding 57

5.1 Experiment Validation 58
5.1.1 Experiment Surface 58
5.1.2 Tracking Method 61
5.2 Results and Discussion 62
5.3 Closing remarks 64

Chapter 6 Two-Dimensional Modeling Micropart Feeding on a Saw-tooth Surface with Symmetric Vibration 67

6.1 Dynamic model of micropart on the asymmetric fabricated surface 68
6.1.1 Micropart surface profile model 68
6.1.2 Transition among contact conditions 68
6.1.3 Equation of micropart motion 71
6.1.4 Driving force 72
6.1.5 Surface friction force 74
6.1.6 Air Drag 78
6.2 Numerical Scheme using Matlab software 78
6.3 Comparison of experiments and simulation results 80
6.3.1 Comparison of experiments and simulation with the effect roughness of surface 80
6.3.2 Comparison of experiments and simulation with effect of air drag 83
6.3.2.1 Amplitude of the vibrating saw-tooth surface 83
6.3.2.2 Response of feeding micropart velocity 84
6.4 Closing remarks 87

Chapter 7 Concluding Remarks and Future Work 89

7.1 Concluding remarks 89
7.2 Future work 90
7.2.1 Present research related to research plan 90
7.2.2 Purpose of proposed research 91

Bibliography 93

Abstract

The objective of this thesis is to investigate the dynamic motion of micro-parts such as small electronic devices on symmetrical vibratory saw-tooth patterned surfaces by experiment and simulation, providing the guidelines for the development efficient micro self-assembly systems. This approach depends only upon the contact condition between the feeder surface and the microparts to carry out microparts one direction. So, the driving system is simple and uses an open loop system for feeding.

To move micro-parts in a desired direction is attractive issue since it has wide applications in electronics industry, micro-logistics, and micro-robot industry. In the micro world, friction dominates in the force applied on microparts rather than its inertia due to adhesion and electrostatic force, van der Waal's force, intermolecular force, and surface tension. However, the effect of these forces on the motion of micro-parts has rarely studied with the variation of the driven system and micro-parts parameters. Therefore, this thesis investigates deeply on the effect of geometry parameters of asymmetric surfaces and microparts, actuator parameters of a feeding system, and environment parameters on the motion of micro-parts by both experiment and simulation techniques. The comparison between experiment and simulation that can model above forces allows identifying the important forces and parameters. Thesis is organized as follows:

Chapter 1 provides a review of the existing micro-feeder systems.

Chapter 2 introduces the available experiment systems as well as demonstrating fabrication technologies of experimental saw-tooth surfaces. In this chapter we also introduce particle tracking velocimetry (PTV) method to track micro-parts position with time.

Chapter 3 describes basic principle of one-directional feeding of micro parts along an asymmetric surface driven by symmetric vibration.

Chapter 4 investigates the effect of the saw-tooth profile of surface and exciting frequencies on the motion of micro-parts by experiment. The obtained results show that

micro-parts can move faster on the surfaces which have the patterned profiles closest to the saw-tooth shape.

Chapter 5 studies the effect of relationship between geometry parameters of surfaces and micro-parts on the motion of micro-parts. We found that the velocity profiles of the micro-parts against characteristic velocity of the surface are similar for the same relative length of micro-part to the saw-tooth pitch.

Chapter 6 describes the simulation model of the micro-parts on saw-tooth surfaces. The model includes the effect of surface roughness, relative micro-parts geometry parameters to the surface geometry parameters, adhesion, and environment parameters. The contact between the micro-part and saw-tooth surface is assumed to be at the contact between a number of hemisphere on the micro-part and the surface, resulting in either a point contact or slope contact. The surface roughness is modeled as a random normal vector with a pre-described distribution. The model describes well the motion of micro-parts.

Chapter 7 provides the concluding remarks the thesis and future works.

主　論　文　要　旨

論文内容の要旨

本論文は，のこぎり歯形状を有する非対称表面上のマイクロパーツの運動を，実験やシミュレーションを通して解析することを目的とする．これにより，マイクロパーツの効率的な搬送システムの開発を目指す．提案する手法では，フィーダ表面とマイクロパーツとの接触状態により，マイクロパーツを一方向に搬送することができる．したがって，オープンループの単純な機構で搬送を実現することができる．

マイクロパーツを定められた方向に搬送することは，電子産業や精密産業，マイクロロボットなど広い応用を持つ．マイクロパーツの世界では，慣性力より摩擦力が支配的であり，凝着力，静電力，ファンデルワース力，分子間力，表面張力など様々な力が作用する．しかしながら，これらの力がマイクロパーツの動的な運動においてどのように作用するか，特に搬送システムやマイクロパーツのパラメータにどのように依存するかは，ほとんど知られていない．そこで本論文は，非対称表面やマイクロパーツの幾何パラメータ，搬送システムのアクチュエータのパラメータ，さらに雰囲気のパラメータがマイクロパーツの搬送に与える影響を実験とシミュレーションを通して明らかにする．実験とシミュレーションの結果を比較することにより，マイクロパーツの搬送に支配的な力やパラメータを見い出す．

本論文の構成を以下に示す．

第 1 章では，既存のマイクロパーツ搬送システムについて述べる．

第 2 章では，実験システムについて述べる．さらに，マイクロパーツの運動を計測する手法である粒子追跡流速測定法(PTV)について述べる．

第 3 章では，非対称表面上におけるマイクロパーツの搬送の原理を述べる．

第 4 章では，非対称表面の幾何パラメータと表面の駆動周波数がマイクロパーツの運動に与える影響を実験的に調べた結果を示す．実験結果より，のこぎり歯形状に近い表面上で，マイクロパーツは速く運動することがわかった．

第 5 章では，非対称表面とマイクロパーツの幾何パラメータが，マイクロパーツの運動に与える影響を述べる．マイクロパーツの搬送速度と表面の速度の関係が，マイクロパーツの寸法とのこぎり歯のピッチの関係で表されることを示す．

第 6 章では，のこぎり歯表面上のマイクロパーツの運動のシミュレーションモデルについて述べる．提案するモデルは，表面粗さ，マイクロパーツと表面の幾何パラメータ，凝着力，雰囲気のパラメータを有する．マイクロパーツとのこぎり歯表面との接触を，パーツの表面を表す有限個の半球と表面との接触で表す．このとき，個々の半球と表面との接触は，点接触か斜面接触で表される．表面の法線方向を確率的な分布を有するベクトルで表すことにより，表面粗さをモデル化する．提案するモデルは，マイクロパーツの運動を良く表現することができる．

第 7 章では，結論と今後の課題を述べる

Abstract in Japanese

Acknowledgement

This research was granted by Japanese Government (Monbukagakusho: MEXT) scholarship program.

This thesis grew up from the indispensable support of my supervisor professor Shinichi Hirai. I would like to take this opportunity to express my sincerest appreciation to him for his guidance in the completion of my thesis. The sincerest gratitude goes to him for conducting me to microparts feeding, for worthy research discussions. He always encourages us as well as to make creatively working ambience, sufficient convenience for research. Without his assistance and persistent help this thesis would not have been possible.

I would like to acknowledge to Dr. Atsushi Mitani for cooperation with me, and for sharing his model regarding dynamic micropart motion.

I am particularly indebted to Dr. Xuan Thien Dinh for contributing valuable ideas in our work. Many ideas become transparent after conversations with him.

Further I desire to show appreciation to all my colleagues in my own Integrated Machine Intelligence Lab. for the very good atmosphere as well as for the fruitful scientific discussions. They also helped on using computer systems and on discovery Japanese life, but particularly to Ms Hatanaka, a lovely secretary, who help me a lot with purchase of experimental devices, documents.

Lastly, I am grateful to my parents who have given support throughout my life. Without their helps, my achievements had become impossible.

Acknowledgement

List of figures

Figure 1.1 Vibratory Bowl Feeders 4

Figure 1.2 Sensorless parts orienting using programmable force fields: the part reaches unique orientation after two subsequent squeezes. There exist such orientating strategies for all polygonal partsFeeder systems to transport parts in linear direction were also developed (Barnes *et al.*, 1992; Frei *et al.* 2002). 4

Figure 1.3 Setup for superconducting magnetic levitation, actuation and magnetic sensing 5

Figure 1.4 General structure of MEMS-based actuator array for air-flow distributed micromanipulation 6

Figure 1.5 a) Electric field vector W traveling across a dielectric particle with velocity vE and position of the included dipole moment P describing the localization of induced charges (+, -). The force (F) leads to particle motion (v) contrary to the f 6

Figure 1.6 Feeder using inertial force: Feeder by inertial force. (Left) Simulation of the displacement of the table along the X direction, (Right) photography of the feeder and his hight voltage piezoelectric actuator 7

Figure 1.7 The sound field in the fluid gap 7

Figure 1.8 Piezoelectric vibratory conveyor 8

Figure 1.9 a) A point fixed to the surface is at x_S relative to a fixed point in the world, and the part is at x_p. Gravity holds the part to the surface. b) Experimental setup 9

Figure 1.10 Diagram of a micropart feeder with a saw-toothed surface and symmetric vibrations 10

Figure 2.1 (a) Microparts feeder system using accumulated piezoelectric actuator, (b) schematizes the driving system 13

Figure 2.2 (a) Microparts feeder system using a couple bimorph piezoelectric actuators, 14

Figure 2.3 Difference between two systems: accumulated piezoelectric actuator and bimorph piezoelectric actuator. 14

Figure 2.4 Experiment system: (a) function generator and power amplifier, (b) microscope, (c) feeding system and (d) a typical micropart. 15

List of figures

Figure 2.5 (a) The laser microscope system, (b) The microscope system 17

Figure 2.6 Procedure for detecting center of micro – parts: (a) row image, (b) improved image, (c) edge detection by Canny method, and (d) tracked center. 18

Figure 2.7 Procedure for detecting position and rotation of microparts: (a) raw image, (b) tracked center. 19

Figure 2.8 a) Original image, b) Edge detection by Otsu technique, c) Edge detection by Canny technique 21

Figure 2.9 Two types of surface profiles of a silicon wafer. 22

Figure 2.10 A typical diamond blade for saw-tooth process. 23

Figure 2.11 Saw-toothed silicon wafers fabricated by a dicing saw 23

Figure 2.12 Microscopic image of a sawtoothed surface fabricated by a dicing saw with a bevel type blade: 3D image synthesized from focusing images by height, and colored contour model 23

Figure 2.13 A grooving blade 24

Figure 2.14 Profile of fabricated surface by grinding process on cemented carbide material 24

Figure 2.15 Microfabricated surface profile seen in atomic force microscope 25

Figure 2.16 Microfabricated surface periodicity 26

Figure 2.17 Microscopic image of a sawtoothed surface fabricated by the anisotropic ething process of [221] oriantation silicon wafer 27

Figure 2.18 Remained resist film on thee anisotropic etched process 28

Figure 2.20 3D analysis model of asymmetric etched surface and their sections of three arbitrary points 29

Figure 3.1 Microscopy raw image of ceramic chip capacitors: (a) 0402-, (b) 0603-, and (c) 2012- capacitors 33

Figure 3.2 Measurement results 3D contour line of electrode of ceramic chip capacitors: (a) 0402-, (b) 0603-, and 2012- capacitors 35

Figure 3.3 Measured section of capacitors: (a) 0402-, 0603-, and 2012- capacitors 36

Figure 3.4 Micropart surface model 36

Figure 3.5 Saw-tooth surface model 37

Figure 3.6 Two contacts between a micropart and a saw-tooth 37

Figure 3.7 Diagram of a micropart feeder with a sawtoothed surface and symmetric vibrations 37

List of figures

Figure 3.8 Statics of each contact condition 38

Figure 3.9 Experiment table set up for 2012-capacitors 40

Figure 3.10 Motion of the 2012-type capacitors due to a 10 Hz on a $\theta = 30^0$ surface 41

Figure 3.11 Motion of the 2012-type capacitors due to a 15 Hz on a $\theta = 30^0$ surface 41

Figure 3.12 Motion of the 2012-type capacitors due to a 30 Hz on a $\theta = 30^0$ surface 41

Figure 3.13 Motion of the 2012-type capacitors due to a 15 Hz on a $\theta = 60^0$surface 42

Figure 4.1 Ideal saw-tooth profile of surface 44

Figure 4.2 Microphotograph and profile of saw-toothed fabricated surfaces 45

Figure 4.3 Examples experimental tracking center of micropart (a) improved image, (b) tracking center 48

Figure 4.4 Variation in micropart velocity with time 50

Figure 4.5 Spectrum of x-velocity on brass (a), carbide (b), and zirconia (c) surfaces 51

Figure 4.6 Variations in micropart displacement with time 52

Figure 4.7 Probability distribution of micropart velocity 54

Figure 4.8 The standard deviation of velocity along x-direction at different frequencies 55

Figure 4.9 Displacement along z-direction at different frequencies 55

Figure 5.1 Experimental surfaces and profiles with different saw-tooth pitches, p 59

Figure 5.2 Examples experimental tracking center of microparts, (a) improved image, (b) tracking center. 61

Figure 5.3 The variation of micropart velocity with analysis feeding microparts for the same value of ratio l/p = 4 runs with frequencies 63

Figure 5.4 The variation of micropart velocity with analysis feeding microparts for the same value of ratio l/p = 10 runs with frequencies 63

Figure 5.5 The variation of micropart velocity with analysis feeding microparts for the same value of ratio l/p = 20 runs with frequencies 64

Figure 5.6 Diagram of individual asymmetrical force on a micropart 64

Figure 6.1 Model of 2012 capacitor 68

Figure 6.2 Contacts of a convexity and two saw-teeth 70

Figure 6.3 Coordinates of micropart transferred from hemispheres 71

Figure 6.4 Pseudo vector field normal to saw-tooth surface 73

Figure 6.5 Saw-tooth surface 73

List of figures

Figure 6.6 Cross section of the fabricated surface 76

Figure 6.7 Adhesion friction model 77

Figure 6.8 Model of adhesion force on saw-tooth 77

Figure 6.9 Approximate saw-tooth profile; dashed red line represents ideal saw profile; solid black line represents real saw-tooth profile approximated by adding white noise to ideal profile 78

Figure 6.10 Flow chart for simulation of micropart motion 79

Figure 6.11 Velocity of micropart x-component with respect to time 81

Figure 6.12 Spectrum of velocity along x-direction 81

Figure 6.13 Ensemble averaged displacement of micropart with respect to time 82

Figure 6.14 Ensemble averaged rotation angle of micropart in (x,y) plane 82

Figure 6.15 The experimental amplitude with time at 100 Hz 85

Figure 6.16 The spectrum of x displacement with frequencies at 100 Hz 85

Figure 6.17 The experiment amplitude for range of frequency 86

Figure 6.18 Variation of ensemble average velocity of micropart with frequency for *l/p* = 4 86

Figure 6.19 Variation of ensemble average velocity of microparts with frequency for *l/p* = 10 87

Figure 7.1 Automatic assembly system in industry 92

Figure 7.2 Development of multiple functional surfaces for microparts feeder with simple planar symmetric vibration. 92

List of tables

Table 2.1 TDK C-Series Specifications 16

Table 5.1 Relative scale with different saw-tooth pitches 60

Table 6.1 Transition of contact force 69

List of tables

Chapter 1

Introduction and Related Work

The objective of this thesis is to investigate the motion of microparts on symmetrical vibratory saw-tooth patterned surfaces by experiment and simulation and then, provides the guidelines to develop efficient micro self-assembly systems.

To move microparts in a desired direction is attractive issue since it has wide applications such as electronics industry, micro-logistics, micro-robot industry, and particular self-assembly in micro-world. The term "self-assembly" has been applied for the manufacture of systems incorporating large numbers of micro-devices. The principle to move parts often encompasses vibration in combination with electrostatic, fluidic, and other forces. In the micro world, the force on micropart includes not only inertia but also friction due to adhesion and electrostatic force, van der Waal's force, intermolecular force, and surface tension (Y. Komari, 1993). However, the effect of these forces on the motion of microparts has rarely studied with the variation of the driven system and microparts parameters. Therefore, this thesis investigates deeply on the effect of geometry parameters, actuator parameters, and environment parameters on the motion of microparts by both experiment and simulation technique. The comparison between experiment and simulation which can model above forces and parameters allows identifying the important forces and parameters. The procedure of this thesis is step by step described in seven chapters as bellow.

Chapter 1 gives a review of the existing micro-feeder systems.

Chapter 2 introduces the available experiment systems in our Robotic Laboratory at Ritsumeikan University and Design Laboratory at Sapporo City University. In this chapter we also introduce particle tracking velocimetry (PTV) method to track microparts position with time.

In chapter 3 describes the basic principle of the asymmetric fabricated surfaces.

Chapter 4 investigates the effect of the saw-tooth profile of surface and exciting frequencies on the motion of microparts by experiment. The obtained results show that microparts can move better on the surfaces which have the patterned profiles closest to the saw-tooth shape.

Chapter 5 studies the effect of relative microparts geometry to the surface geometry on the motion of microparts. We found that the velocity profiles of the microparts against characteristic velocity of the surface are similar for the same relative length of micropart to the saw-tooth pitch.

Chapter 6 describes the simulation model of the microparts on saw-tooth surfaces. The model includes the effect of surface roughness, relative microparts geometry parameters to the surface geometry parameters, adhesion, and environment parameters. The contact between the micropart and saw-tooth surface is assumed to be the contact between a number of hemisphere on the micropart and the surface, which results in either a point contact or slope contact. The surface roughness is modeled as a random normal vector with a pre-described distribution. The model describes well the motion of microparts.

Chapter 7 provides the concluding remarks the thesis and future works.

1.1 Feeding parts

Many industrial applications require part feeder to sorting, arranging, and moving a large number of parts automatically to a desired target at a certain time. For example, in automatic assembly, the orientation and position of the parts are important because the parts have to be aligned in a desired orientation before assembly processes (Ngoi *et al.*, 1995).

Moreover, feeder systems using vibratory mechanism can be used to check the cracks and other defects of the parts. Therefore, feeding parts have been widely studied with various principles to feed parts.

The most popular feeder was the vibratory bowl-type which has been found in many applications such as automobile, pharmacy, cosmetics, electronics, fasteners and plastics, to sort and orient parts before assembly (Maul *et al.*, 1997; Okabe *et al.*, 1981; and Morrey *et al.*, 1986) (Fig. 1.1). A typical vibratory bowl feeder consists of a bowl mounted on a base by three or four inclined leaf springs. An electromagnet is placed between the base and bowl. The bowl travels vertically and twists about the vertical axis by the constrain of the springs and the electromagnetic force between the bowl and the electromagnet. Parts are conveyed in the bowl by one of two modes: sliding and hopping. In the sliding mode, the motion of part is produced from friction between the part and the bowl. As the bowl rises and twists forward, the friction between the track and part drives the part forward with the track. When the track descends and twists backward, the friction is lessened, so the part moves less backward. In the hopping mode, part moves forward with the bowl as the bowl rises and twists, but the part falls freely when the bowl moves downward with the acceleration exceeding the gravity.

Levy (2001) studied further on the conveyor feeders by considering mathematical models to evaluate the probability distributions of the natural resting aspects of prismatic parts in a bowl feeder. The models were applied to study the motion of prismatic parts in square, cylindrical, triangular, hexagonal, rectangular, and symmetrical and asymmetrical T shapes. The models were also applied to analyze three different terminal connectors. The analytical results were agreed well with experimental data in the drop test results.

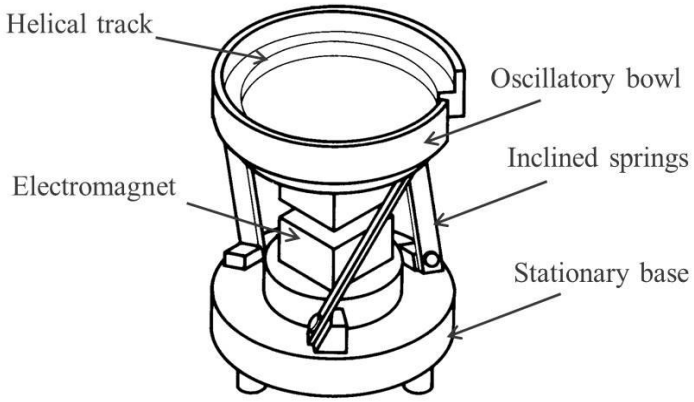

Figure 1.1 Vibratory Bowl Feeders

Another conveyor feeder principle relies on the idea of "distributed manipulation" (Bohringer *et al.*, 2000). In this principle, the feeder consists of a large number of simple structure manipulators (Fig. 1.2). Each manipulator is capable to move part to the neighbor. Successively, the part can be transported in a simple and inexpensive way.

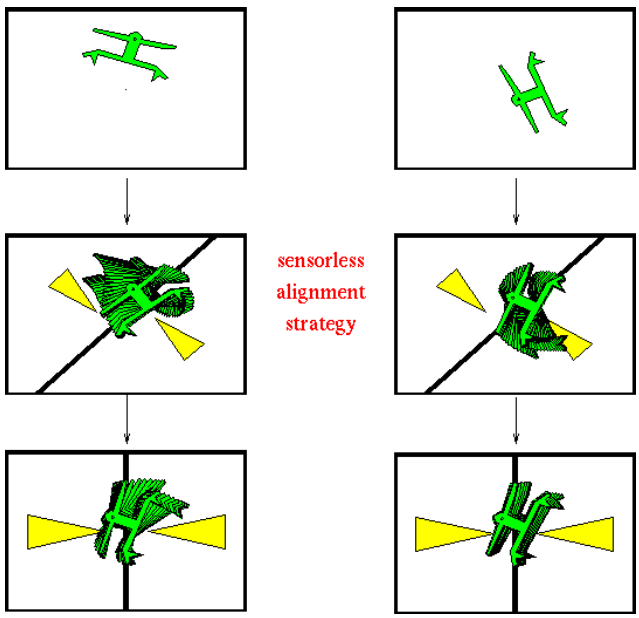

Figure 1.2 Sensorless parts orienting using programmable force fields: the part reaches unique orientation after two subsequent squeezes. There exist such orientating strategies for all polygonal partsFeeder systems to transport parts in linear direction were also developed (Barnes *et al.*, 1992; Frei *et al.* 2002).

In these feeders, the surfaces were oscillated in two directions: vertical and horizontal directions. The aspect ratio of the horizontal/vertical oscillation amplitude was controlled to prevent the parts from jumping.

1.2 MEMS based feeding microparts

Recently, parts to assembly devices have been down scaled into sub-millimeter scale since the devices is required to compact to save consumption energy. Fortunately, with the development of MEMS technology, various principles for micro scaled parts are available such as magnetic, pneumatic, ciliary, and ultrasonic feeder.

Komari *et al.* (1993) reported a feeder for microparts with an array of linear actuators. The actuators were actuated by superconducting magnetic levitation (Fig. 1.3). The movement of the linear actuators was limited to one direction because almost of the actuators can have linear guides. Later, Iisuka *et al.* (1994) improved the design of the actuators that allows the actuators moving in two linear directions and rotation. In this design, the stator layer is planar distributed under the slider. This feeder system provides a smooth linear and rotating motion with high resolution.

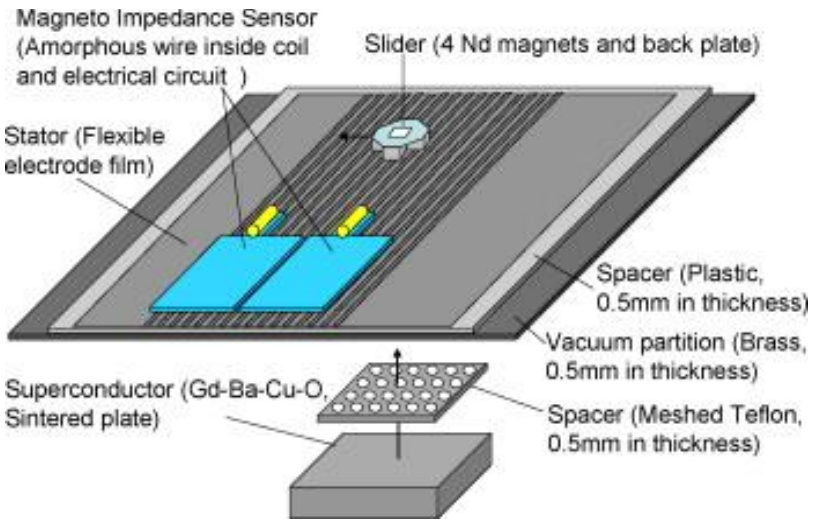

Figure 1.3 Setup for superconducting magnetic levitation, actuation and magnetic sensing

In pneumatic feeders, air flows are used to transport microparts. MEMS technology was used to mount on planar board arrays of micro sized nozzles that, by turning on or off air flow, can control the direction of the moving microparts (Konish *et al.*, 1994-1999, Arai *et al.*, 2002). The advantages of this type of feeder are frictionless and large force on the parts. Therefore, various MEMS feeder have been developed. Fukuta *et al.* (2006) presented a pneumatic feeder composed of an array of micro actuators which can be realized by bulk MEMS technology.

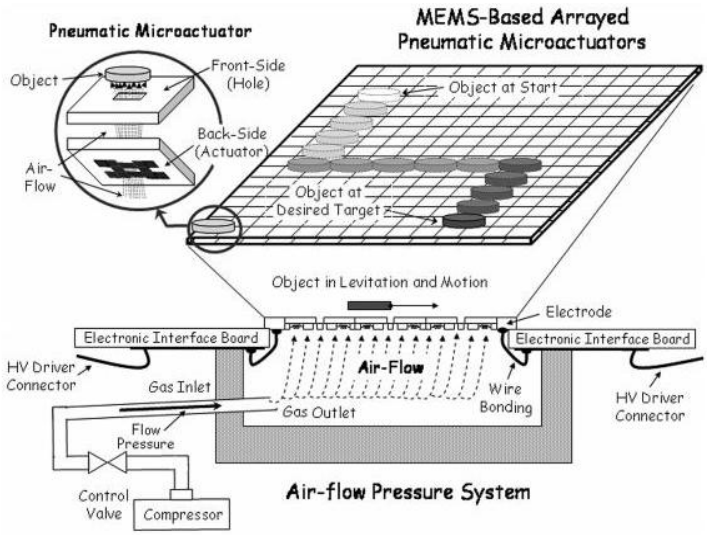

Figure 1.4 General structure of MEMS-based actuator array for air-flow distributed micromanipulation

At the top level, the authors found the MEMS layer based on pneumatic microactuator. The second level represents the microsensor layer to detect positions of the object. Finally, all sensor information is addressed and proceeds at the microcontroller level to drive the distributed MEMS surface.

The method of using electric fields for feeding microparts has been discussed numerous literatures (Flix *et al.*, 1999). In G. Fuhr *et al.* (1995) work, the mechanism to move micro particles was similar to a dielectric induction motor. Depending on the passive electric properties of the particle and the surrounding medium, two cases of polarization could occur (Fig. 1.5 a, b) and consequently the particle moves in or contrary to the direction of electric field motion, respectively.

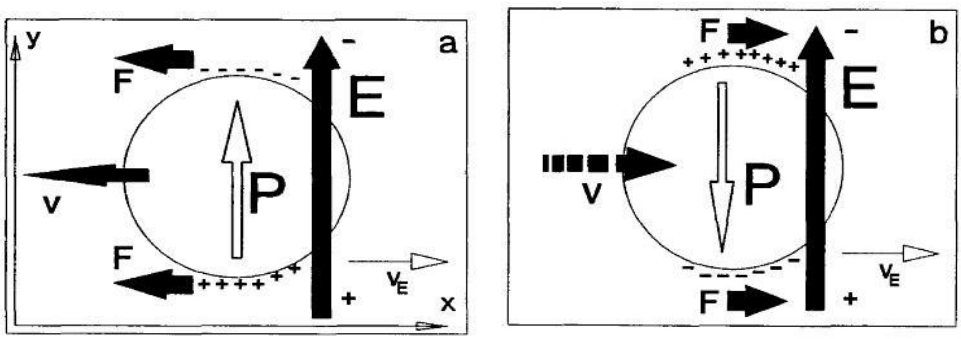

Figure 1.5 a) Electric field vector W traveling across a dielectric particle with velocity vE and position of the included dipole moment P describing the localization of induced charges (+, -). The force (F) leads to particle motion (v) contrary to the f

Paris *et al.*, (2008) presented the concept of the feeding by inertial force. His approach was based on control mechanical vibrations in order to move the microparts. These vibrations allowed breaking adhesion and friction (Fig. 1.6). To control the displacement they have used the Input Shaping technique. After identification of the dynamic behavior of the moving table, the time delays and the amplitudes of impulses have been calculated. The feeder allowed to reduce the residual vibrations and then controlled the acceleration of the feeder.

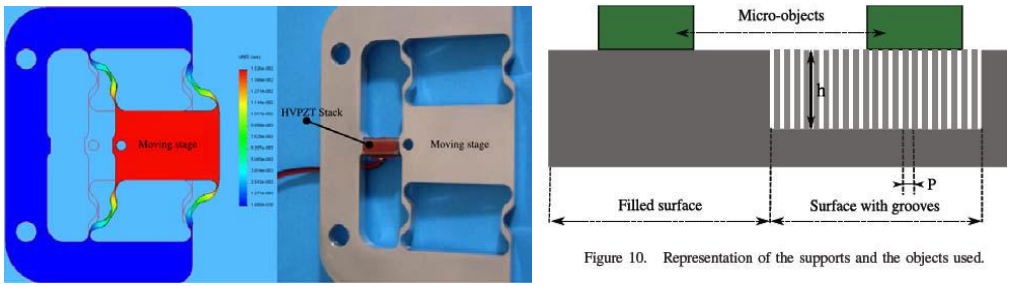

Figure 1.6 Feeder using inertial force: Feeder by inertial force. (Left) Simulation of the displacement of the table along the X direction, (Right) photography of the feeder and his hight voltage piezoelectric actuator

Another method to transport microparts is using ultrasonic force. The general principle of ultrasonic feeder was explained in detail in (E. Benes *et al.*, 2005, Haake *et al.*, 2003). A vibrating plane emitted ultrasonic sound that was reflected at another rigid plane (Fig. 1.7). Depending on the surface movement of the emitting plane, a two- or three-dimensional standing sound field was built up between these two planes. With this sound field, it was possible to position small particles in one or two dimensions and to hold them in an equilibrium position in the vertical direction. By changing the sound field the microparts can be moved.

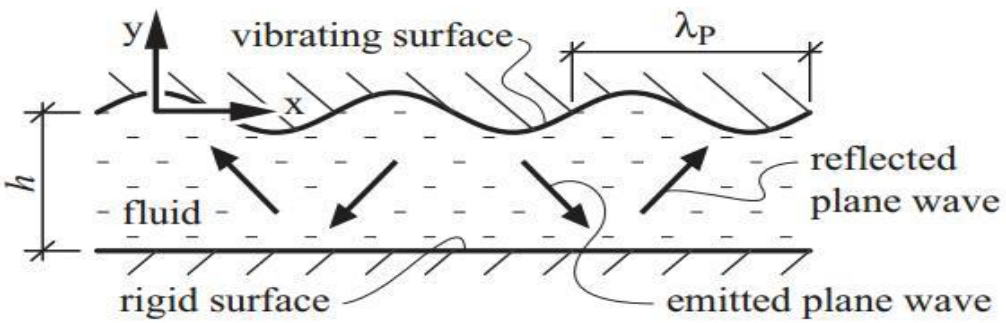

Figure 1.7 The sound field in the fluid gap

Other systems used the concept of ciliary actuator. Suh *et al.*, (1999) described a first functional ciliary actuator array integrated with CMOS circuitry. The actuator's tip can deflect and then lift microparts. The overall architecture of the chip and supporting hardware allow moving microparts.

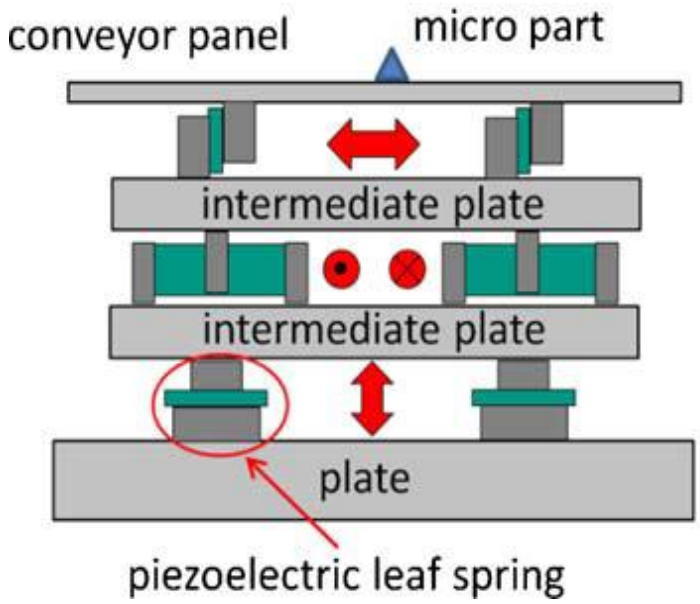

Figure 1.8 Piezoelectric vibratory conveyor

Fleisccher *et al.*, (2011) presented a multi body simulation model describing the micro slide principle including all major influencing parameters for microparts. The model of the feeder included three actuator systems to elevate and transport microparts as shown in Fig. 1.9. Depending on the type of the superimposition of the three oscillations, it was possible to transport micropart on the feeder surface in good agreement with a pre-determined path.

Finally, various feeding system using superconducting (Kim *et al.*, 1989), bimorph piezoelectric actuators (Chang *et al.*, 2000, Ting *et al.*, 2002-2005), and inchworm systems (Zesch *et al.*, 1995, Higuchi *et al.*, 1990, and Codourey *et al.*, 1995) have been developed. Research topics have included the effects of the surface contamination of tracks on feeding (Francisco *et al.*, 1991), traps designed for the alignment (Berretty *et al.*, 1999), and solutions to models to describe the touching or overlapping parts (Maul *et al.*, 1994).

1.3 Feeding micropart by asymmetry

In order to reduce the complex in control of a feeder, asymmetry pattern of the feeder surface or linear vibration of the feeder was considered. There were three pattern asymmetries.

First principle was fast/slow driving of a plane in the horizontal plane in which the asymmetry was time of slipping in one direction versus another to create a net impulse on microparts in one cycle. By using this principle, microparts could move in different directions on the one-degree-of-freedom linear conveyors (Okabe *et al.* 1985, Umbanhowarp *et al.*, 2008) and a planar shaker plate (Reznik *et al.* 1998-2011). Okabe *et al.* (1985) studied to find a periodic longitudinal waveform of an inclined surface that maximized the speed of the microparts. They used a finite parameterization of the waveform and conducted numerical simulation to provide the guidelines for the choice of these parameters. Umbanhowarp *et al.*, (2008) incorporated acceleration constraints and solved exactly the optimal driving waveform without parameterization. Consequently, they could drive an optimal feeding motion in both the horizontal and vertical directions.

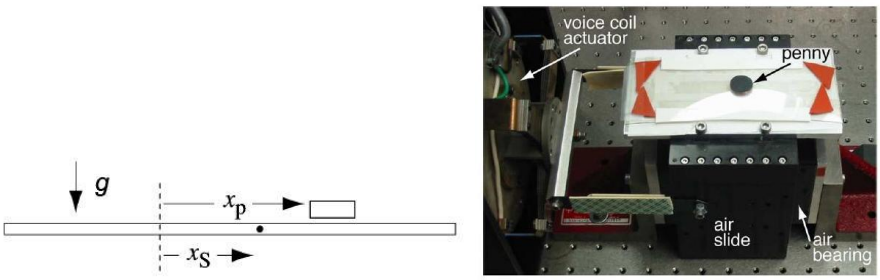

Figure 1.9 a) A point fixed to the surface is at x_S relative to a fixed point in the world, and the part is at x_p. Gravity holds the part to the surface. b) Experimental setup

The second principle was similar to the first principle. However, the asymmetric friction force lied on the asymmetric normal force between the microparts and feeder surface in one cycle of the vibration. The vibrating feeder surface was generated the horizontal plane (x-y-yaw) and out of the horizontal plane (z-roll-pitch) (Umbanhowarp *et al.*, 2008-2012; Boothroyd *et al.* 2005; and Peter *et al.*, 2000). In this type of feeder, the asymmetrical normal force arises due to the time-dependent out-of-plane acceleration.

The third principle was anisotropic texture of the feeder surface. Mitani *et al.*, (2006-2011) proposed a micropart feeder that has saw-tooth profile texture on the feeder surface. The microparts can move in one direction with simple horizontal sinusoidal oscillation of the feeder (Fig. 1.10). His study was carried out for various saw-tooth geometry parameters and exciting frequencies. They also examined the motion of microparts on different profiles of the asymmetric structure which are achieved by the ability of fabricated technologies. However, his study method was unable to study the dynamics of the microparts. In addition, the results were reported case by case without systematical conclusion.

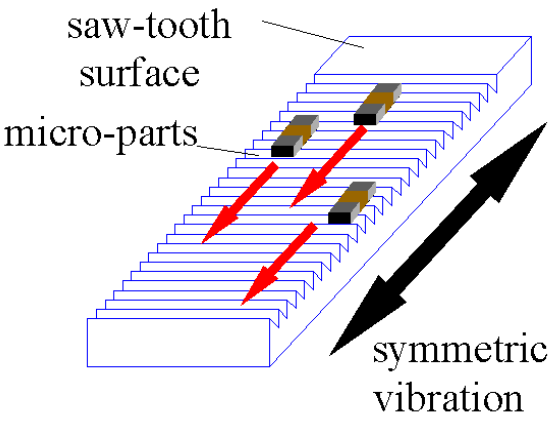

Figure 1.10 Diagram of a micropart feeder with a saw-toothed surface and symmetric vibrations

This thesis will focus on the third principle to move microparts in a desired direction, since this principle is simple and then easily to integrate to a self-autoassembly system. The thesis will systematically investigate the effect of the geometry parameters of the feeder surface, actuator parameters, and environment parameters on the motion of microparts by both experiment and simulation techniques. The experiment technique will be considered in the way that we can observe time-dependent motion and dynamics of the microparts. Simulation technique focuses on the uncertain effects in micro-world such as the effect of the feeder surface roughness no the motion of the microparts.

Chapter 2

Experimental Systems

This chapter introduces the experiment system as well as analyzes the microparts movement by using particle tracking velocimetry (PTV) method. In order to drive microparts feeder table, the accumulated piezoelectric actuator and the bimorph piezoelectric actuator are used. Because in the previous relative works, the moving microparts were recorded for a distance and then the micropart velocity was measured as time averaged velocity on this distance. Therefore, it could not observe the dynamic motion of the microparts. In this thesis particle tracking velocimetry (PTV) is used to determine the time-dependent velocity of the microparts. Two techniques, Canny edge detection and Otsu thresholding, to detect the position of the microparts are discussed. Moreover, the technologies to fabricate the saw-tooth surfaces including dicing saw process, grinding process, femtosecond laser process, and etching process are introduced in Section 2.4.

2.1 Microparts feeders

The piezoelectric actuator (PZT) is a well-known commercially available device for managing extremely small displacements in the range of 10 pm (1 pm $= 10^{-12}$ m) to 100 μm (Adriaens H,. *al et*, 2000). A PZT actuator is an electromechanical device that undergoes a dimensional change when voltage is applied. The conversion of electrical energy into mechanical energy takes place without generating any significant magnetic field or need for moving electrical contacts. Dimensional changes are proportional to the applied voltage and can therefore be adjusted with extremely high resolution. PZT actuators can be operated over millions of cycles without wear or deterioration. Their high response speed is limited only by the inertia of the object being moved and the output capability of the electronic driver. Figure 2.1, 2.2 shows photos of the micro – parts feeding system driven by accumulated piezoelectric actuator and bimorph piezoelectric actuators.

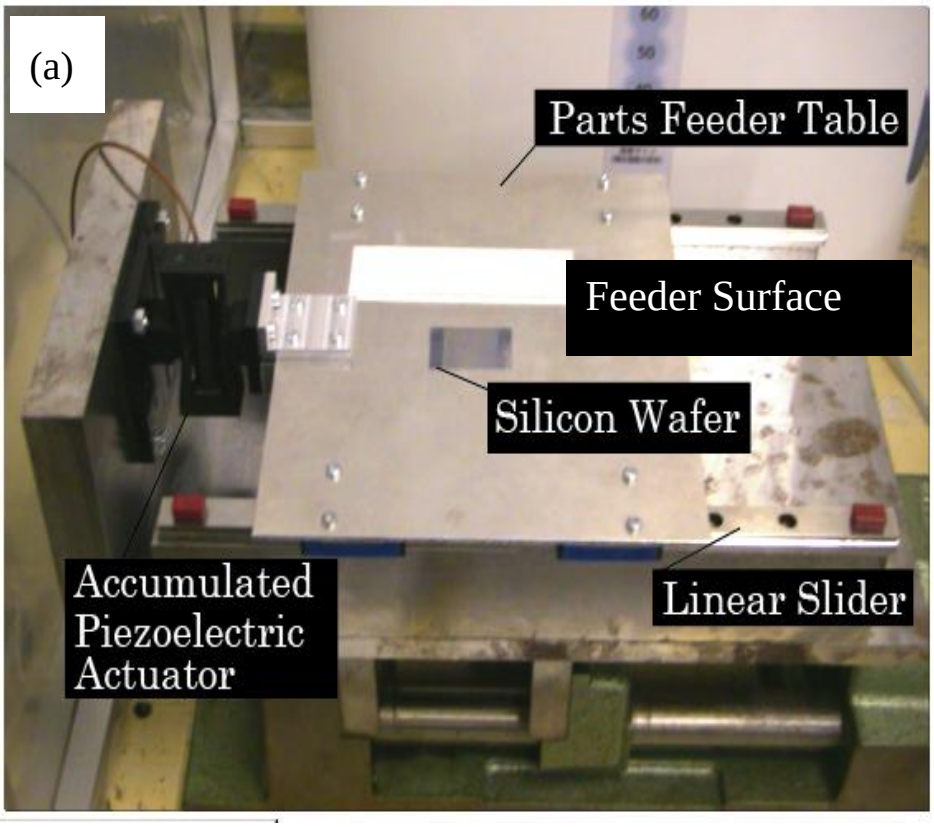

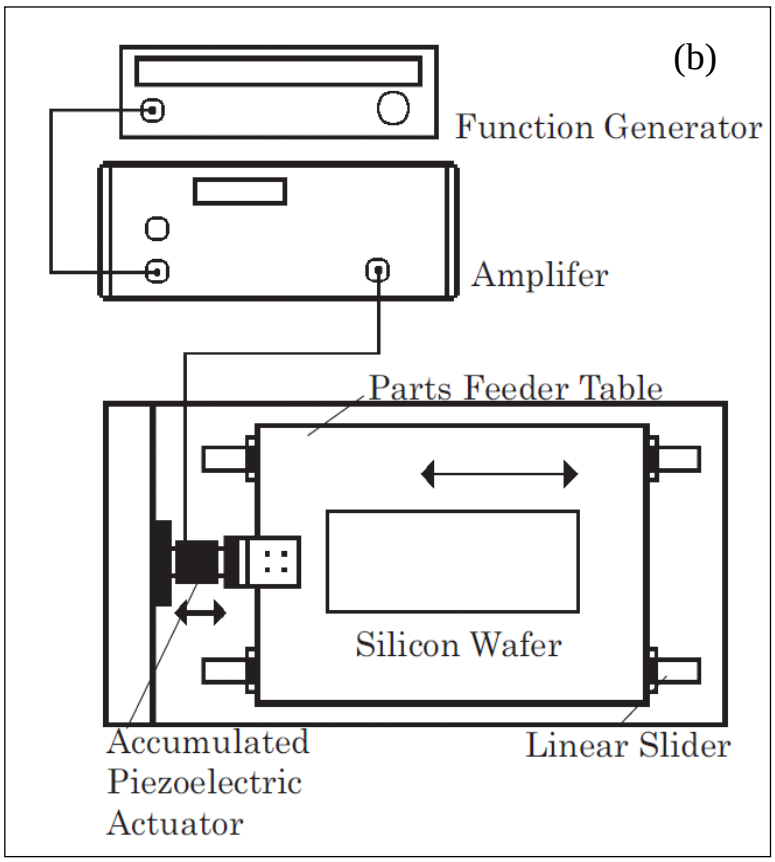

Figure 2.1 (a) Microparts feeder system using accumulated piezoelectric actuator, (b) schematizes the driving system

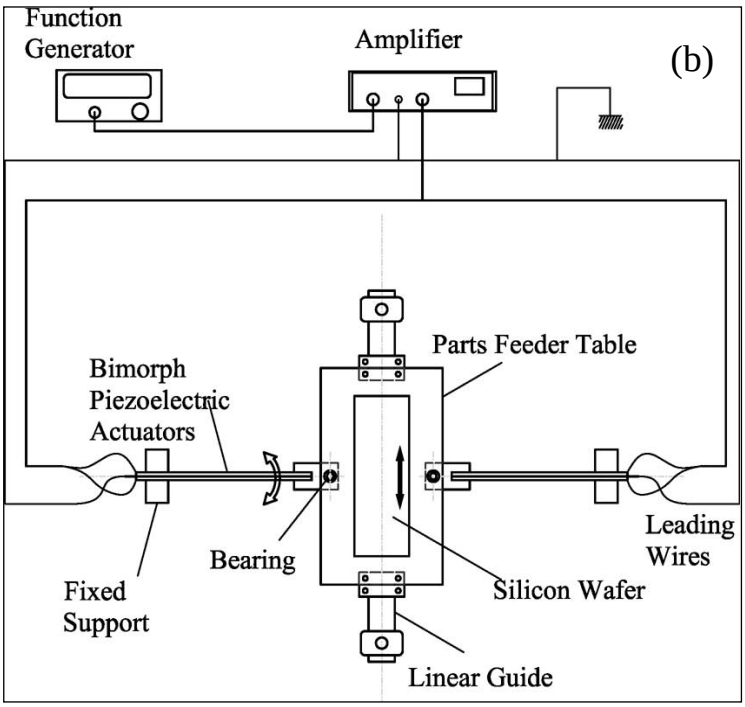

Figure 2.2 (a) Microparts feeder system using a couple bimorph piezoelectric actuators,

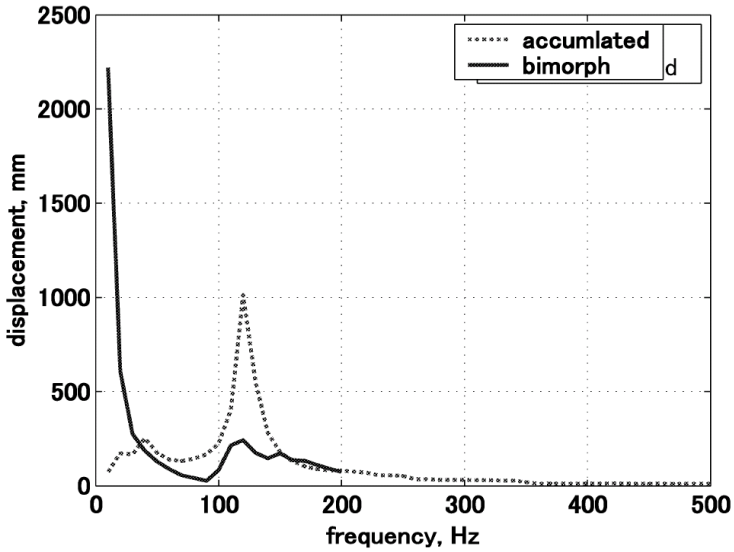

Figure 2.3 Difference between two systems: accumulated piezoelectric actuator and bimorph piezoelectric actuator.

Figure 2.3 shows that the accumulated piezoelectric actuator is good for high frequency but low hysteresis while the bimorph is good for low frequency driving but large hysteresis and bad thermal characteristics.

2.2 Microparts movement measurement tool

The experimental feeding system includes a saw – tooth surface attached to a vibratory table, a function generator, an amplifier, and a microscope (VH – Z20R, Keyence), as shown in Fig. 2.4. The microscope is connected to a variable magnification lens, providing a 20 mm × 200 mm field of view. The lens is adjustable in three directions and perpendicularly oriented to the saw–tooth surface. The vibratory table is horizontally oscillated by a piezoelectric actuator. The actuator is driven by the function generator through the amplifier, which can supply a square/sinusoidal wave with a peak-to-peak output voltage of up to 300 V.

Figure 2.4(a) shows a typical sample of the C – series ceramic chip capacitors (TDK Inc.), which is used as the micro – part in the present study. The micro – parts employed in our study are 2012-, 1608-, 1005-, 0603-, and 0402- type capacitors; the dimensions and weights of these microparts are specified in Table 2.1.

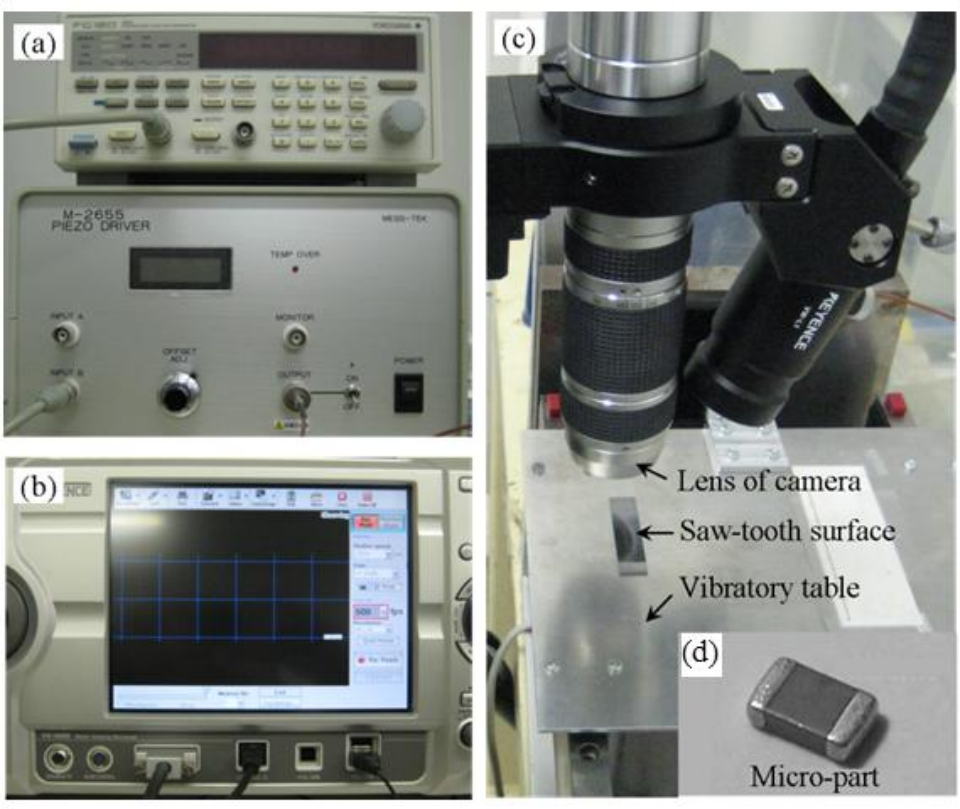

Figure 2.4 Experiment system: (a) function generator and power amplifier, (b) microscope, (c) feeding system and (d) a typical micropart.

Table 2.1 TDK C-Series Specifications

Type	Size (l × w × h [mm^3])	Mass [mg]
2012	2.0 × 1.2 × 0.6	7.5
1608	1.6 × 0.8 × 0.8	1.2
1005	1.0 × 0.5× 0.5	1.2
0603	0.6 × 0.3 × 0.3	0.3
0402	0.4× 0.2× 0.2	0.1

Inspection each surface using a scanning laser microscope system HD100D (Lasertec Corp.), and a microscope system as shown in Fig. 2.5 (a) – (b), we obtained microphotograph of the saw-toothed fabricated surfaces as well as their surface profile model of each surface and also measurement the real profile of ceramic chip capacitors which will be discussed in the next Chapters.

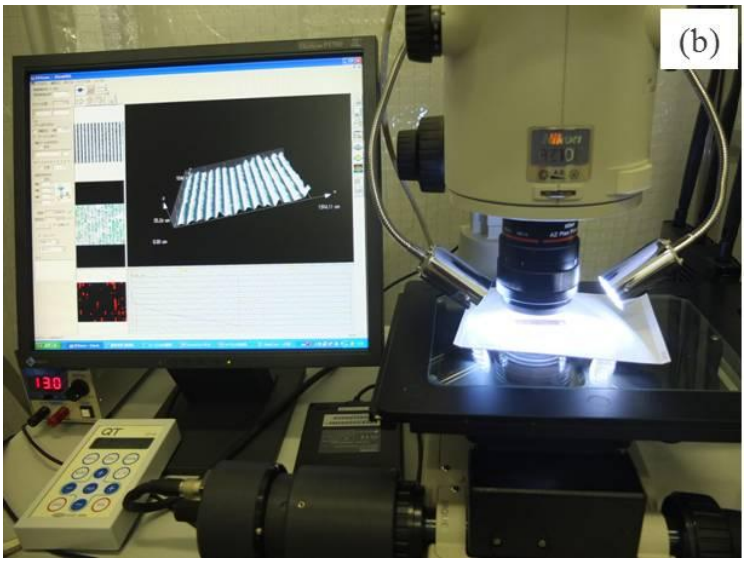

Figure 2.5 (a) The laser microscope system, (b) The microscope system

2.3 Analysis of microparts movement using particle tracking velocimetry (PTV)

PTV determines the (Lagrangian) velocity by measuring the displacement of particle images over a well known period of time. The velocity is computed by dividing the distance between the particle pairs by the time interval. This Largrangian velocity of the particles is often used to represent the instantaneous Eulerian velocity. Particle Tracking Velocimetry is a fast and simple method. In our research presents two techniques of image segmentation to facilitate mage edge detection, that can be used further by image analysis based on the extracted features of image edges, Canny edge detection and Otsu threshold are examples of the proposed techniques. Depending on the quality of the recorded movie, the appropriate technique will be chosen.

2.3.1 Canny Edge Detector

The Canny edge detector is a popular method for detecting edges that begins smoothing an image by convolving it with a Gaussian of a given sigma value. Based on the smoothed image, derivatives in both the *x* and *y* direction are computed, these in turn are used to compute the gradient magnitude of the image. Once the gradient magnitude of the image has been computed, a process called “non maximum suppression” is performed; in which pixels are suppressed not constitute a local maximum. The final

step in the Canny edge detector is the hysteresis operator, in which pixels are marked as either edges, non-edges and in-between, this is done based on threshold values. The next step is to consider each of the pixels that are in-between, if they are connected to edge pixels these are marked as edge pixels as well. The result of this edge detector is a binary image in which the white pixels closely approximate the true edges of the original image.

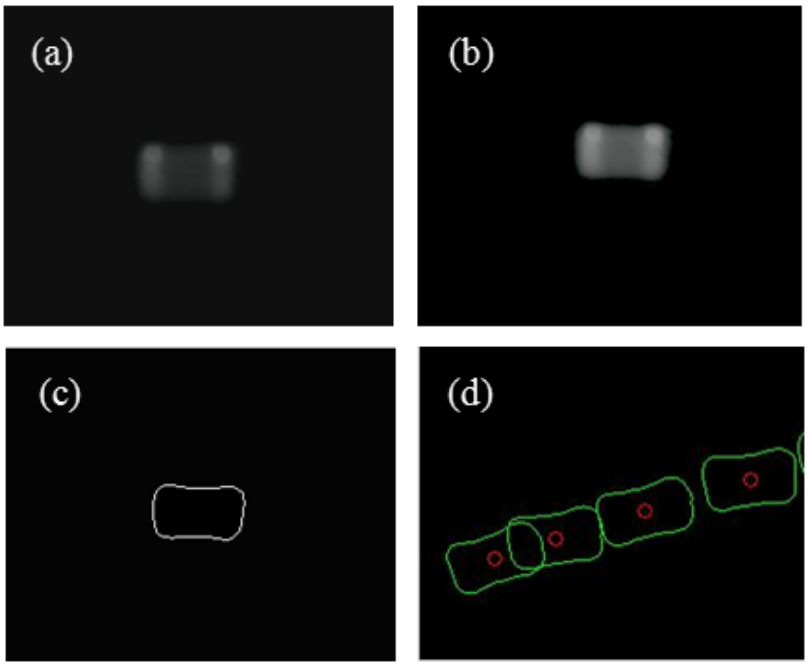

Figure 2.6 Procedure for detecting center of micro – parts: (a) row image, (b) improved image, (c) edge detection by Canny method, and (d) tracked center.

The steps for using the PTV technique in this study are explained in Fig. 2.6. First, a series of images of the motion of a micropart are recorded by the microscope within the focused region of the lens. The raw image shown in Fig. 2.6(a) is extracted from the recorded image series, and its quality is improved as in Fig. 2.6(b) by using image editor software (VW-H1ME, Keygence Co.). Next, the edge of the microparts is detected by Canny method using an approximated threshold defined relatively to the maximum intensity of picture. Fig. 2.6 (c) shows a plot of the edge of the microparts for different value of threshold which is used in this case to obtain the best quality edge. Finally, the center of the microparts is computed by averaging the ensemble of the edge pixels; it is indicated by the circle in Fig. 2.6(d). The steps shown in Fig. 2.6(a) – (d) are executed by using MATLAB libraries.

2.3.2 Otsu Thresholding

As mentioned in the section 2.3.1, the position and velocity of a moving micropart were measured by the particle tracking velocimetry (PTV) method. In this method, the edge of the microparts is detected by the Canny filter and the center of the microparts is computed by averaging the ensemble of the edge pixels. However, the orientation and angular velocity of a micropart could not measure by the Canny method. So, the Otsu's method is applied into the particle tracking velocimetry to determine the orientation and angular velocity of a micropart.

The center of a micropart is detected in two successive images, and the velocity is calculated from the consecutive locations of the center. The steps of the PTV technique in this study are illustrated in Fig. 2.7. The same with the first step of Canny method, a series of images of a moving micropart are recorded by a microscope within the focused region of the microscope. The raw image is extracted from the recorded image series, and then, a global image threshold determined by Otsu's method (Otsu, N., 1997) is used to convert the intensity image into a binary image, as shown in Fig. 2.7(a). Finally, the center of the micro part is determined as the centroid of the image identified by the circle in Fig. 2.7(b). The orientation of the micropart is obtained by determining the principal axis of the image (William K. Pratt, 2001). The steps shown in Fig. 2.7(a) – (b) are executed using MATLAB libraries.

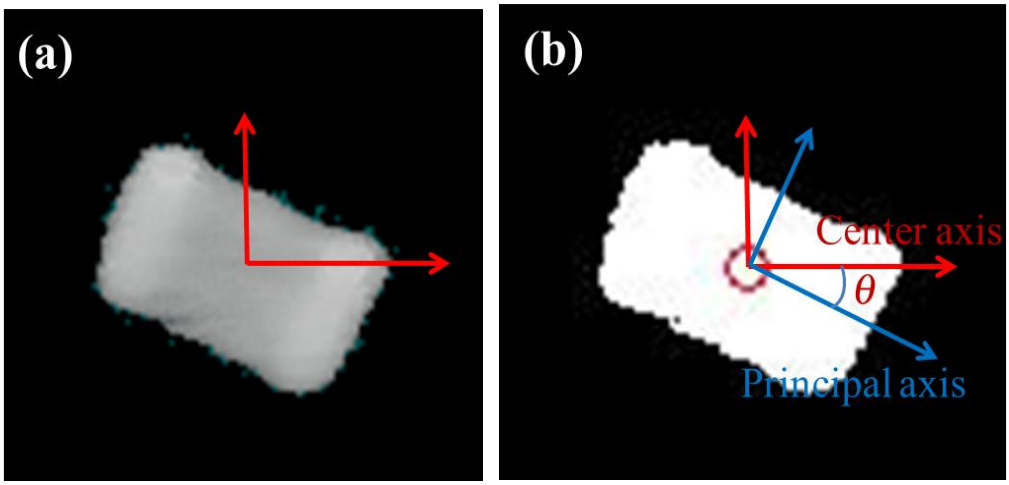

Figure 2.7 Procedure for detecting position and rotation of microparts: (a) raw image, (b) tracked center.

The moment of the image is defined as:

$$M(m,n) = \sum_{j=1}^{J}\sum_{k=1}^{K} x_j^m y_k^n F(j,k) \tag{2.1}$$

where *F(j,k)* is the intensity of the binary image, (J,K) is the size of image, and m-nth is the order moment.

The centroid of the is image is :

$$x_c = \frac{M(1,0)}{M(0,0)}$$
$$y_c = \frac{M(0,1)}{M(0,0)} \tag{2.2}$$

The central moment referred to the center of the image is

$$M_c(m,n) = \sum_{j=1}^{J}\sum_{k=1}^{K} (i - x_c)^m (j - y_c)^n F(j,k) \tag{2.3}$$

The moment of inertia covariance matrix is

$$M = \begin{bmatrix} M_c(2,0) & M_c(1,1) \\ M_c(1,1) & M_c(0,2) \end{bmatrix} \tag{2.4}$$

Let λ_1 and λ_2 be eigenvalues of matrix *M*, and $e_1 = [e_{11}, e_{21}]^T$ and $e_2 = [e_{12}, e_{22}]^T$ be the eigenvectors corresponding to λ_1 and λ_2 respectivelyOrientation angle of a micropart is then computed by

$$\theta = \begin{cases} \arctan(e_{21}, e_{11}) & (\lambda_1 > \lambda_2) \\ \arctan(e_{22}, e_{12}) & (\lambda_1 < \lambda_2) \end{cases} \tag{2.5}$$

2.3.3 Comparison between Canny and Otsu techniques in PTV method

This section presents two techniques of image segmentation, Canny edge detection and Otsu thresholding in the particle tracking velocimetry (PTV) method to investigate the motion of micropart. Depending on the quality of recorded movie of motion

micropart on the saw-tooth surface, which one of techniques was decided. For example: comparison between two techniques for the experiment of a micropart on the zirconia surface and the carbide surface as shown in Fig. 2.8. The tracking center of micropart by Otsu technique in case 1 of Fig. 2.8(b) was unsuccessful because the color zirconia surface is bright close to the color of micropart, so processing separation of light and dark regions was impossible to obtain part of desired region. In this case, Canny technique is more suitable to track edges of micropart as shown with a little noise as in seen Fig. 8(c). In case 2, using PTV method to analyze motion of micropart on the carbide surface. Because the color of carbide material totally contrast to the color of micropart, using both Canny and Otsu techniques give good detection image. In addition, as conclusion above section the orientation and angular velocity of a micropart could not measure by the Canny method. So, the Otsu's method is applied into the particle tracking velocimetry to determine the orientation and angular velocity of a micropart.

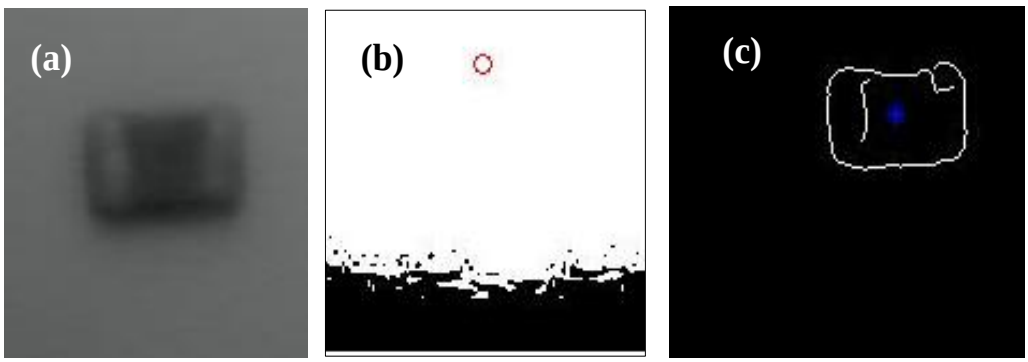

Case 1: Experiment for a micropart on the Zirconia surface

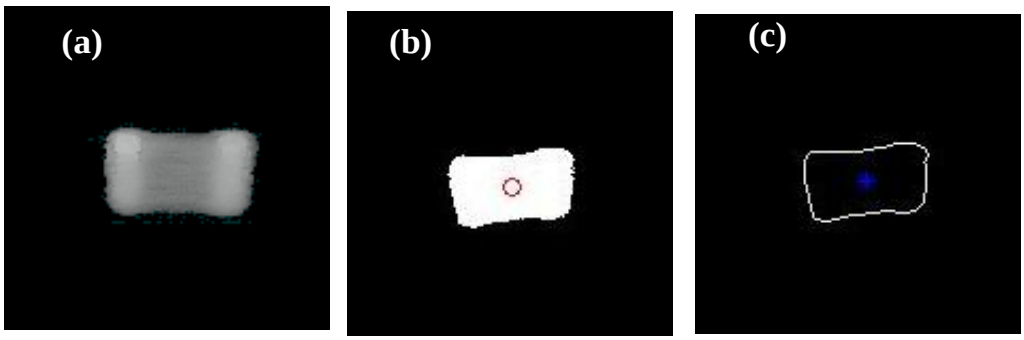

Case 2: Experiment for a micropart on the Carbide surface

Figure 2.8 a) Original image, b) Edge detection by Otsu technique, c) Edge detection by Canny technique

2.4 Characteristic of Obtained Surfaces by Technologies Fabrications

2.4.1 Fabricated surface by dicing saw

A dicing saw (Disco Corporation), a high-precision cutting and grooving machine, can be used for the saw-tooth processing silicon wafers. The saw can be equipped with a variety of diamond blades (Fig 2.10), each for a particular task. The two saw-tooth surface profiles, shown in Fig 2.9 (a) and (b), can be cut in the silicon wafer using bevel-type blades. In these figures, p, l, d, and θ are the pitch, groove length, and elevation angle of a saw-tooth, respectively. A saw-tooth profile is obtained when $p = l$; a trapezoidal profile is obtained when $p > l$.

Mitani *at el.,* (2011) previously used saw-toothed surface of silicon wafer fabricated by a dicing saw. Applying a bevel type blade, authors obtained saw-toothed periodic structure on a silicon wafer (Fig. 2.11). In this case, however, there were fabrication errors at the top teeth because of cracks, and also the shapes of each structure were not perfectly saw-toothed but close to asymmetric sinusoidal wave with low uniformity as shown in Fig. 2.12. They caused variations of contact between fed microparts and feeder surfaces, which affected the feeding stability of microparts.

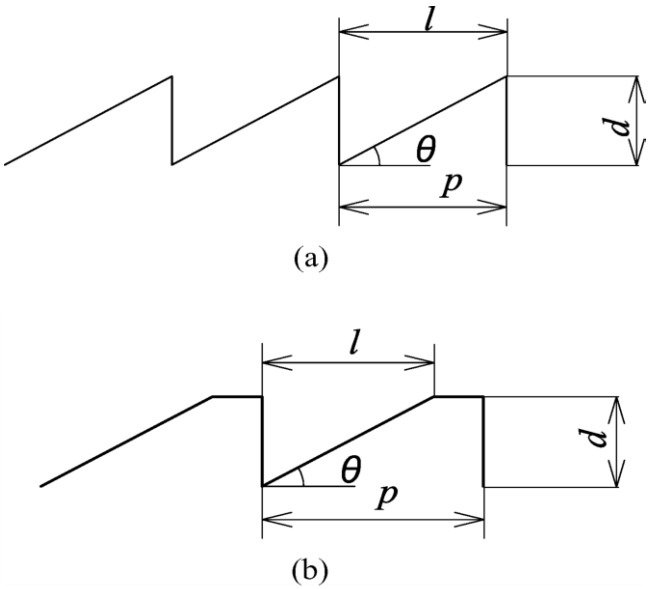

Figure 2.9 Two types of surface profiles of a silicon wafer.

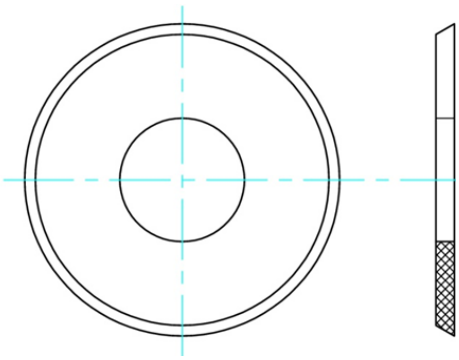

Figure 2.10 A typical diamond blade for saw-tooth process.

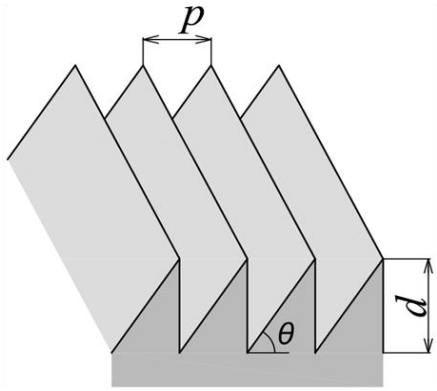

Figure 2.11 Saw-toothed silicon wafers fabricated by a dicing saw

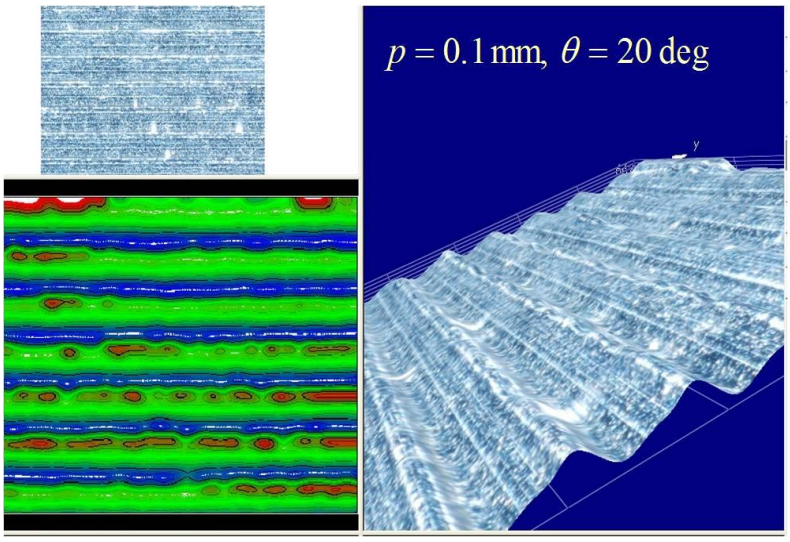

Figure 2.12 Microscopic image of a sawtoothed surface fabricated by a dicing saw with a bevel type blade: 3D image synthesized from focusing images by height, and colored contour model

2.4.2 Fabricated surface by grinding process

The grinding technology is applied to develop various reflection surfaces for optical communication. This technology can generate periodic V-shape grooved surfaces. Fig. 2.13 shows a grooving blade, which has a beveled in one side and straight in the other. Using this blade, asymmetric fabricated surface can be generated on various materials according to its thickness, 2 mm.

Brass, zirconia, and cemented carbide materials were chosen based on their machinability, with brittleness, low viscosity, and low thermal deformation. These characteristics are suitable to be fabricated into accurate saw-toothed. Figure 2.14 shows the obtained saw-tooth profile on cemented carbide material for example by using the grinding technology, and on other materials will be discussed on the next Chapter.

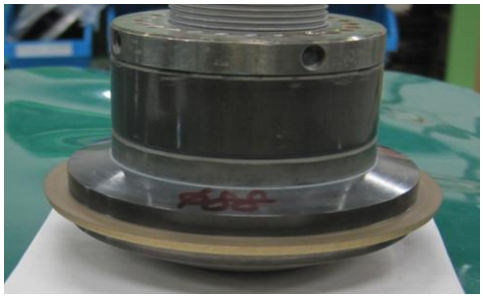

Figure 2.13 A grooving blade

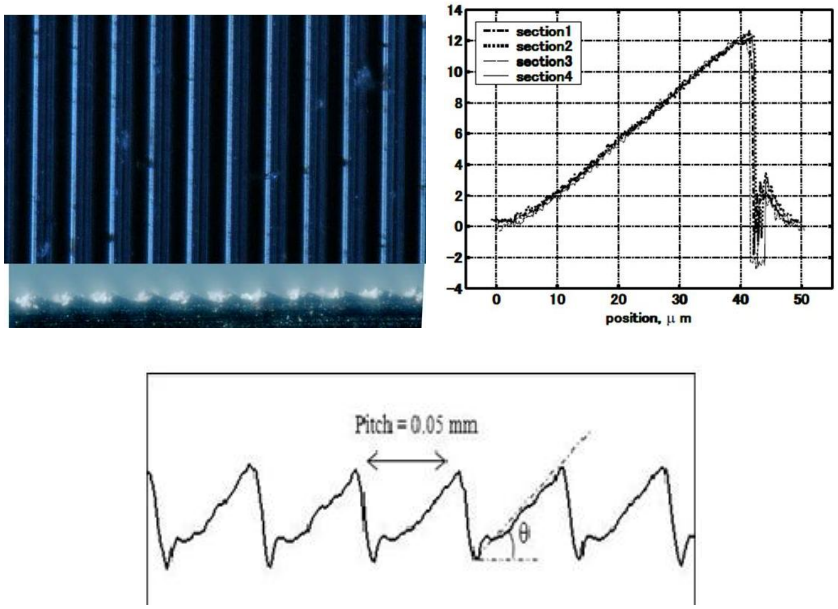

Figure 2.14 Profile of fabricated surface by grinding process on cemented carbide material

2.4.3 Fabricated surface by femtosecond laser process

Femtosecond laser technology, which is used to reshape materials, to control chemical reactions, and to fabricate microparts, is also used in microelectromechanical system (MEMS), and to observe super-high-speed phenomena. Materials around the area irradiated in femtosecond laser fabrication are chemically and thermally unaffected. The minute grating structures thus formed on materials such as silicon and stainless steel are of the same order of magnitude as the laser beam pulse wavelength and the periodic structures on the contacting surface reduce friction and adhesion effects by decreasing the contact area. In our study, we applied experimental surfaces which were designed to feed 0402 capaciors $0.4 \times 0.2 \times 0.2$ mm in size and 0.1 mg weighting using double-pulsed femtosecond laser irradiation to create an asymmetrical surface (A Mitani and S Hirai, 2009). The feeder surface is stainless steel shim tape 0.5 mm thick, 10 mm wide, and 33 mm long. To make the feeder profile asymmetric, the authors used double-pulsed femtosecond laser beam irradiation in which a single-axis femtosecond laser beam is divided into two, with one side having an angle of 20^{o} and delay of 50 ps. The surface begins moving 50 ps after irradiation by the fist beam, and simultaneous irradiation with the second beam forces the transpirations recoil to shift toward the second beam's incidence angle generation an asymmetrical surface (Fig. 2.15) with many periodic convexities (Fig. 2.16).

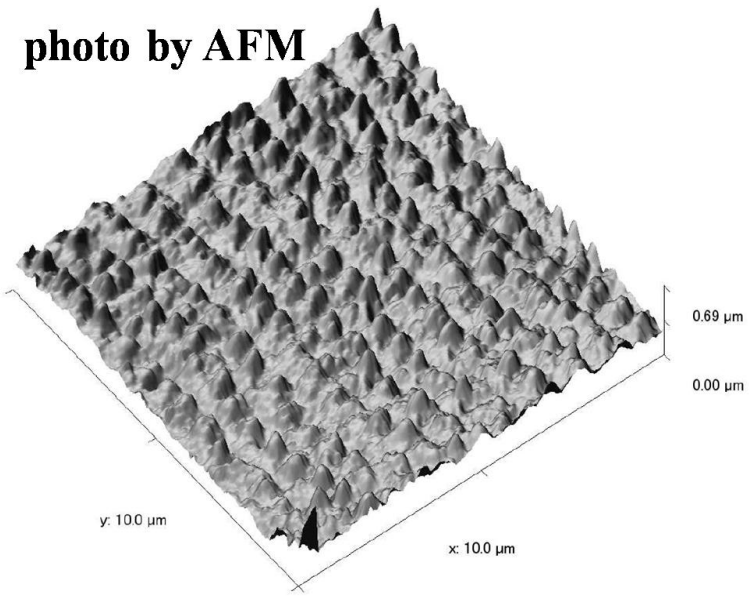

Figure 2.15 Microfabricated surface profile seen in atomic force microscope

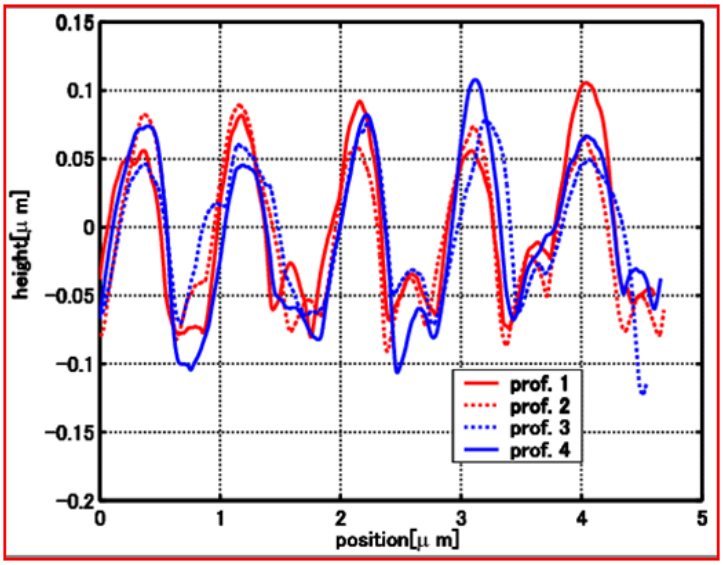

Figure 2.16 Microfabricated surface periodicity

2.4.4 Fabricated surface by etching process

Etching process, a MEMS (micro electro mechanical system) technology, can generate stable and precise periodic pattern on a single crystal silicon wafer according to an etching mask. The behavior of the etching process, such as etching speed and etching direction, depends upon silicon crystal orientation appeared on the cut side. This means that we can control the surface profile generated on the etched surface by selecting an appropriate orientation of silicon crystal. In the case of a typical crystal orientation surface, for example [100], the etching speed vary according to the etching direction along the crystal surface, then etching process advances isotropically.

We prepared silicon wafers with a plain orientation of [221] in order to generate an asymmetric periodic structure by the etching process. A silicon wafer was thermally oxidized under a temperature of 1000 °C and an oxygen density of 0.2 kg/cm2 with a fluid rate of 5 l/min, then the thermally oxidized film with 300 nm in thickness was generated. After photoresist processing using a spin coater, a periodic slit pattern was exposed on the resist film. The Si02 film was etched by the reactive ion etching (RIE) process of the CHF3 gas with 10 sccm and a radio frequency (RF) power supply energy of 100 W. Removing the resist film, the silicon wafer was etched anisotropically using the ELM-SiM (org), an enchant for high speed anisotropic etching of silicon (Mitsubishi Gas Chemical Company), with a temperature of 80 °C for about 90 min. Then the

silicon wafer was fabricated asymmetry. Figure 2.17 shows a microscopic image of an anisotropic etched surface developed in the previous works, captured from the side (Mitani. A and Matsuo.Y, 2011). From this figure, the profile of each tooth was asymmetric triangular shape, and all of them were uniform. We also found that the etching process was stopped at the [111] surface. The elevation angles of both right and left sides were 15.6 ° and 57.4°, respectively, which were close to the theoretical values defined by rotation of silicon crystal, 15.8 ° and 54.7 °, respectively.

However, we found two problems in its sawtooth shape as shown in Figure 2. 18. There was resist film remaining at the top of tooth that influences on the tribology asymmetry because the both side slopes are hidden by them. Also, unexpected over etching was occurred between the right side slope and the resist film. This made it difficult to contact microparts with the right side slope. In order to improve the sawtooth shape, we tried to realign the etching parameters and obtained three different surfaces.

All anisotropic etched surfaces were captured by a scanning electron microscope system (SEM) to obtain geometric parameters of surface profile. The geometric parameters of tooth shape was measured based on tooth model described in Figure 2.19.

Figure 2.20 shows the 3D contour models and their surface profiles. Overshoots around the edge at the left side of the flat part and around the bottom of groove can be ignored because they may be caused by scanning error.

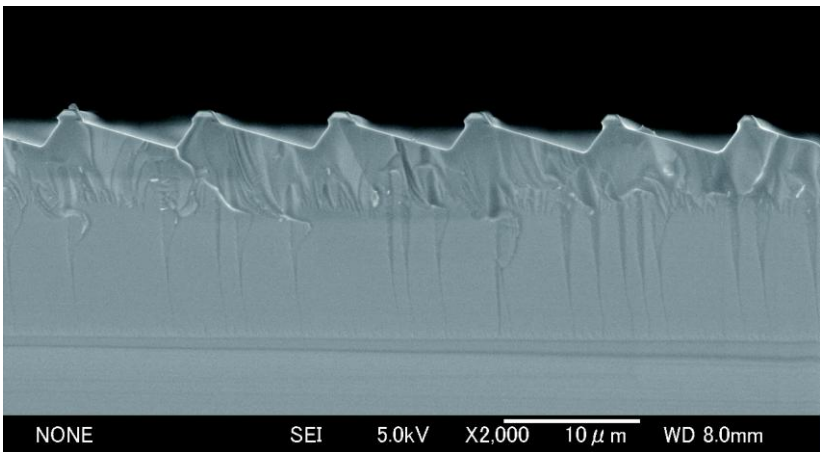

Figure 2.17 Microscopic image of a sawtoothed surface fabricated by the anisotropic ething process of [221] oriantation silicon wafer

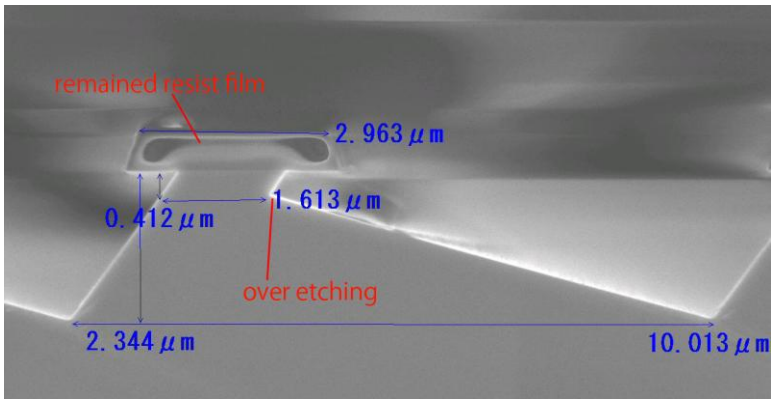

Figure 2.18 Remained resist film on thee anisotropic etched process

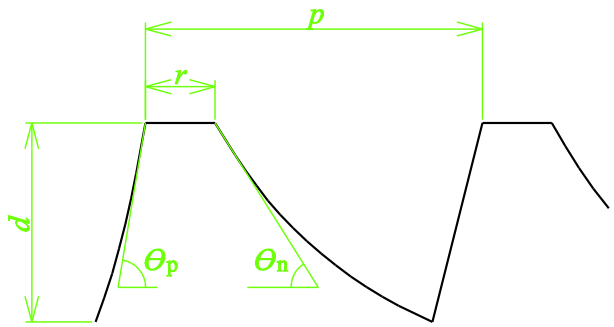

Figure 2.19 Geometric model of anisotropic etched surface

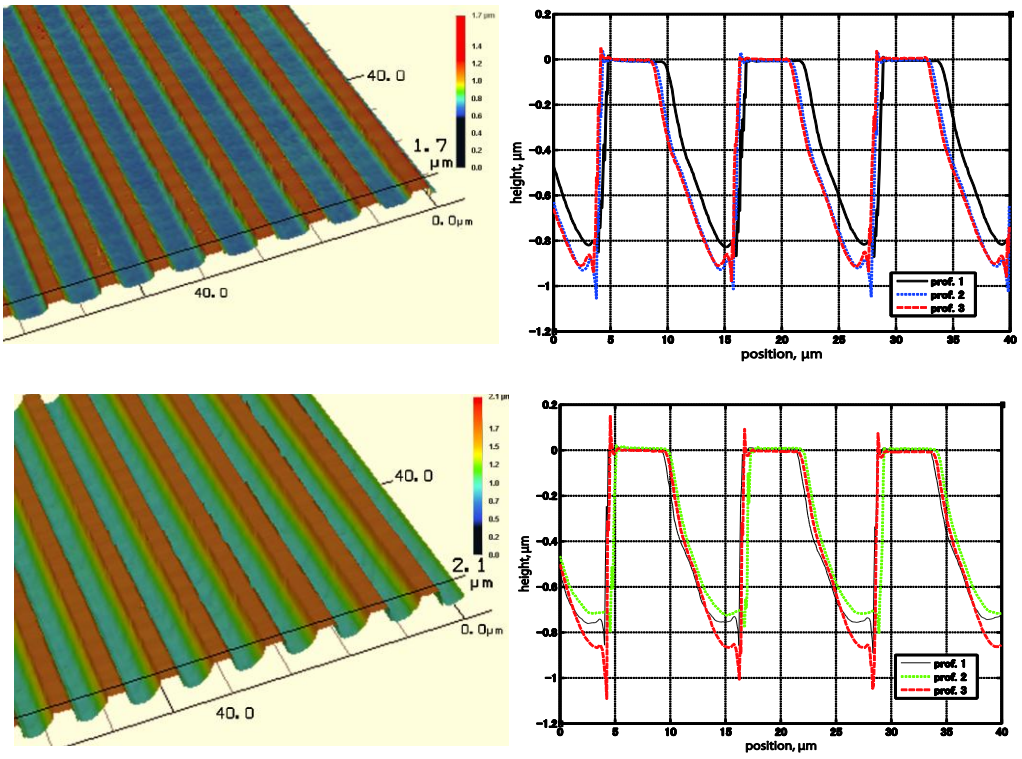

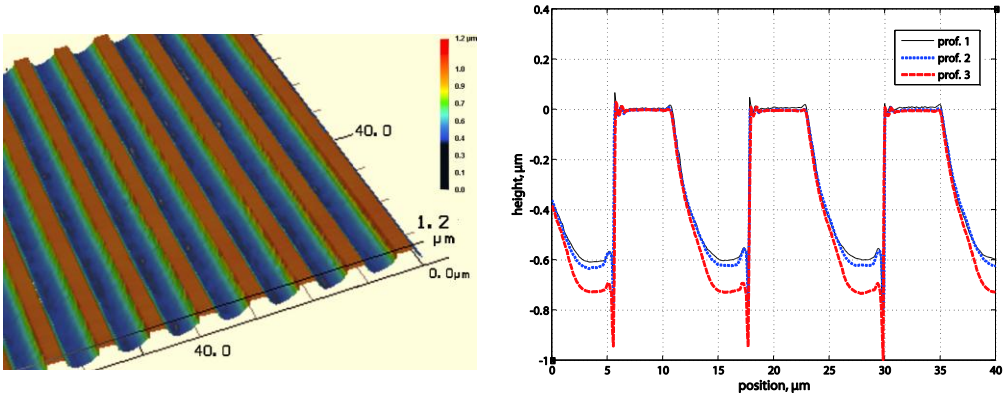

Figure 2.20 3D analysis model of asymmetric etched surface and their sections of three arbitrary points

2.5 Closing remarks

This chapter has introduced experiment systems, microparts movement tracking method, and the discussion of fabrication techniques dependent surface.

To track the motion of microparts, Particle Tracking Velocity (PTV) was employed. Two techniques of image segmentation, Canny edge detection and Otsu thresholding, were used to determine the position and velocity of a micropart. Canny edge detection was more suitable than Otsu thresholding for grey scale with low noise. In contrast, Otsu thresholding was a good choice to determine the orientation and angular velocity of microparts. In our study, both techniques were used depending on the quality of the images and requirement of the output information.

In this chapter, the dependence of the characteristic of the feeder surface on fabrication technology was also discussed. The discussed fabrication technologies consisted of dicing, grinding, femtosecond laser, and etching processes. By dicing process, saw-tooth patterned profiles on silicon wafer were achieved. However, this process produced the errors at the tooth tops because of cracks. Furthermore, the shapes of the profiles were not perfectly in saw-tooth shapes. The profiles were sometime closed to square wave with low uniformity. Alternatively, grinding technology improved the saw-tooth profiles and this pattern profiles could be achieved on different materials not only on silicon. However, grinding technology could not produce the saw-tooth profiles with submillimeter peak for the experiments on submillimeter microparts.

Fortunately, femtosecond laser and etching process could overcome this drawback, since they avoided using an external mechanical contact to the surface. These two techniques allowed us to fabricate a wide range of saw-tooth peaks on a wide range of materials, and then the experiments on various parameters will be enabled.

Chapter 3

Principle of Unidirectional Feeding

This chapter presents the principle of feeding system that uses the asymmetrically patterned surface driven by symmetric vibration to transport microparts in one direction. First, the details of micropart such as capacitors used in electrical devices are described. Several dimensions of the microparts are considered and investigated by a microscopy system. Next, the idea using a saw-tooth patterned surface is described to transport microparts unidirectionally with symmetric vibration. The difference between the forces when the microparts contacts to either the edge or the slop of the saw-tooth partterned surface pushes the microparts moving in one direction. Finally, we analyze the contact force as a function of the relative position of a micropart to the saw-tooth.

3.1 Introduction

A variety of microparts, such as ceramic chip capacitors and resistors, are currently being produced in large numbers for cellular phones and palm-top PCs. Microparts feeders are applied in factory to make inspecting, feeding, and shipping automatically. To feed along various parts in one direction, different force should be applied according to direction by asymmetric vibration, inclined structure, or sloping mechanism. Contrary, this work proposed to realize unidirectional feeding using an asymmetric surface such as saw-tooth surface. In this case, contact changes according asymmetric frictional property by the asymmetric fabricated surface. Also when feeding along microparts that less than 100 μm in size such as ceramic chip capacitors and resistors, the effect of adhesion between feeder surface and micropart surface is getting larger than inertia since the former is proportional to the area of contact, while the latter is proportional to the volume. In order to analyze the dynamics of microparts moving on such a asymmetric surface as saw-toothed surface, it is essential to consider the effect of both adhesion and inertia. In this chapter, contacts between three types of ceramic chip capacitors and a saw-tooth surface were analyzed based on measurements using a microscopy system.

3.2 Microparts surface inspection equipment

The surface profiles of capacitors and saw-toothed silicon wafers were analyzed using a multi-purpose zoom microscope MULTIZOOM AZ100 (Nikon Instruments Co. Ltd.) With a mono zoom optical system that enables on-axis observation and documentation and built-in optics of from 1 × to 8 × magnification. In combination with an objective lens of up to 5X magnification, we could take pictures at up to 40 × magnification. The microscope also has an automatic focus height positioning device using a stepping motor, then focus height can control at a resolution of 0.54 μm. A digital camera is attached to the top of the microscope, and pictures are forwarded to a computer via USB interface. The resolution of forwarded pictures taken at 40 × magnification is 0.276μm/pixel. Each image is forwarded to a personal computer and saved as a bitmap file. We used focus image synthesizing software DynamicEye REAL (Mitani Corp.) to analyze these convexities. The software can synthesize a three

dimentional (3D) model from these pictures according to focus height. Sections of the 3D model are yielded to obtain a convexity size and position. By using the DynamicEye Real software, we obtained a 3D model synthesized according to focus height. We could also derive discrete section along any directions of the 3D model. Sections of the 3D model were assessed to obtain a convexity size and position.

3.3 Microparts surface characteristics

Figure 3.1 shows the raw image of ceramic chip capacitors, as examples, which are captured by the microscope. Each capacitor is composed of a conductor with an electrode on either side. The electrodes contact the feeder surface, as they are about 10μm higher than the conductor. There are also many convexities on the surface of the electrode. We obtain a contour line of the synthesized model as shown in Fig. 3.2. In this figure, the convexities on the electrode of the capacitors are defined and analyzed (Mitani *et al.*, 2007). Figure 3.3 shows representative contours along a capacitor, obtained using sensing-pin surface measurement Form Talysurf S5 (Taylor Hobson Corp.).

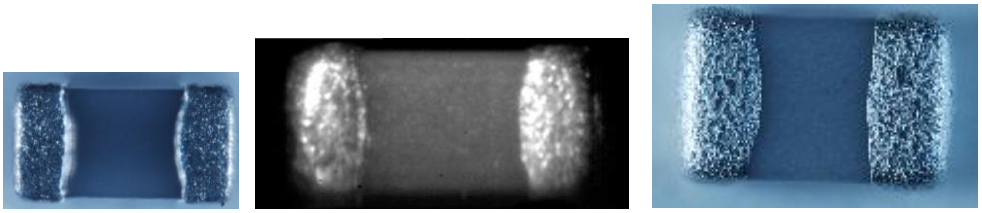

(a) (b) (c)

Figure 3.1 Microscopy raw image of ceramic chip capacitors: (a) 0402-, (b) 0603-, and (c) 2012- capacitors

Principle of Unidirectional Feeding

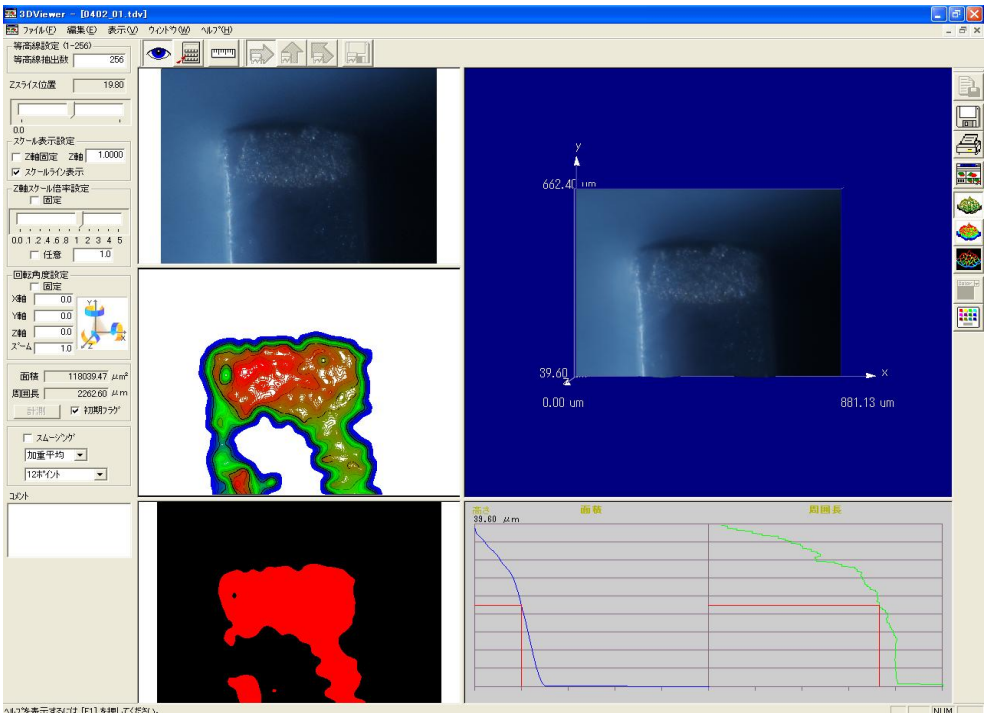

(a)

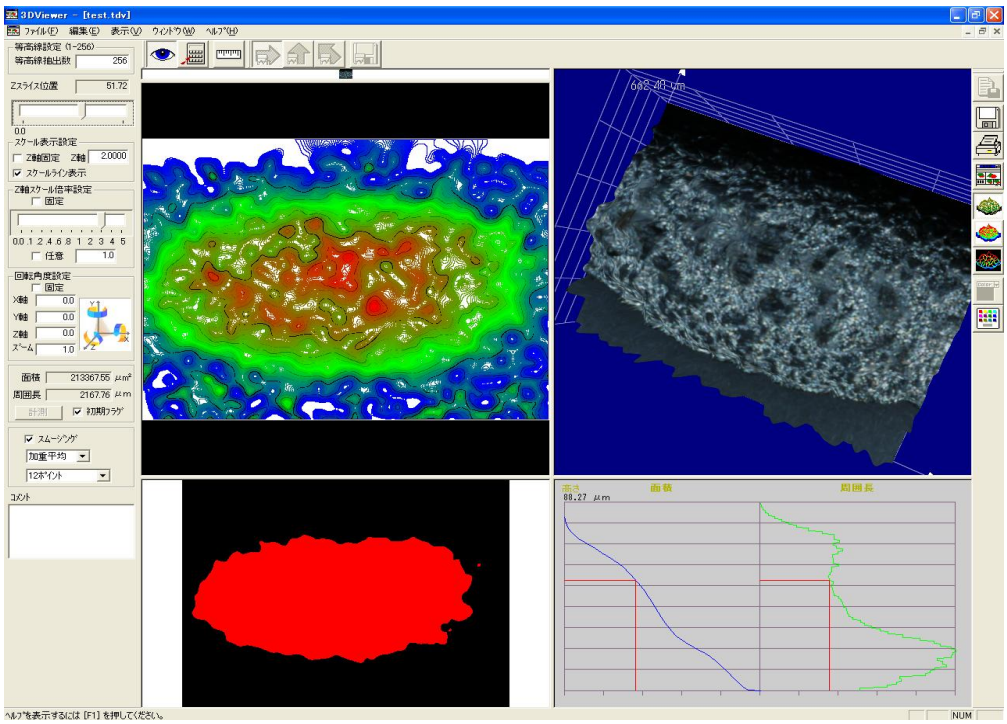

(b)

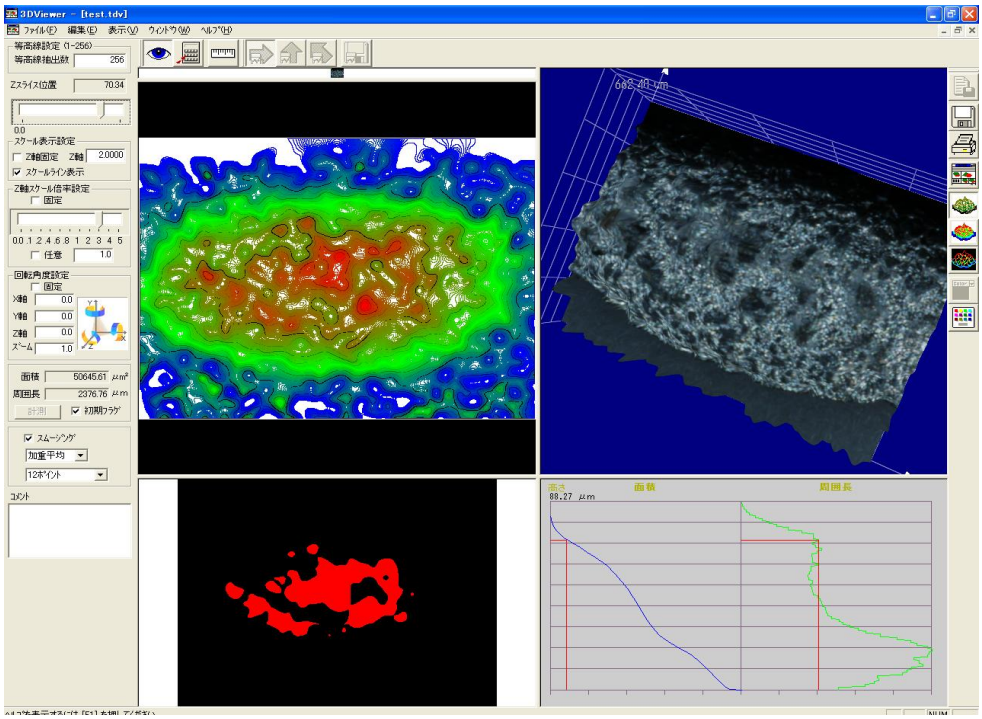

(c)

Figure 3.2 Measurement results 3D contour line of electrode of ceramic chip capacitors: (a) 0402-, (b) 0603-, and 2012- capacitors

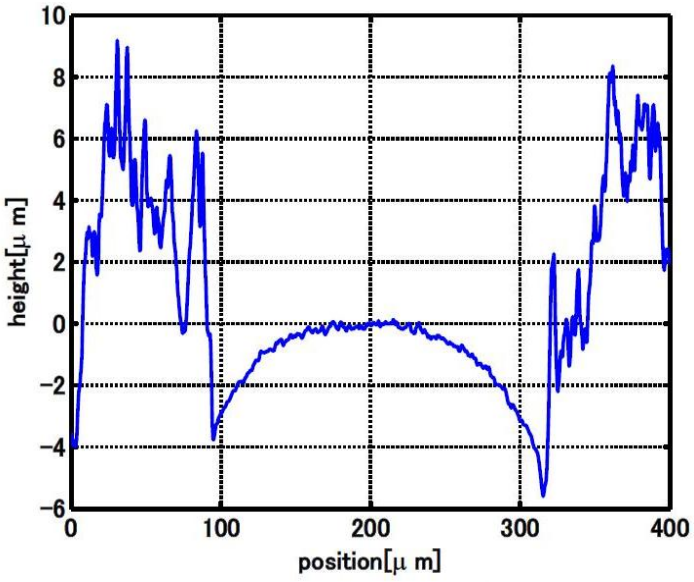

(a)

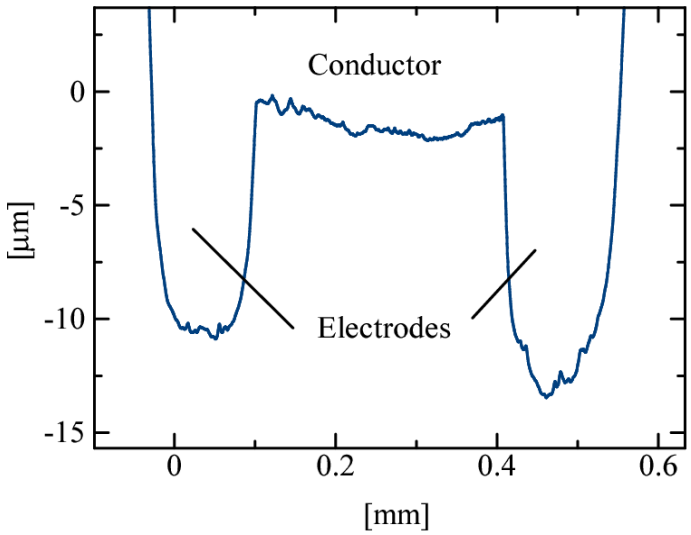

(b)

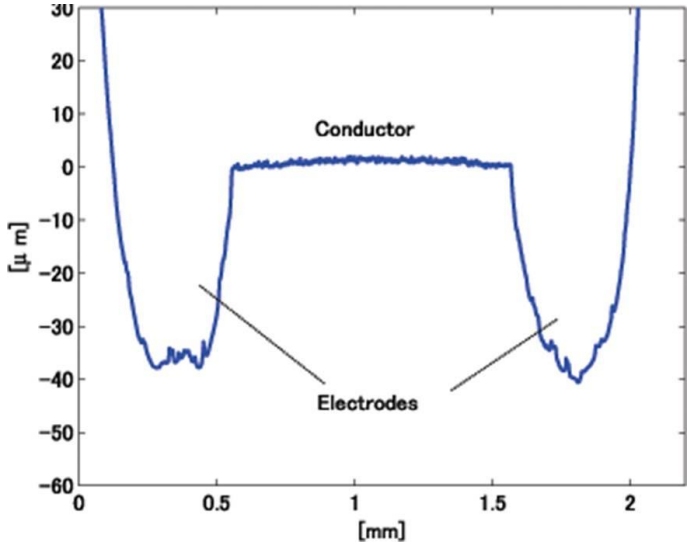

(c)

Figure 3.3 Measured section of capacitors: (a) 0402-, 0603-, and 2012- capacitors

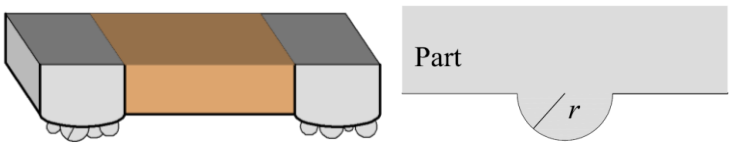

(a) Electro model (b) Convexity

Figure 3.4 Micropart surface model

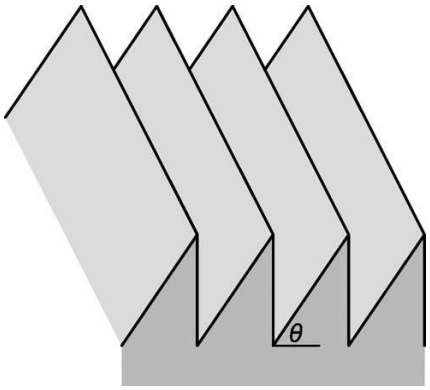

Figure 3.5 Saw-tooth surface model

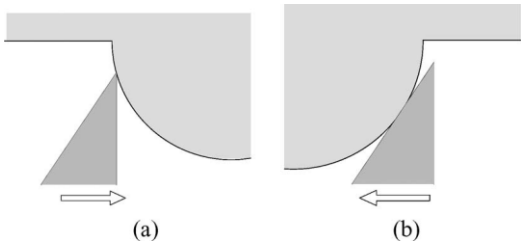

Figure 3.6 Two contacts between a micropart and a saw-tooth

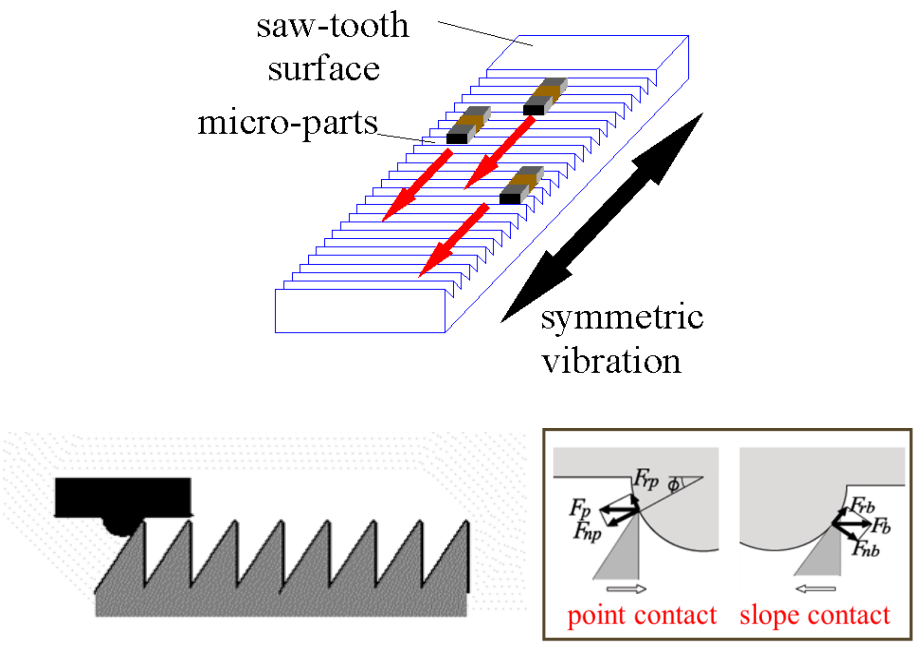

Figure 3.7 Diagram of a micropart feeder with a sawtoothed surface and symmetric vibrations

We assume that the convexities in the electrode surface are perfectly spherical, as shown in Fig. 3.4(a) and the feeder surface is saw-toothed (Fig. 3.5). Let r be the radius of the convexity, as shown in Fig. 3.4(b). Recall that θ is the elevation angle of a saw-

tooth, as illustrated in Fig. 3.5. A saw-tooth can contact an electrode in one of the two ways, as shown in Fig. 3.6: a point contact in which the point of a saw-tooth contacts with a convexity, or a slope contact in which the slope side of a saw-tooth contacts with a convexity. Consequently, they drive the microparts in one direction.

In our study, we have researched dynamics motion of microparts on the microparts feeder applied an asymmetric fabricated surface, for example, saw-tooth surface, as a feeder table (Figure 3.7). The asymmetric fabricated surface can feed along microparts in one direction using horizontal and symmetric vibration because contact between a micropart and the asymmetric fabricated surface varies according to the direction of motion. In order to formulate the dynamics of micropart precisely, we need to analyze both inertia caused by vibration of the feeder surface and adhesion according to these contacts.

3.4 Contact between microparts and saw-tooth surface

The driving force which drive the microparts in one direction according to the contact conditions are slope contact and point contact.

3.4.1 Slope contact

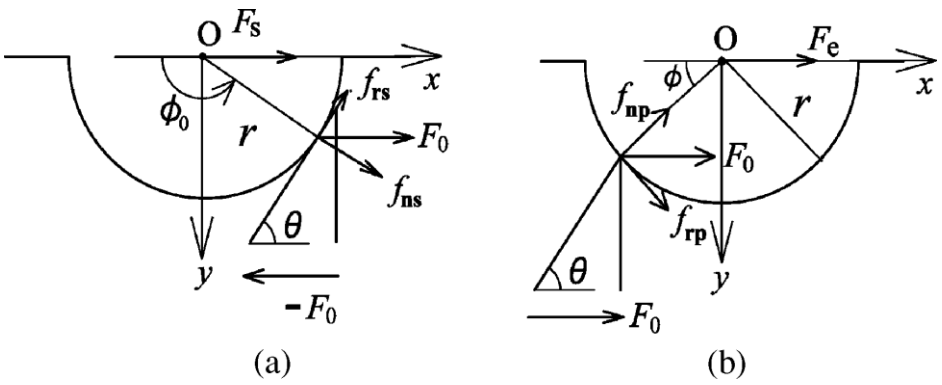

Figure 3.8 Statics of each contact condition

Let us assume that a slope pushes a convexity to the left with a contact force F_0, as shown in Fig. 3.8(a). The convexity is climbing the slope of the saw-tooth. Let μ_s be the friction coefficient of the slope contact, f_{rs} be the normal force along the slope of the saw-tooth, and f_{ns} be the tangent force to the slope of the saw-tooth. Then, the following equations can be derived:

$$f_{rs} = F_0 cos\theta - \mu_s F_0 sin\theta \quad \textbf{(3.1)}$$

$$f_{ns} = F_0 sin\theta. \quad \textbf{(3.2)}$$

Driving force F_s along the x-axis can be expressed as

$$F_s = f_{ns} cos\theta + f_{rs} sin\theta = F_0(1 - \mu_s cos\theta sin\theta). \quad \textbf{(3.3)}$$

Note that F_s = - F_0 when $cos\theta - \mu_s sin\theta < 0$.

3.4.2 Point contact

Let us assume that a point on a saw-tooth contacts a convexity with a contact force F_0, as shown in Fig. 3.8(b). Let ϕ be the point contact angle and μ_s be the friction coefficient of the point contact. The driving force is the resultant of the normal force $f_{np} = F_0 cos\theta$ and the friction force $f_{rp} = \mu_s f_{np}$. Driving force F_e along the x-axis can be expressed as follows:

$$F_e = f_{np} cos\emptyset + f_{rp} sin\emptyset = F_0 cos\emptyset(cos\emptyset - \mu_e sin\theta). \quad \textbf{(3.4)}$$

Note that F_e = 0 when $sin\emptyset - \mu_e cos\emptyset < 0$.

3.5 Previous feeding experimental results

From based research (Mitani *et al.*, 2007), feeding experiments on the 2012-type capacitors were conducted using a θ = 300 surface. The voltage on the piezoelectric actuators was a 120-V peak – to – peak square wave. Figs. 3.10, 3.11, and 3.12 show the experimental results for driving frequencies of 10, 15, and 30 Hz, respectively. Fig. 3.10 (a) and (b) shows the trajectories of the microparts over a 1-s period at a driving frequency of 10 Hz. The microparts rotated or jumped in both feeding directions, which shows that feeding is unstable. Fig. 3.11 (a) and (b) shows the trajectories of the microparts over a 4-s period at a driving frequency of 15 Hz. In both the cases, all the microparts moved steadily. The microparts in (b) moved in the direction opposite to those in (a), which proves that the directionality of the feeding is achievable using a saw-tooth surface. Fig. 3.12 (a) and (b) shows the trajectories of the microparts over an 8-s period at a driving frequency of 30 Hz. The feeding distance was short, but the microparts clearly moved in one direction, namely in the direction of the saw-tooth surface. Fig. 3.13(a) and (b) shows the results of the feeding experiments using a θ =

60◦ surface. A driving frequency of 15 Hz was applied for 2 s. In the positive direction, the second micropart reached the front of the feeder table in about 2 s. The others did not reach the front of the feeder table while they moved in one direction. In the negative direction, the first micropart moved in the direction opposite to the desired direction. The others stopped in the middle of the feeder surface. Thus, unidirectional feeding was not achieved on the θ = 60◦ surface. No directionality was observed with the θ = 60◦ surface, presumably because the microparts remained still during the slope contact. Some microparts moved faster on the θ = 30◦ surface. The adhesion force on the θ = 60◦ surface was weaker than that on the θ = 30◦ surface.

From the experiments described above, the most stable feeding was achieved when a 15 Hz square wave was used. But it took 4 s or longer the microparts to move 30 mm. For a faster feeding, the driving conditions and surface profile need to be improved. The microparts jumped and revolved when the driving frequency was 10 Hz. Large feeder vibration amplitudes generated high driving forces on the microparts. The edges of the microparts were raised by the collision between the microparts and the saw-teeth. The microparts moved only short distances when the driving frequency was 30 Hz. Amplitudes of the feeder vibration were too low to change the state of contact between the microparts and the saw-teeth from slipping on stopping at point contact.

Figure 3.9 Experiment table set up for 2012-capacitors (Mitani *et al.*, 2007)

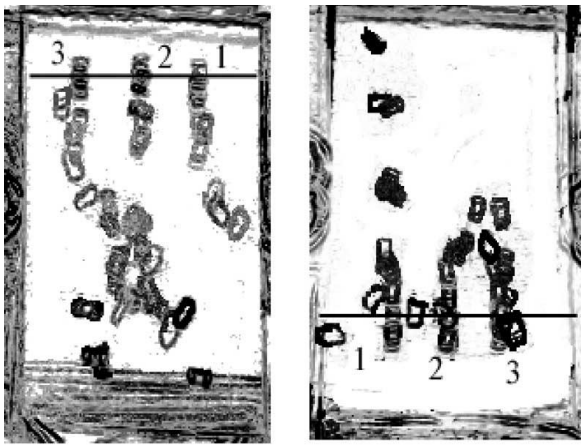

(a) (b)

Figure 3.10 Motion of the 2012-type capacitors due to a 10 Hz on a $\theta = 30^0$ surface (Mitani *et al.*, 2007)

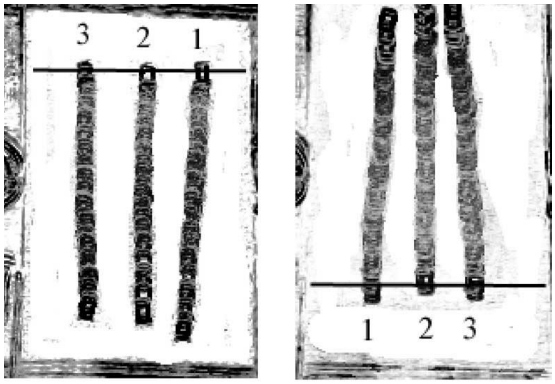

(a) (b)

Figure 3.11 Motion of the 2012-type capacitors due to a 15 Hz on a $\theta = 30^0$ surface (Mitani *et al.*, 2007)

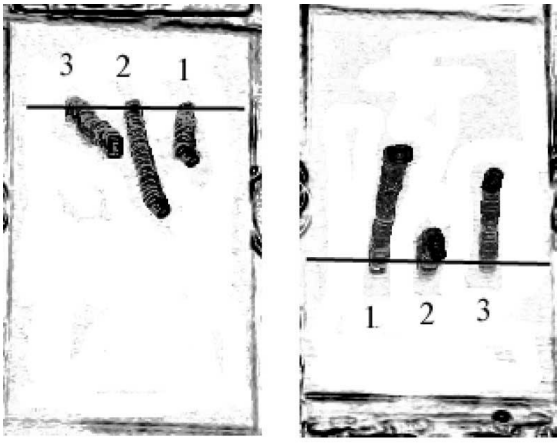

(a) (b)

Figure 3.12 Motion of the 2012-type capacitors due to a 30 Hz on a $\theta = 30^0$ surface (Mitani *et al.*, 2007)

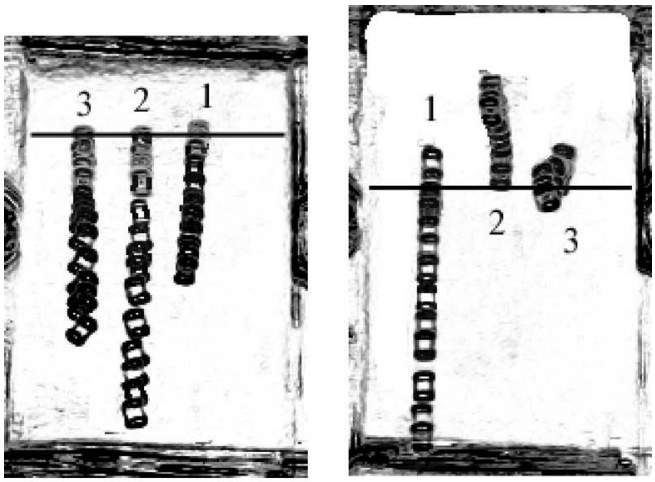

Figure 3.13 Motion of the 2012-type capacitors due to a 15 Hz on a $\theta = 60^0$surface (Mitani *et al.*, 2007)

3.6 Closing remarks

We have proposed the simple microparts feeder which used an asymmetrically patterned surface that was saw-toothed surface integrated with symmetrical vibration to control movement of microparts in one direction. In addition, we have analyzed the convexity size and position of the electrode surface. As a result, the convexity could be approximated by a hemisphere. In principle, the saw-tooth surface contacted to the microparts with either the point or the slope contacts. The different force between these contacts results in unidirectional motion of the microparts. The experiments have shown that the unidirectional feeding was achieved.

In future work, we will focus on a method to derive motion of microparts to a desired target position and orientation by applying various textured surface.

Chapter 4

Effect of Asymmetric Patterned Profile on Feeding Velocity

This chapter investigates the effect of the patterned profile on the surface to the feeding velocity of the micropart by experiment. The real patterned profiles were analyzed by using a laser microscope. To evaluate the effect of profile surface on the feeding micropart, we conducted experiments on a type of capacitor. The instantaneous motion of a micropart on a saw-tooth surface was analyzed by PTV method described in Chapter 3. The experiments were carried out for different patterned profiles which obtained by different materials, sizes of micropart, and driven frequencies on the surface. The feeding velocity of the micropart was analyzed by its power spectrum which was obtained by Fourier transform technique. The experimental result showed that microparts move stably and quickly on the profile surface which is close to the ideal saw-tooth shape. Additionally, the stability in motion of the microparts in range of frequency was also demonstrated in this chapter.

To access the effects of surface profiles on the motion of microparts, we utilized three materials as feeder surfaces: brass, zirconia, and cemented carbide. Each material was cut into 30 mm planar pieces, and the surfaces were micro-fabricated into a saw-toothed periodic structure with an elevation angle $\theta = 20^0$ and a pitch p = 50μm, as shown in Fig. 4.1. They were micro-fabricated by a grinding machine.

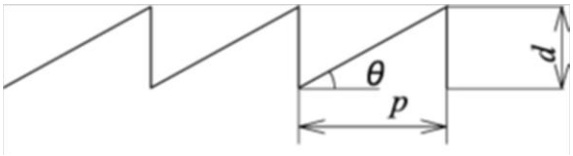

Figure 4.1 Ideal saw-tooth profile of surface

4.1 Analysis of real surface profiles using scanning laser microscope system

Inspection each surface using a scanning laser microscopy system HD100D (Lasertec Corp.) in Chapter 2, we obtained microphotograph of the saw-toothed fabricated surfaces as well as their surface profile model of each surface.

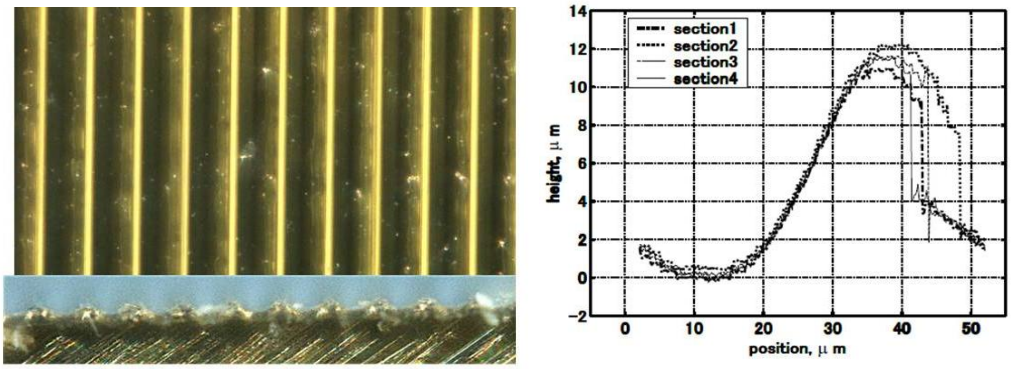

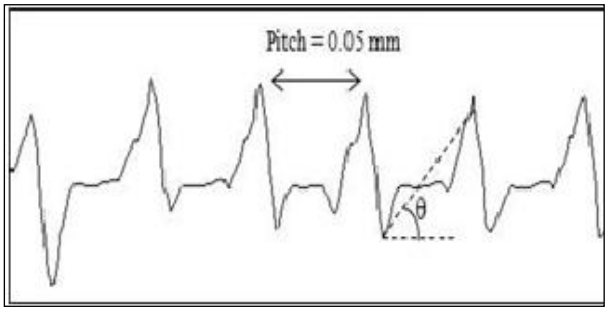

(a) Brass material

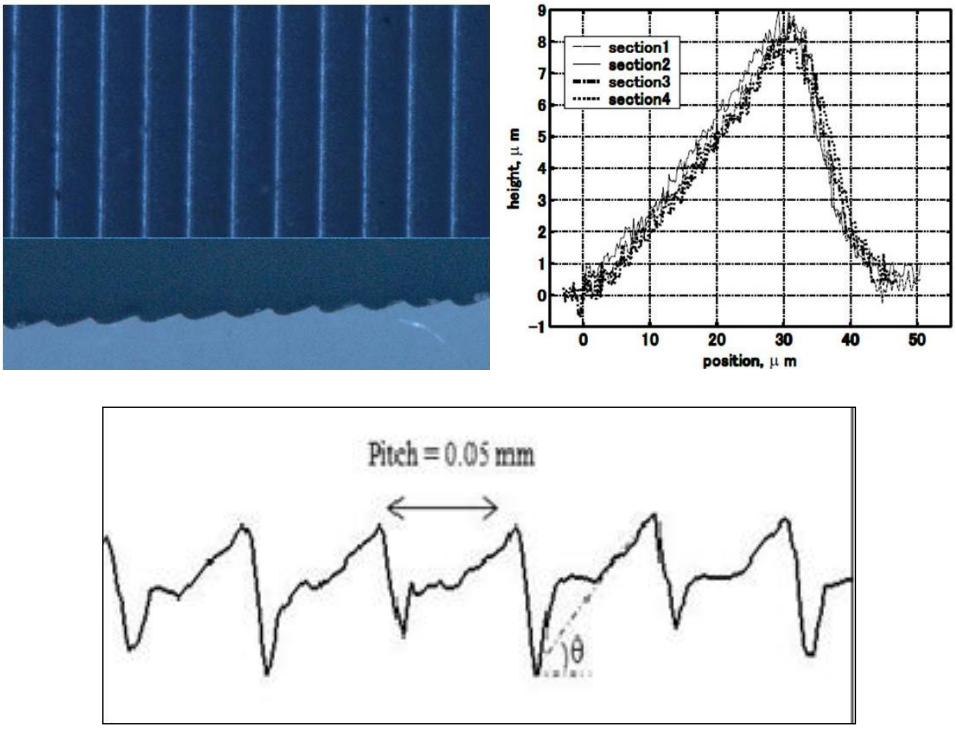

(b) Zirconia material

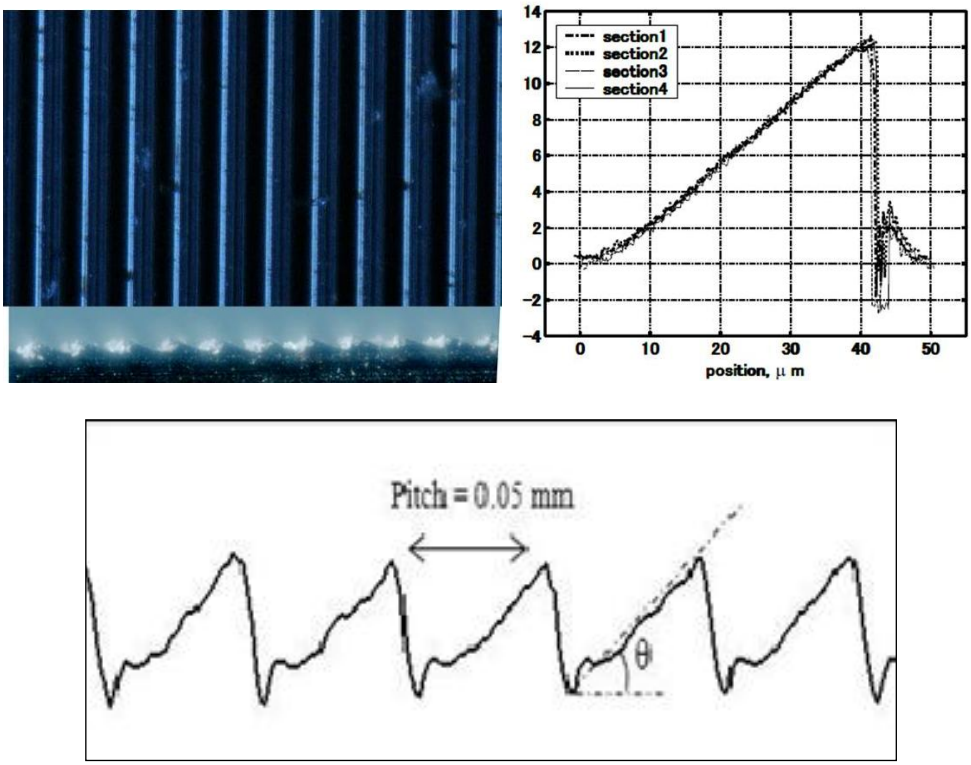

(c) Cemented carbide material

Figure 4.2 Microphotograph and profile of saw-toothed fabricated surfaces

As shown in Fig. 4.2 (a) - (c), these micro-fabricated showed that they were not perfectly saw-toothed, but had many dents and cracks on the top of the teeth caused by fabrication errors and the characteristics of each material. Any three sections on each surface are described in Fig. 4.2(a) – (c). Seen in Fig. 4.2(a), there were vertical surface partially in the right side of the saw-tooth on the brass surface, even though there were cracks around the top of saw-tooth and bottom of the left side, and also there were some roughness in the shape of saw-teeth. In contrast, both zirconia and cemented carbide surfaces were stable, because of few cracks appeared in their surfaces and highly uniformity in the shape of these saw-teeth (Fig. 4.2 (b) – (c)). Specially, the cemented carbide surface was an ideal because the top of saw-tooth was pointed and the right side was closed to vertical.

4.2 Effect of asymmetric profile on the motion of micropart

4.2.1 Particle Tracking Velocimetry

As mentioned in Chapter 3, the particle tracking velocimetry (PTV) is a technique to determine the velocity of an object. Figure 4.3 plots the tracking center results of micropart on the brass-, carbide-, and zicornia-material surface, respectively, as examples by Canny edge detection method.

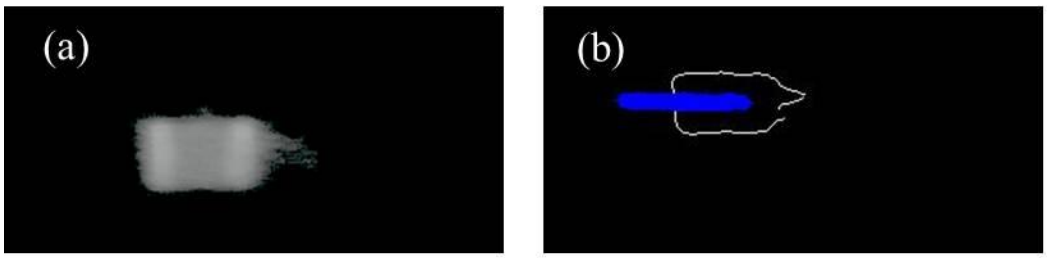

Experiment No. 1

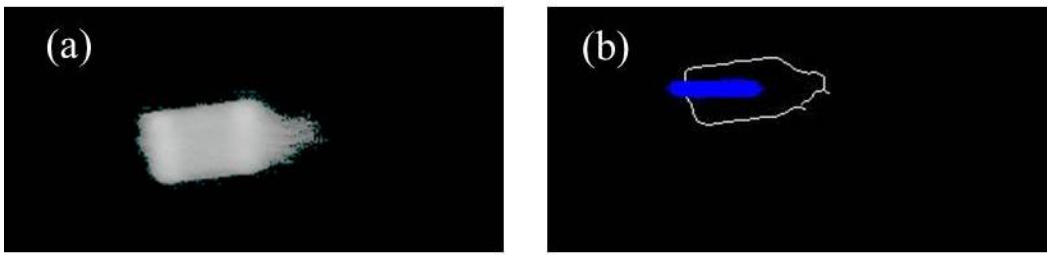

Experiment No. 2

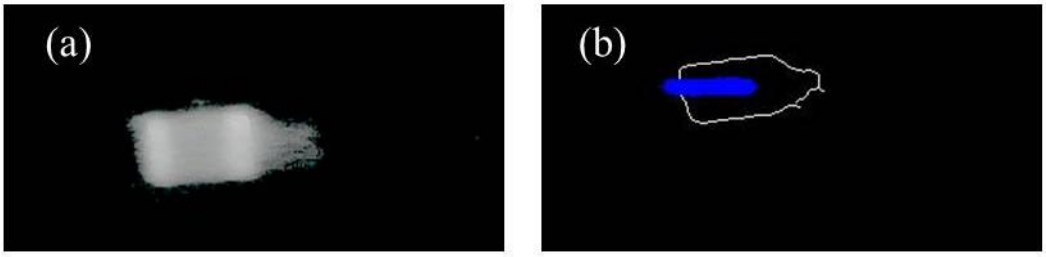

Experiment No. 3

on Brass material

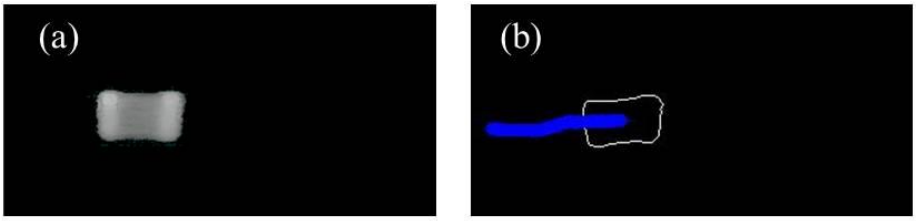

Experiment No. 1

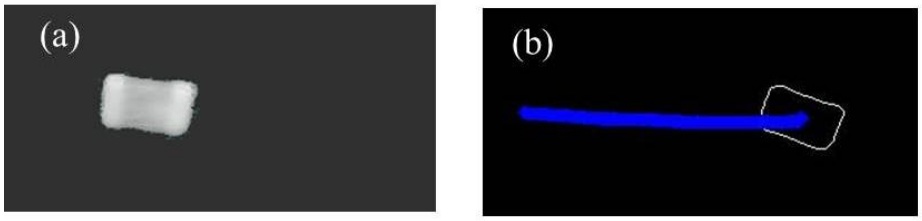

Experiment No. 2

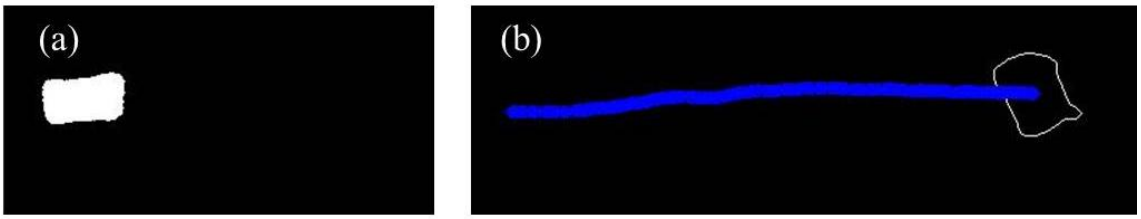

Experiment No. 3

on Carbide material

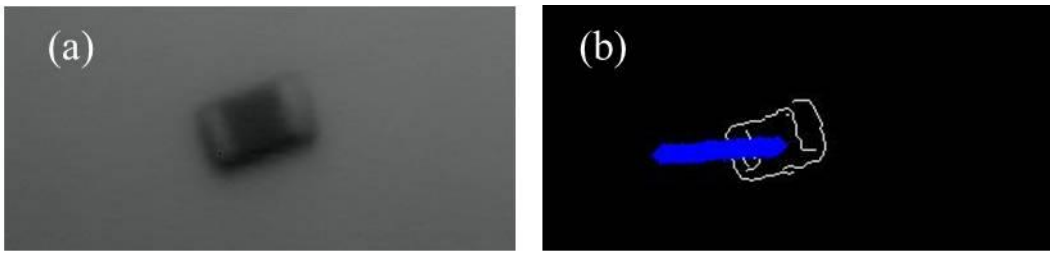

Experiment No. 1

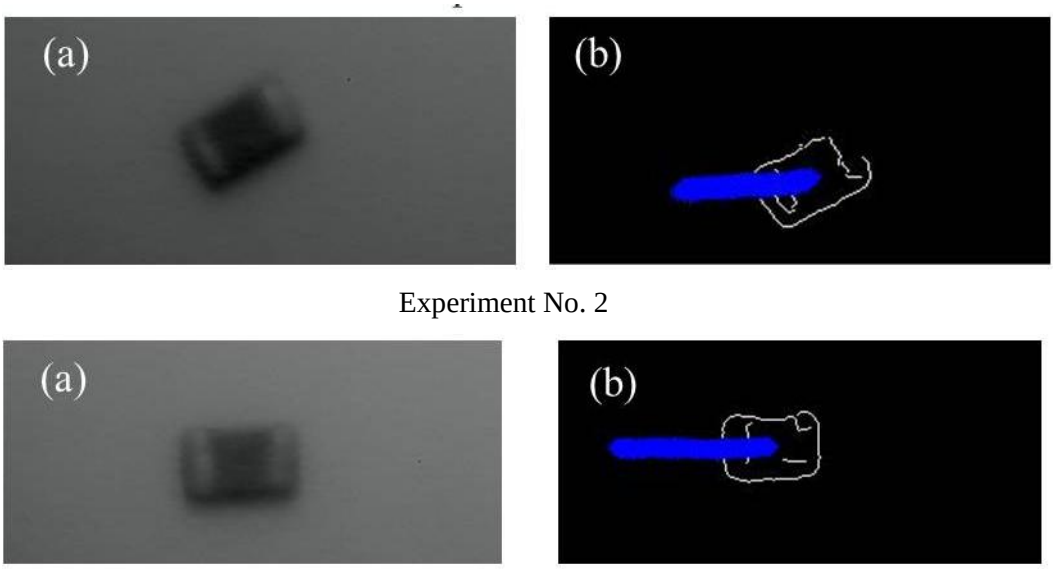

Figure 4.3 Examples experimental tracking center of micropart (a) improved image, (b) tracking center

4.2.2 Results

The effect of surface material on feeding manipulation is considered by investigating the motion of a 2012 – type capacitor at the driven frequency of 15Hz and voltage of 15.7 V. The motion of the microparts is captured at the frame rate of 500 fps. The motion of a micropart is analyzed in the horizontal (x, y) plane, and the vibration along x – direction.

Figure 4.4 plots the instantaneous velocity of a micropart on three different surfaces. It shows that micropart motion strongly fluctuated and varies with different surfaces. Furthermore, it is not shown in the figure that the motion is different for various experiments in spite of the same exciting frequency, voltage driving of the piezoelectric actuator, and the initial orientation of the micropart. The uncertainties might be due to the random surface roughness distribution an uncontrollable atmosphere. Therefore, it is unrealistic to develop a deterministic dynamic model of the motion of micropart without adding the uncertainty factor.

Although the fluctuated motion of the micropart is exhibited for a wide range of frequencies, as shown in Fig. 4.5, the first and dominant frequencies of the micropart motion on the three surfaces are 15.1 Hz. This value is close to the exciting frequencies of the surface. Moreover, the spectrum of carbide surface is the clearest. It might be explained that the real profile created on carbide material is the most approximate to the ideal saw-tooth profile while the profiles on the other material appear square-tooth with several valleys and uneven peak and depth (See Fig. 4.2). The difference in the real profiles comes from the properties of material which can stand the fabrication process. In the experiment movies, we observed that it is difficult for a micropart to move on the brass surface and the micropart travels short distances and then vibrates with a high frequency at the top point. This explains the high-frequency bundles in the tail of Fig. 4.5(a).

The variation of the displacement of the microparts along the x – direction with respect to time is plotted in Fig. 4.6. According to this figure, the average velocities of the micropart during 5.5 s which was taken from the observation of the experimental movies on the brass, zirconia, and carbide surfaces are 0.25, 0.5, and 1.5 mm/s, respectively. The carbide surface appears to be the best for the micropart feeding among the considered surfaces. A reasonable explanation of this fact is the dependence of velocity on how the real saw-tooth profile of the surface is. A more approaching to the ideal saw-profile would make a lager asymmetric contact force when the surface vibrates symmetrically. As we observed in Fig. 4.2, the profile on the brass surface is likely a square-profile which balances well the contact force then the surface moves in either negative or positive direction. Therefore, the microparts velocity on this surface is the smallest.

Moreover, due to the profile of the surface, micropart fluctuated strongest on the brass surface and slightest on the carbide surface as shown in Fig. 4.6. Comparing the relation between the velocity and velocity spectrum clarity, the micropart moved faster when spectrum is clear.

Figure 4.6 also plots the motion of microparts in y – direction. It shows that the motion in the y – direction is much lesser than that in the x – direction. This implies that the feeder system can transport unidirectionally along the vibration direction.

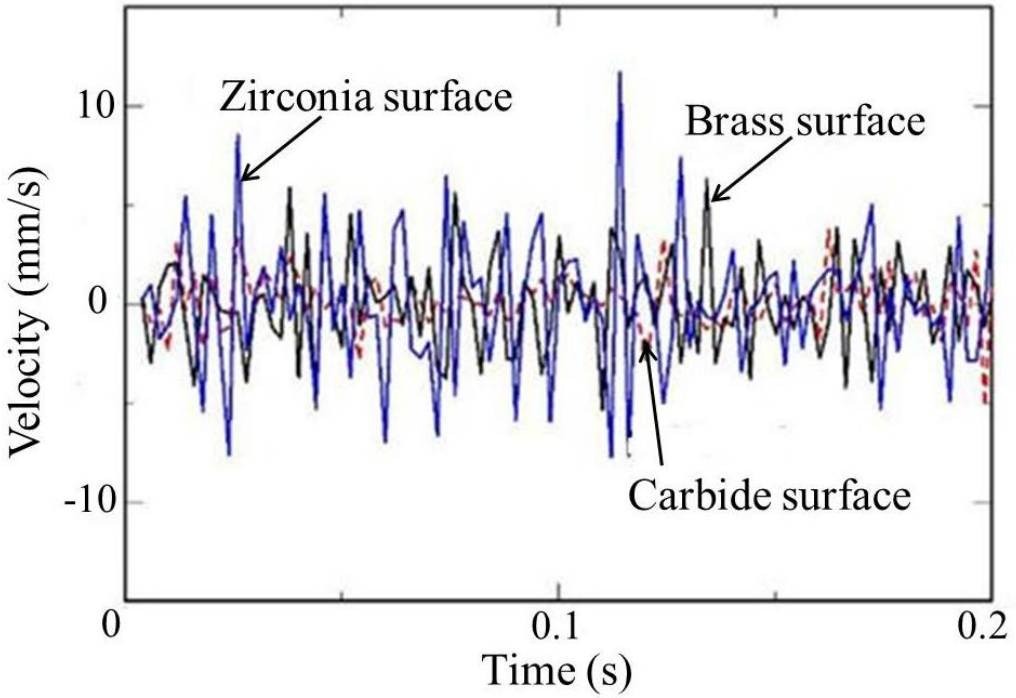

Figure 4.4 Variation in micropart velocity with time

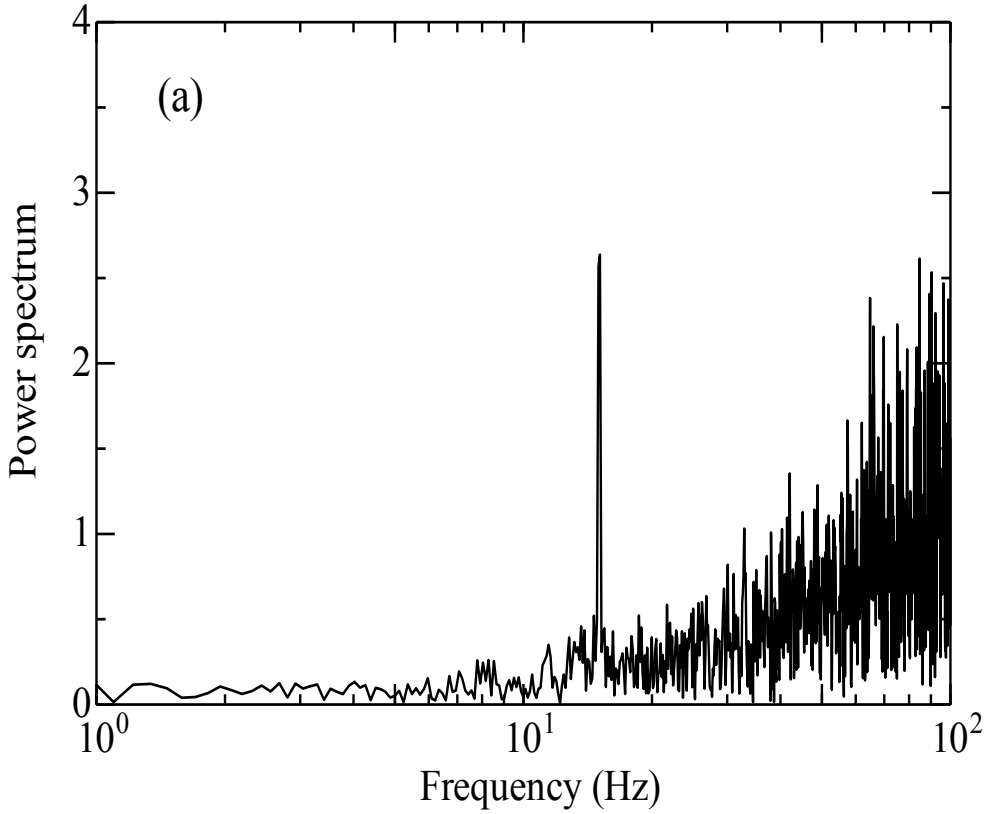

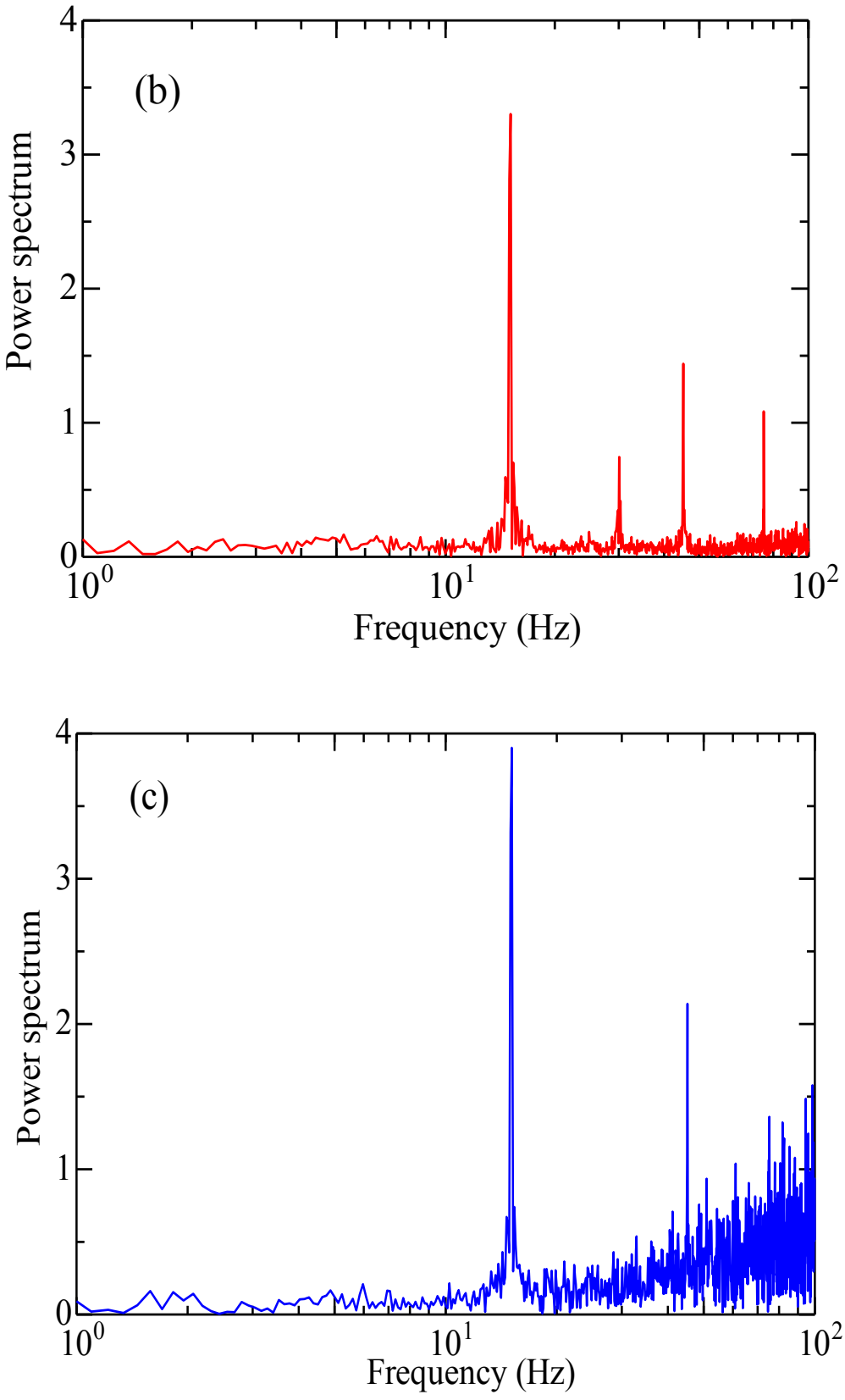

Figure 4.5 Spectrum of x-velocity on brass (a), carbide (b), and zirconia (c) surfaces

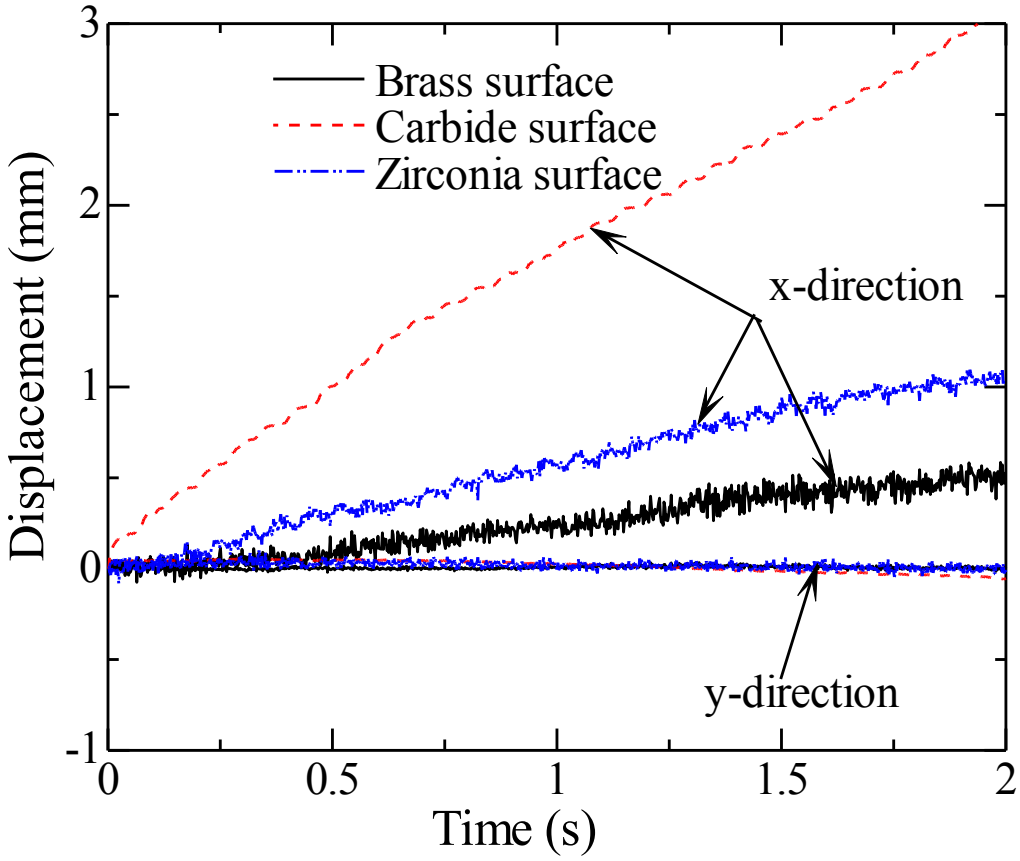

Figure 4.6 Variations in micropart displacement with time

4.3 Effect of Exciting Frequency on Motion of Microparts

Since the carbide surface provides the best solution for transporting microparts, as shown in Section 3.1, we will investigate the effect of frequency on the motion of microparts on the carbide surface only. In this section, the experiment on two types of capacitors, 2012 and 0603 capacitors is carried out. At each frequency, we performed a number of experiments for each type of capacitor. The average velocities of the microparts are summed over experiment and time.

To examine the stability in motion of the microparts, we consider the probability distribution the microparts velocity computed by

$$f(v) = \frac{n}{Ndv}, \qquad \textbf{(4.1)}$$

where n is the number of velocities whose values are within $v \pm dv/2$, dv is the infinitesimal velocity at v, and N is the number of all velocity values in our computed velocity range. In the present study, the velocity range is divided into 200 segments.

It is clear that the probability distribution with smaller standard deviation represents a more stable motion. In the present study, the standard deviation of probability distribution in Eq. (4.1) is computed by approaching $f(v)$ to a Gaussian distribution as

$$G(v) = \frac{a}{\sqrt{2\pi\sigma^2}} \exp(-\frac{(v-V)^2}{2\sigma^2}), \qquad \textbf{(4.2)}$$

where V is mean velocity, σ is standard deviation, and a is a constant to fit the peak of the distribution. The values of V, σ and a are determined by a nonlinear fitting technique which are implemented using MATLAB libraries.

Figure 4.8 plots the probability distributions at different exciting frequencies for two types of microparts and their approached Gaussian distribution. It shows that the distribution of microparts can be well approached by a Gauss distribution. Therefore, the σ value computed by Eq. (4.2) can be used to estimate velocity bias of micropart.

Figure 4.9 shows the variation of standard deviation of the velocity along x-direction with exciting frequency. In our examined frequency range, 2012 capacitor exhibits a stable motion whereas 0603 capacitor moves with strong fluctuation if the frequency is lesser than 40Hz.

Since the contact between the micropart and the saw-tooth profile can be either slope contact or point contact. The vertical motion of the microparts exists, and its average is shown in Fig. 4.10. In comparison with Fig. 4.7, the jump of the microparts is much smaller than the moving in x-direction. Furthermore, the jump magnitude of 2012 capacitor is almost constant while jump of 0603 capacitor varies with frequency. This is may be due to the effect of mass on the jumping motion where 2012 capacitor is heavier than 0603 counterpart.

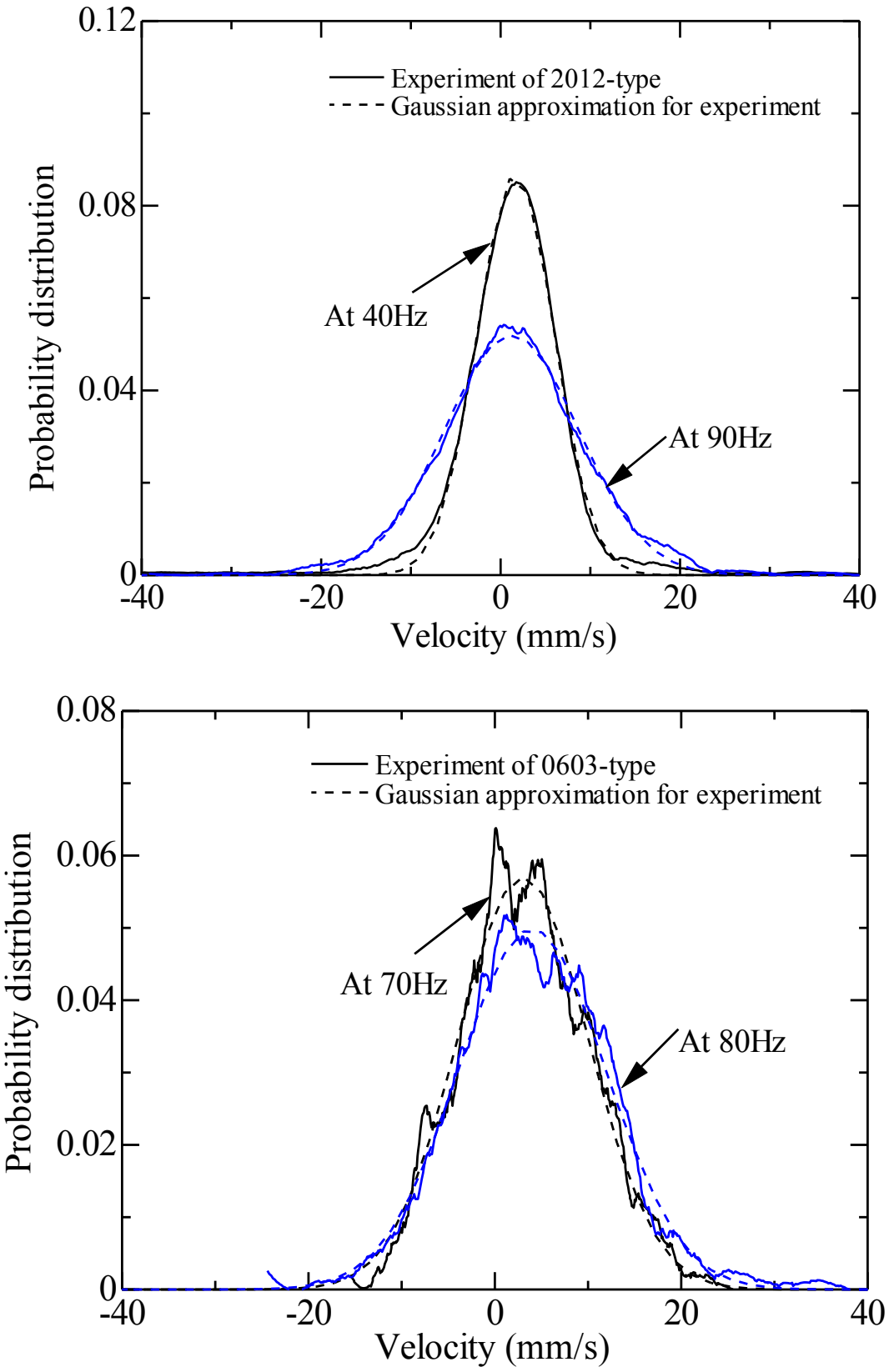

Figure 4.7 Probability distribution of micropart velocity

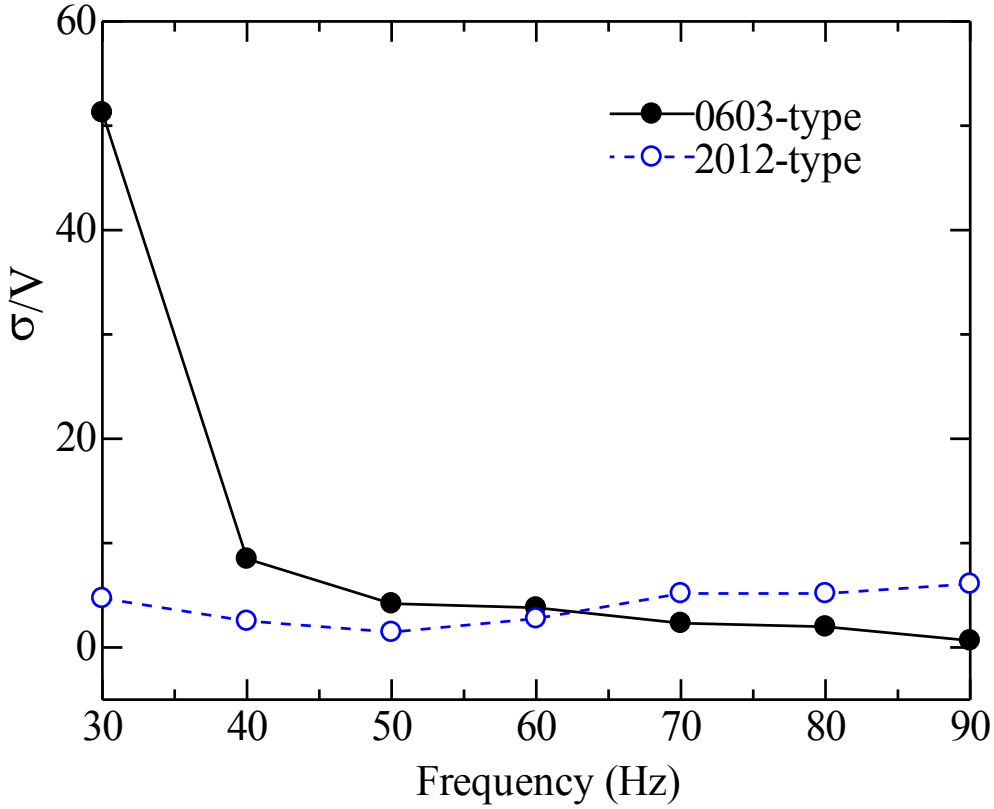

Figure 4.8 The standard deviation of velocity along x-direction at different frequencies

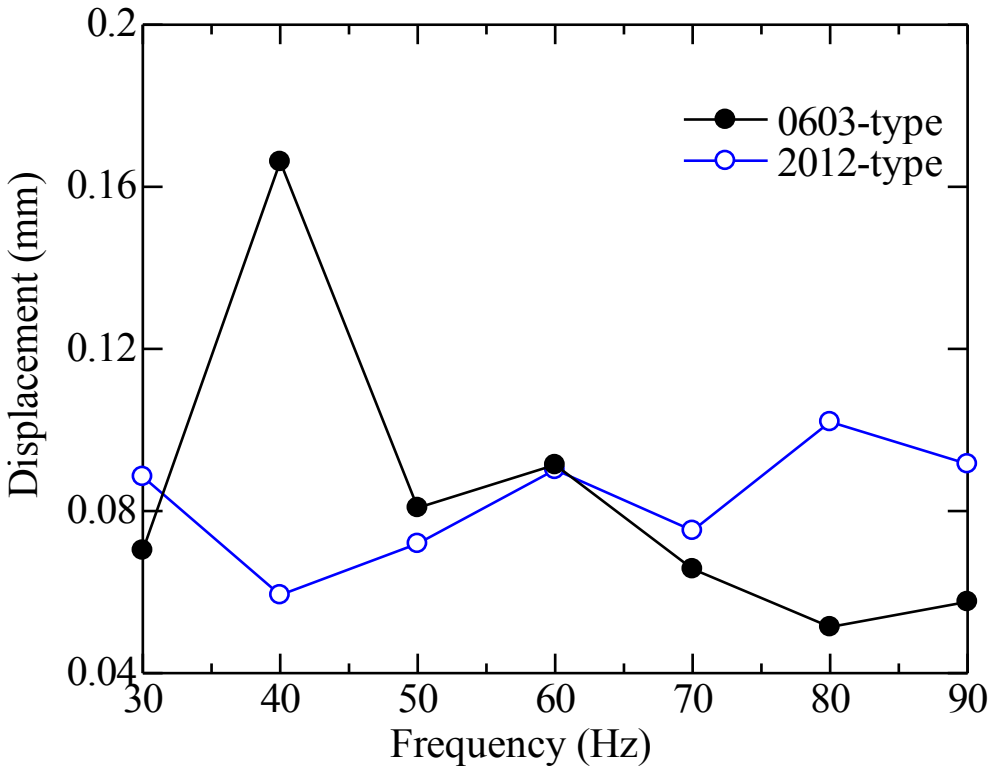

Figure 4.9 Displacement along z-direction at different frequencies

4.4 Closing remarks

This chapter investigates the effect of the patterned profile on the surface to the feeding velocity of the micropart by experiment. The instantaneous motion of a micropart on several patterned profiles was investigated by the use of PTV method. The experiments were carried out for different sizes of micropart and driven frequencies on the surfaces.

The experiment showed that the feeding velocity of the microparts depends on the patterned profile on the surface. In this study, the carbide surface showed the best results in comparison with the brass and zirconia surfaces in terms of the transportation speed, since the saw-tooth profile on the carbide surface is the most perfect. It appeared that a more approaching to the ideal saw-profile produced a lager velocity because this profile made a lager asymmetric contact force between the micropart and surface.

The motion of the microparts was demonstrated for various modes. The dominant frequency coincides with the exciting frequency. The frequencies of the other significant modes were larger than this value. It was observed that the micropart moved faster when the velocity spectrum was clearer. It seemed that in the present feeder system, the motion of a heavier micropart was more stable in a wide range of exciting frequency. It may be due to the effect of micropart mass on its motion.

Chapter 5

Effect of Geometry Parameters of Asymmetric Fabricated Surface on Micropart Feeding

This chapter presented experimentally the effect of the geometry parameters of saw-tooth surface and micropart on the motion of microparts. The experiments were performed in dimensionless parameters between the saw-tooth pitch, *p*, and micropart length, *l* to determine the important characteristic saw-tooth pitch scale and micropart length scale. The results showed that the velocity of the micropart increases up to a certain value of *pf*, which is represented for surface, and then decreases with increasing *pf*. The widths of the velocity profiles with *pf* were similar for the same value of the relative scale *l/p* but the peaks of these profiles were slightly larger and the profiles were lefty shifted for larger pitch of the saw-tooth surface. It implied that the motion of micropart depends on the characteristic surface velocity *pf* than the relative scale *l/p* and larger pitch of the saw–tooth creates a larger asymmetric force on the micropart.

5.1 Experiment Validation

5.1.1 Experiment Surface

The asymmetric structures of the surface considered in this work have different pitches depending on the fabrication technologies such as dicing or etching process as in Figs. 5.2(a) and (b). These selected asymmetric structures are the closest to the ideal saw-tooth profile which has been proved that it can transport the microparts better than other profiles.

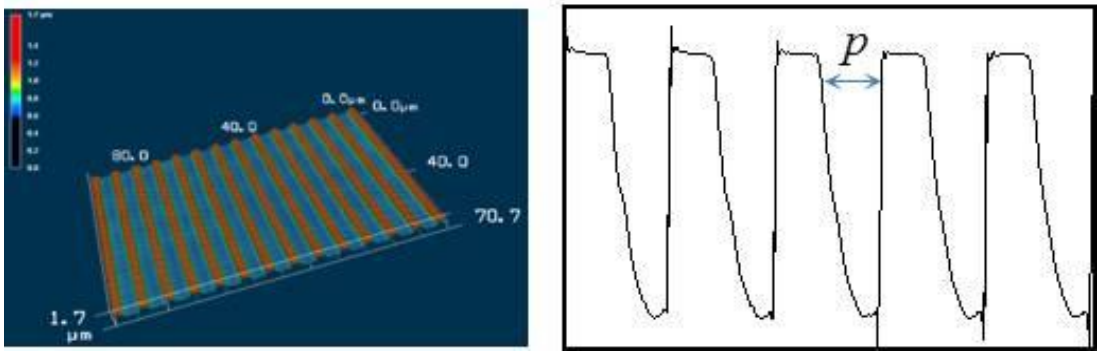

(a) p = 0.01 mm

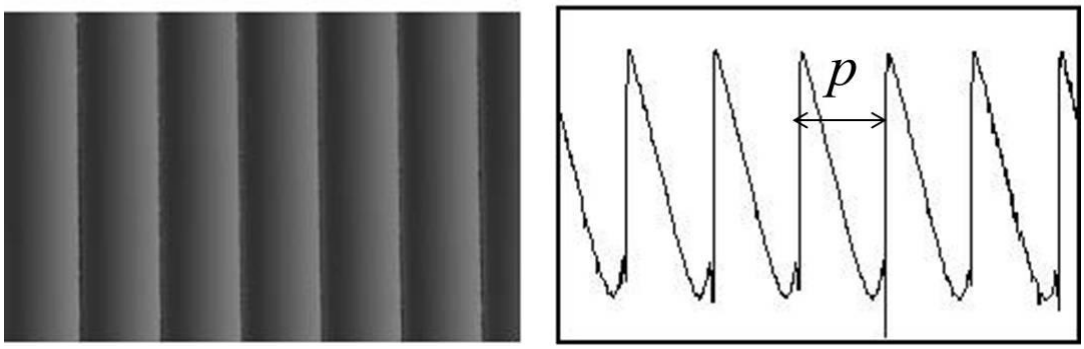

(b) p = 0.05 mm

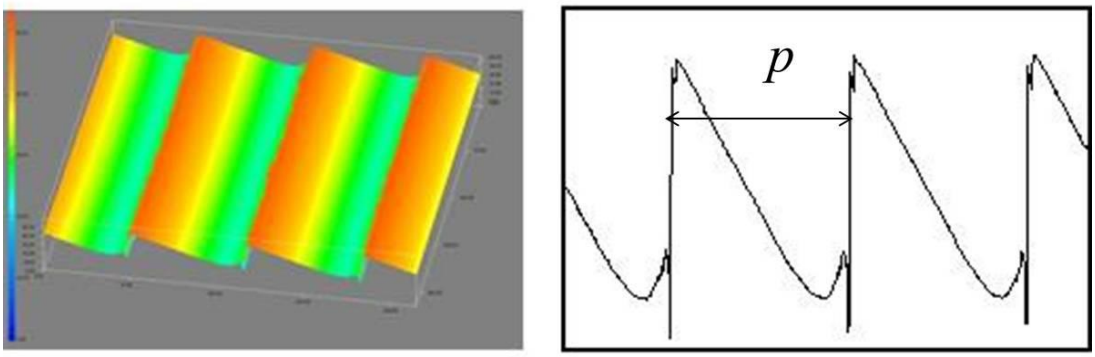

(c) p = 0.1 mm

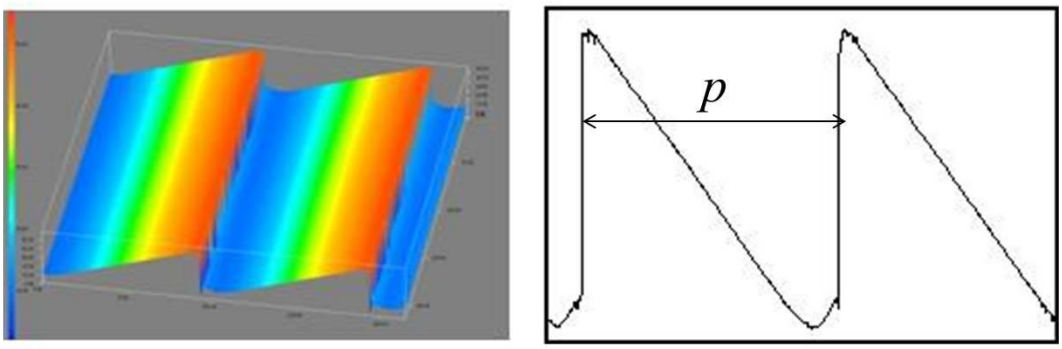

(d) p = 0.15 mm

Figure 5.1 Experimental surfaces and profiles with different saw-tooth pitches, p

The profile shown in Fig. 5.2(a) is in trapezoidal shape. However, it has asymmetric characteristic as the profiles shown in Fig. 5.2(b)-(d), since the flat portion of profile in Fig. 5.2(a) has negligible asymmetric effect on the motion of microparts. In addition, the other surfaces with different pitch of saw-tooth such as p = 0.2 mm, p = 0.4 mm, p = 0.08 mm and p = 0.06 mm were used in the present study. All of these profiles are not plot in this paper because they also have same profile shown in Fig. 5.2(b)-(d). Therefore, we assume that all profiles have the same saw-tooth profile.

We performed experiment on several microparts with different size such as ceramic chip capacitors 0402 ($l \times w \times h$ = 0.4 × 0.2 × 0.2 mm), 0603 ($l \times w \times h$ = 0.6 × 0.3 × 0.3 mm), 1005 ($l \times w \times h$ = 10 × 0.5 × 0.5 mm), 1608 ($l \times w \times h$ = 1.6 × 0.8 × 0.8 mm), and 2012 ($l \times w \times h$ = 2.0 × 1.2 × 0.6 mm) where l, w, and h are length, width, and depth of the capacitors respecting to x, y, and z direction. The x-direction is defined along the vibration motion of the surface. The z-direction is normal direction of the surface.

The considered parameters are micropart length, pitch of saw-tooth, and exciting frequencies. We assume that the asymmetry effect of all saw-teeth covered by the micropart on the micropart is proportional to the asymmetry effect of each saw-tooth. Therefore, we consider the relative scale l/p as a parameter. The second parameter is pf since it is the velocity of asymmetry. Table 5.1 shows four relative scales: l/p = 4, l/p = 10, and l/p = 20. For each of the relative scale, we have three different capacitor lengths and saw-tooth pitches.

Table 5.1 Relative scale with different saw-tooth pitches

l/p =20	Case 1	*l*	2.0 mm
		p	0.1 mm
	Case 2	*l*	1.6 mm
		p	0.08 mm
	Case 3	*l*	1.0 mm
		p	0.05 mm
l/p =10	Case 1	*l*	2.0 mm
		p	0.2 mm
	Case 2	*l*	1.0 mm
		p	0.1 mm
	Case 3	*l*	0.6 mm
		p	0.06 mm
l/p = 4	Case 1	*l*	0.6 mm
		p	0.15 mm
	Case 2	*l*	1.6 mm
		p	0.4 mm
	Case 3	*l*	0.4 mm
		p	0.1 mm

5.1.2 Tracking Method

Figure 5.2 plots the tracking center result of 0402-, 1005-, 1608-, and 2012-capacitors as examples by Otsu threshold method.

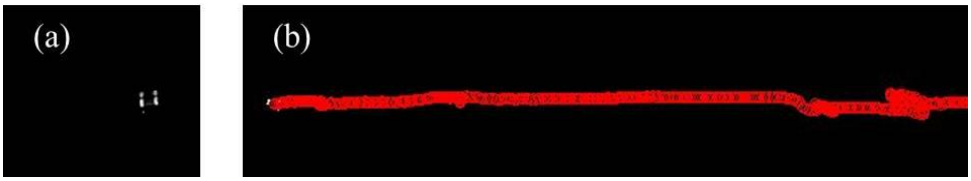

0402-capacitor

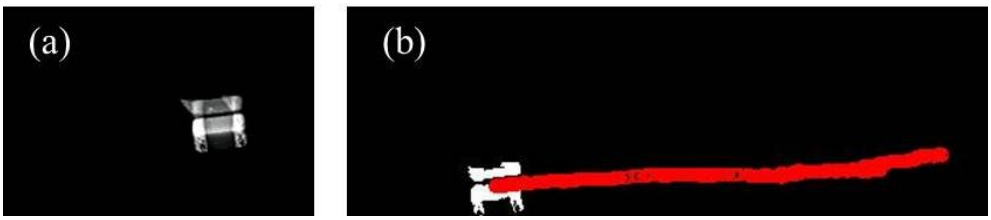

1005-capacitor

1608-capacitor

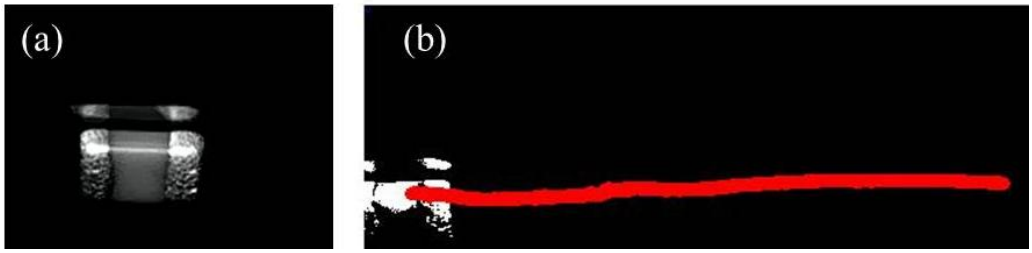

2012-capacitor

Figure 5.2 Examples experimental tracking center of microparts, (a) improved image, (b) tracking center.

5.2 Results and Discussion

We conducted experiments for range of frequency from 100 Hz to 160 Hz with the interval of 10 Hz. To compute the ensemble-averaged velocity, each experiment setup is repeated eight times.

Figures 5.3–5.5 show the ensemble averaged velocity of microparts against the characteristic velocity of the surface *pf* at the same ration *l*/*p* for different pitches *p*. The values of *l* and *p* are shown in Table I. They show that the velocity increases up to a certain value of *pf* and then decreases with increasing *pf*. It is observed that the profiles are shifted to the right along *pf* axis for larger *p*. The widths of the profiles are similar but the peaks of the profiles are higher for larger *p*. In the other words, microparts move faster on the surface which has larger saw–tooth pitch. A possible reason for this observation is that a larger pitch of saw–tooth produces a stronger asymmetric force on the micropart.

We assume that the total force, *F*, on the micropart is equal to the sum of the individual asymmetrical force, F_i, caused by each saw-tooth covered by the micropart as

$$F = \sum_{i=1}^{N} F_i$$

where $N \approx l/p$ is number of saw-tooth covered by the micropart as illustrated in Fig. 5.6. Therefore, the lower peaks of the velocity profiles for smaller *p* as shown in Figs. 5.3–5.5 indicate that F_i is smaller. In other words, the asymmetric force of each saw–tooth is smaller for smaller saw–tooth pitch.

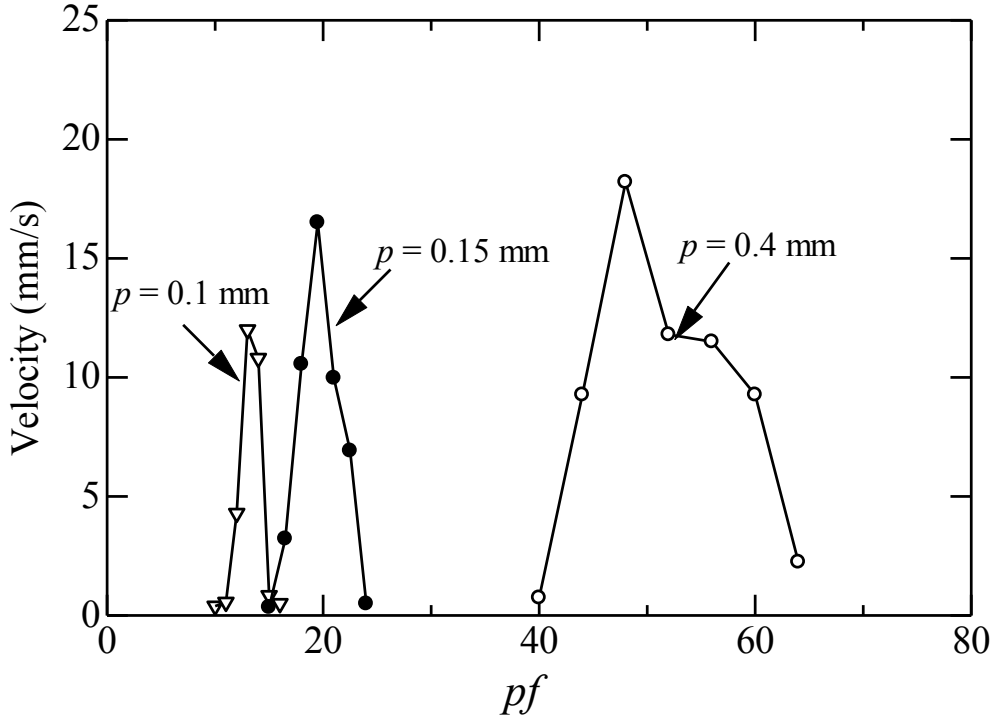

Figure 5.3 The variation of micropart velocity with analysis feeding microparts for the same value of ratio *l/p* = 4 runs with frequencies

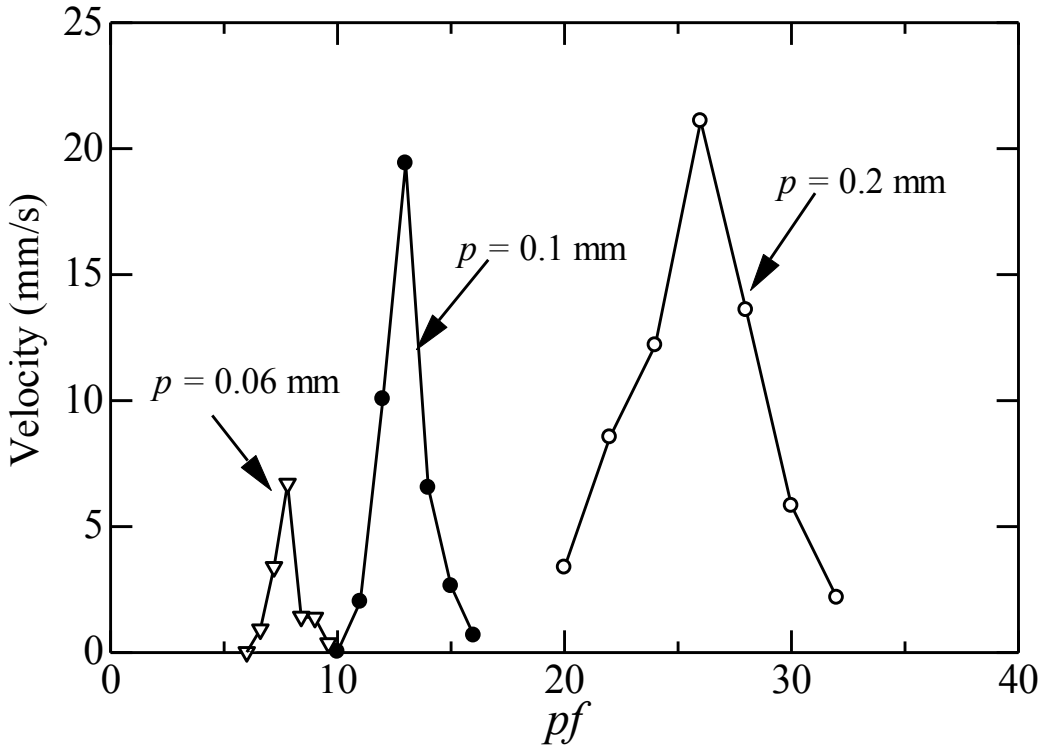

Figure 5.4 The variation of micropart velocity with analysis feeding microparts for the same value of ratio *l/p* = 10 runs with frequencies

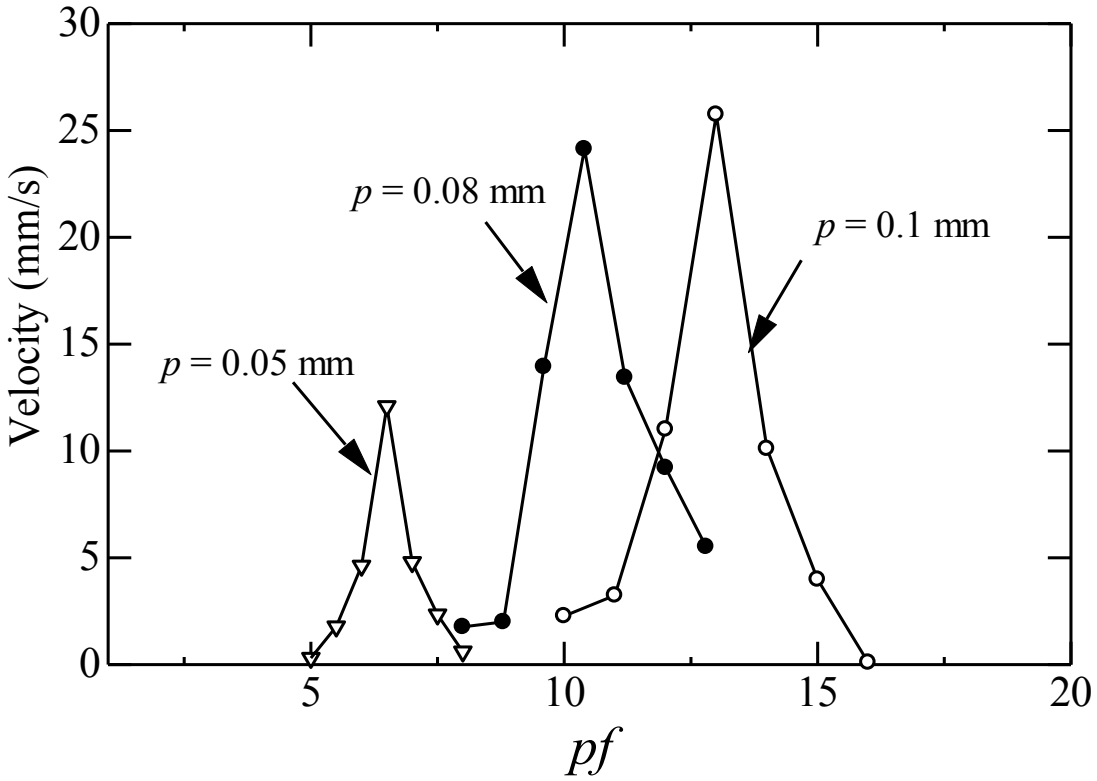

Figure 5.5 The variation of micropart velocity with analysis feeding microparts for the same value of ratio l/p = 20 runs with frequencies

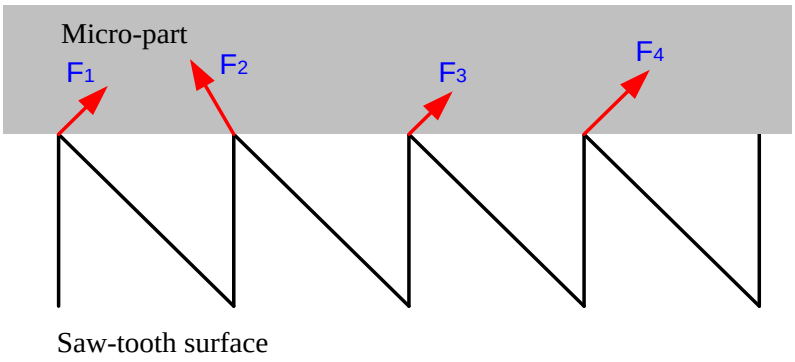

Figure 5.6 Diagram of individual asymmetrical force on a micropart

5.3 Closing remarks

We have studied experimentally the effect of the geometry parameters of asymmetrical structured surface and of micropart on the motion of micropart. The experiments were carried out on surfaces whose asymmetric structures were close to the saw–tooth profile for various frequency *f* applied on the surface. The saw–tooth pitches

were in sub–millimeter scale. The velocity of the micropart was measured by PTV method. The length of micropart, *l*, and pitch of the saw-tooth, *p*, were selected so that constituted to several relative scales of micropart length to the saw-tooth pitch. We found that for the same value of the relative scales widths of the velocity profile against *pf* were similar for the same relative scale *l/p* but the peaks of the profiles were higher for larger pitch of the saw–tooth. In the other words, micropart moves faster on the surface having larger pitch of saw-tooth. It implies that larger pitch creates stronger asymmetrical force on the micropart. It is important to develop theoretical relationship between the parameter *pf* and micropart velocity. This means how to relate peaked velocities at each case each other. If a theoretical function, such as linear function, is appeared, we can access the experimental results more strictly.

The analysis in this chapter has been done based on velocity. In future work, we will try to analysis based on inertial because micropart scale change brings micropart weight change.

Chapter 6

Two-Dimensional Modeling Micropart Feeding on a Saw-tooth Surface with Symmetric Vibration

In this chapter, we proposed a dynamic simulation model for the micropart feeding that describes the planar motion modes of the micropart including two linear motions and one rotational motion, on a saw-tooth surface. In the simulation, the contact between the micropart and saw–tooth surface was assumed to be the contact between a number of hemispheres on the micropart and the surface, which results in either a point contact or slope contact. The effect of the saw–tooth surface roughness on the contact force was modeled as a normal vector. In addition, the roughness of the saw–tooth surface is approximated by superposing white noise on an ideal saw–tooth profile and is used to evaluate the adhesion force. We also considered the effect of the air drag on the feeding velocity of the sub-millimeter sized parts. The results showed that the model could describe the motion modes of a micropart and the two linear motions were in good agreement with the experimental data. The proposed model could be used to improve the design of surfaces for micropart transport.

6.1 Dynamic model of micropart on the asymmetric fabricated surface

6.1.1 Micropart surface profile model

The authors (Mitani *et al.* 2006) suggested that the contacts between a micropart and a saw-tooth surface are the contacts between the convexities on the electrodes of the micropart and the saw-tooth surface. Each convexity on the electrodes of a capacitor was defined as a hemisphere. In this study, a 2012 capacitor shows one of the consumer products provided by TDK Cooperation is used in Fig. 6.1(a). The dimensions of the part are 2.0 × 1.2 × 0.6 mm^3 in length, width, and depth, respectively. The four highest convexities are found, and in the present study, we assume that the convexities on the electrode surface are four hemispheres, as shown in Fig. 6.1(b) and (c). The parameters l and w are the length and width of the micropart, respectively, and r is the radius of the hemisphere, which is selected depending on the relative contact given by Mitani *et al.* 2006.

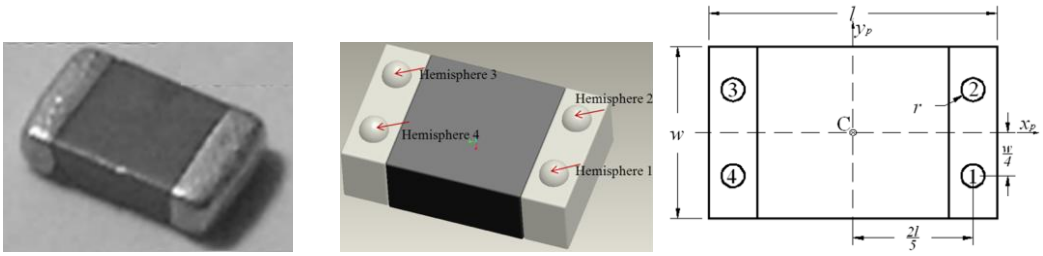

(a)The real 2012 capacitor (b) 3D model of 2012 capacitor (c) Hemisphere positions of 2012 capacitor

Figure 6.1 Model of 2012 capacitor

6.1.2 Transition among contact conditions

Let us assume that the convexity center O moves between the K^{th} and the $(K\text{-}1)^{th}$ saw-teeth as shown in Fig. 6.2. Four contacts occur according to the relative position of the convexity and these saw-teeth:

1) Point contact with $(K\text{-}1)^{th}$ saw-tooth;
2) Point/slope contact;
3) Slope contact with the K^{th} saw-tooth;
4) Point contact with the K^{th} saw-tooth.

Let O = (x, y) be the position of the convexity center, S_k = (x_k, y_k) and S_{k-1} = (x_{k-1}, y_{k-1}) be the position of the two saw-teeth, ϕ_{k-1} be the angle of the point contact with the (K - 1)th saw-tooth, and ϕ_0 be the angle of the slope contact with the K^{th} saw-tooth, respectively. The above four contacts occur when the following conditions, respectively, are satisfied:

1) $x_{k-1} \le x \le x_{k-1} + r\cos\phi_{k-1}$;
2) $x = x_{k-1} + r\cos\phi_{k-1}$;
3) $x_{k-1} + r\cos\phi_{k-1} < x \le x_k - r\sin\theta$;
4) $x_k - r\sin\theta < x \le x_k$;

where $\phi_{k-1} = \theta + \sin^{-1} x\left(1 - \frac{p}{r}\sin\theta\right)$

$$\phi_0 = \frac{\pi}{4} + \theta.$$

Table 6.1 Transition of contact force

Relative position	Relative motion	Contact force
1	Left	Zero
	Right	Point contact
2	Left	Slope contact
	Right	Point contact
3	Left	Slope contact
	Right	Zero
4	Left	Point contact
	Right	Zero

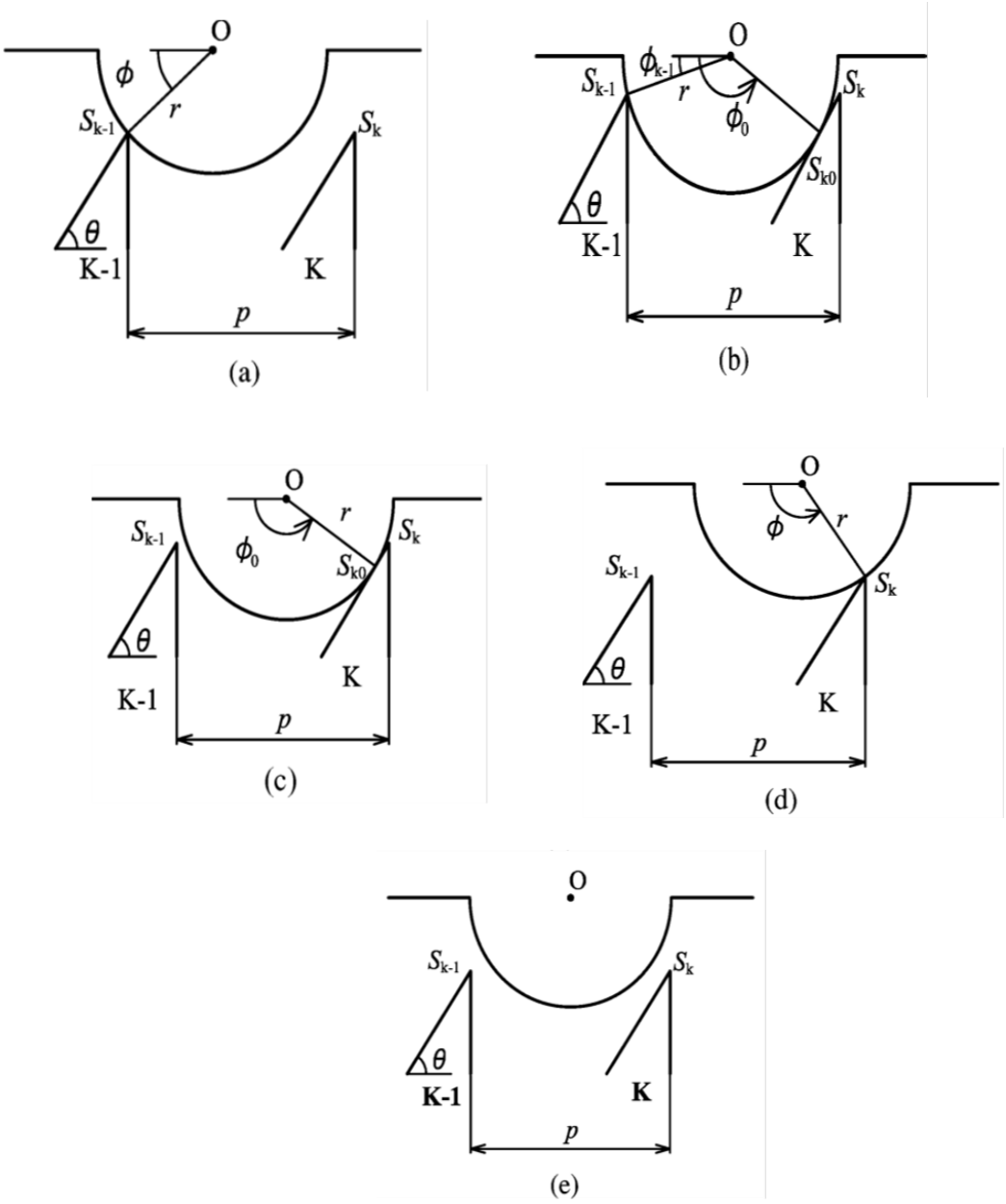

Figure 6.2 Contacts of a convexity and two saw-teeth

The contact force changes with the relative positions of the saw-tooth and microparts. When the convexity is not in contact with any saw-tooth, as shown in Fig. 6.2(e), the contact force vanishes. Especially in the case of the point/slope contact, the contact force changes according to the relative motion between the saw-tooth and the microparts. Table I summarizes the contact forces, and the relative positions/motions of the saw-teeth and microparts.

Next, consider the saw-tooth pitch p. No contact occurs when p is larger than $p = r(1 + \sin\theta)/\sin\theta$, which causes a reduction in the feeding velocity. Slope contact does not occur when $p \leq 2r\ sin\theta$, which makes it impossible to feed a micropart unidirectionally. Consequently, the saw-tooth pitch should be selected as

$$2r\ sin\theta \leq p < r\frac{1+sin\theta}{sin\theta}. \quad \textbf{(6.1)}$$

6.1.3 Equation of micropart motion

To describe the motion of a micropart, we define two coordinates: *O-xy* is frame-fixed to space, and *C-*$x_p y_p$ is frame-fixed to a micropart. The coordinate (x_c, y_c) is referred to as the position of a micropart in the *O-xy* frame, and φ_c is the orientation angle of the micropart, as shown in Fig. 6.3. The linear velocity vector of the micropart is described by the equation(v_{yc}, v_{yc}) = ($\dot{x}_c, \dot{y}_c$), and the angular velocity is described by the equation $\dot{\omega}_c = \dot{\varphi}_c$.

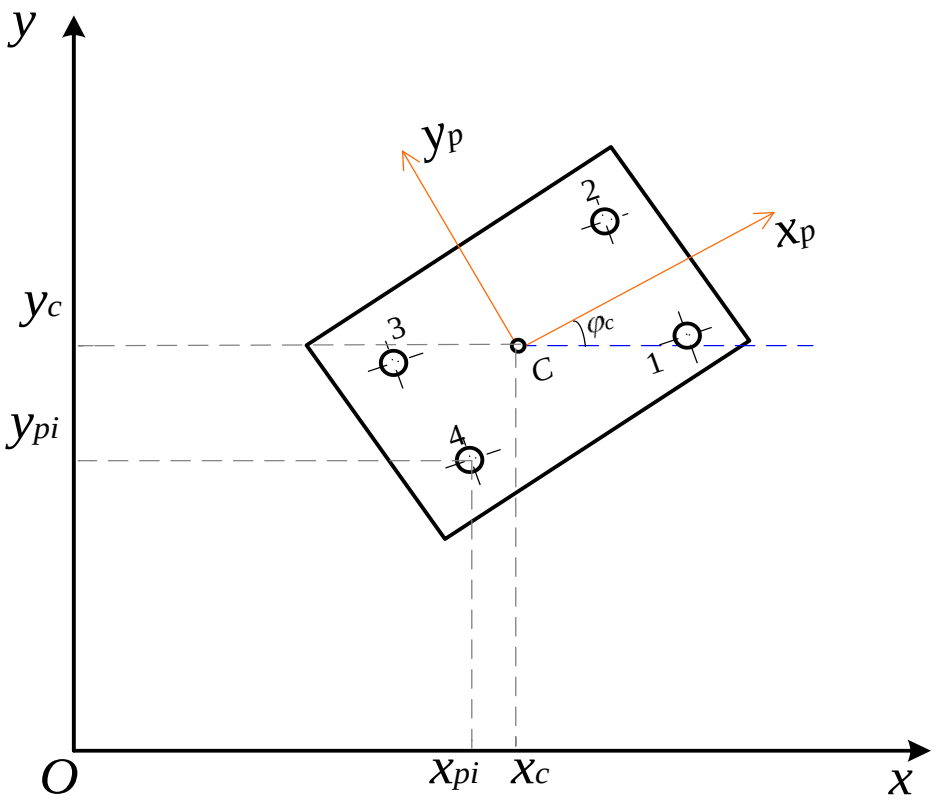

Figure 6.3 Coordinates of micropart transferred from hemispheres

The motion of a micropart obeys Newton's second law as follows:

$$m\begin{bmatrix}\dot{v}_{xc}\\ \dot{v}_{yc}\end{bmatrix}=\begin{bmatrix}F_x\\ F_y\end{bmatrix}-c\begin{bmatrix}v_{xc}\\ v_{yc}\end{bmatrix}$$
$$I\dot{\omega}_c=\tau_z-d\omega_c \quad , \tag{6.2}$$

where c and d denote the linear and rotational damping coefficients, respectively; m and I are the mass and inertia moments in relation to the center of the micropart, respectively; τ_z is the torque; and $[F_x, F_y]^T$ are total forces F_{total} that are the result of the driving force and surface force and air drag applied to the micropart.

$$\vec{F}_{total}=\vec{F}_{driving}+\vec{F}_{surface}+\vec{F}_{drag} \tag{6.3}$$

6.1.4 Driving force

In this study, the variation of the driving force vector due to the roughness of the saw-tooth surface is simulated by randomly generating a normal vector, as shown in Fig. 6.4. At each contact point, the driving force is along the direction of the normal unit vector.

For example, when a slope contact occurs, the normal vector, n, is formulated in the O_s-$x_s y_s$ coordinate system, which is oriented to the slope of the surface, as shown in Fig. 6.5.

$$\begin{bmatrix}n_{s\_x}\\ n_{s\_y}\\ n_{s\_z}\end{bmatrix}=\begin{bmatrix}\sin\theta_s\cos\varphi_s\\ \sin\theta_s\sin\varphi_s\\ \cos\theta_s\end{bmatrix}. \tag{6.4}$$

The normal vector, n, should be close to the z_s axis if the angles θ_s and φ_s have small values. In this study, we generate normal vectors within $[-20^0, 20^0]$ with a normal distribution.

The three components of the normal vector, *n*, are expressed in the global coordinates *O-xy*, as defined by Eq. (6.5), using the Euler rotation rule about the *y*-axis with the angle of - θ as

$$\begin{bmatrix} n_x \\ n_y \\ n_z \end{bmatrix} = \begin{bmatrix} \cos(-\theta) & 0 & -\sin(-\theta) \\ 0 & 1 & 0 \\ \sin(-\theta) & 0 & -\cos(-\theta) \end{bmatrix} \begin{bmatrix} n_{s\_x} \\ n_{s\_y} \\ n_{s\_z} \end{bmatrix}. \quad \textbf{(6.5)}$$

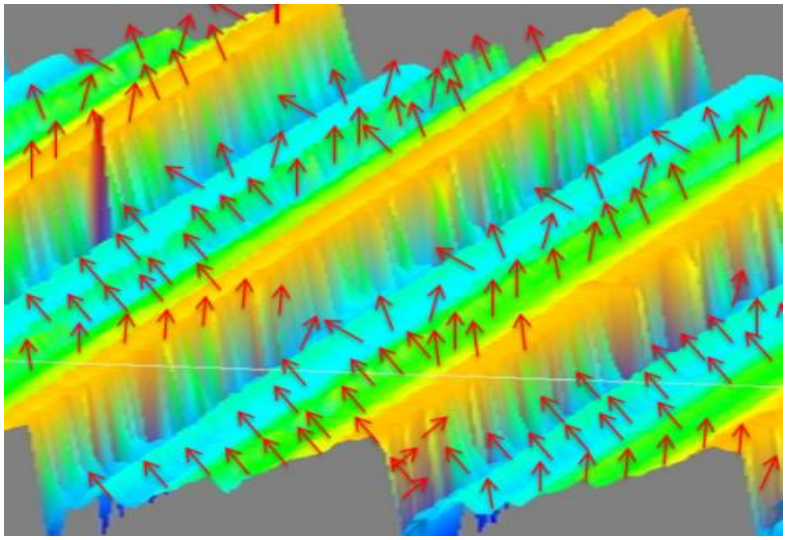

Figure 6.4 Pseudo vector field normal to saw-tooth surface

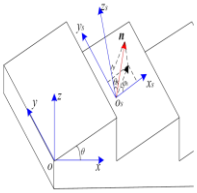

Figure 6.5 Saw-tooth surface

Thus, the driving force components along the directions of the *x*-, *y*-, and *z*-axes are

$$\begin{bmatrix} F_{c\_x} \\ F_{c\_y} \\ F_{c\_z} \end{bmatrix} = \|F_c\| \begin{bmatrix} n_x \\ n_y \\ n_z \end{bmatrix}, \quad \textbf{(6.6)}$$

where the magnitude of the driving vector force, F_c, on the *i-th* hemisphere can be determined from the relative position and velocity of the hemisphere, x_{pi}, v_{pi}, and those of the nearest peak of the saw-tooth surface, x_s, v_s, as proposed in (Mitani *et al.* 2006).

The driving torque, τ_z, can be obtained from the force as

$$\tau_z = \sum_{i=1}^{4} \left[F_{c\_yi}(x_{pi} - x_c) - F_{c\_xi}(y_{pi} - y_c) \right]. \quad \textbf{(6.7)}$$

6.1.5 Surface friction force

Let us analyze the surface force of a fabricated surface. The surface force is assumed to be the sum of the Coulomb friction and the resistance force caused by the adhesion force between a micropart and a surface. The latter is referred to as the "adhesion friction". Let g be the gravity, μ_m be the Coulomb friction coefficient, and F_r be the adhesion friction. The surface force F_s can be expressed as follows:

$$F_s = \mu(d_g)mg = \mu_m mg + F_r. \quad \textbf{(6.8)}$$

Let F_{ad} be the ahesion force between a micropart surface and the bottom surface of a groove, as shown in Fig. 6.7 (a). Area of the bottom surface is given by $dS = \omega dx$. Recall that the adhesion force is proportional to the surface area. Then, we have the following equations:

$$F_{ad}(dS, d_g) = \beta(d_g)dS \quad \textbf{(6.9)}$$

where $\beta(d_g)$ is a proportionality constant.

Assume that the adhesion friction is porportional to the adhesion force. Let μ_{ad} be the ashesion coefficient, and $\Delta F_r(dS)$ be the adhesion friction over a small area dS. Then, the adhesion friction is expressed as:

$$\Delta F_r(dS) = \mu_{ad} F_{ad}(dS, d_g) = \mu_{ad}\beta(d_g)dS. \quad \textbf{(6.10)}$$

Note that $\mu_{ad}\beta(d_g)$ is independent of the area dS.

Let us formulate the adhesion friction caused by the surface shown in Fig. 6.7(b). The distance between a micropart and a surface at coordinate x is expressed as $d_g(x)$. Intergrating the adhesion friction over small areas, we get the total adhesion friction as follows:

$$\mathrm{F_r} = \int_0^{p_n} \mu_{ad}\beta\left(d_g(x)\right)\omega dx = \mu_{ad}\omega \int_0^{p_n} \beta\left(d_g(x)\right)\mathrm{dx}. \quad \textbf{(6.11)}$$

Equation (6.11) is applied to a fabricated surface shown in Fig. 6.6. Let S0 ≅ ωpn be the surface area of a micropart. In the case of the no-fabricated surface, that is $d_g = 0$, F_r can be represented as follows:

$$F_r = \mu_{ad}\omega \int_0^{p} \beta\left(d_g(x)\right)dx = \mu_{ad}S_0\beta(0). \quad \textbf{(6.12)}$$

Substituting (6.12) into (6.8), we have

$$\mu(0) = \mu_m + \frac{\mu_{ad}\beta(0)}{mg}S_{0.} \quad \textbf{(6.13)}$$

Similarly, when the surface is fabricated with the groove depth d_g, as described in Fig. 6.6, a half of the surface area remains non-fabricated. That is, we have the following equation:

$$F_r = \mu_{ad}\omega\left\{\int_0^{p_n/2}\beta(0)dx + \int_{p_n/2}^{p_n}\beta(d_g)dx\right\} = \mu_{ad}\frac{S_0}{2}\{\beta(0) + \beta(d_g)\}.$$

(6.14)

Substituting (6.14) into (6.8), we have

$$\mu(d_g) = \mu(0) - \frac{\mathrm{S_0}}{2}\frac{\mu_{ad}\left(\beta(0) - \beta(d_g)\right)}{mg}. \quad \textbf{(6.15)}$$

Then, the ration $\mu(d_g)/\mu(0)$ is given by

$$\frac{\mu(d_g)}{\mu(0)} \equiv 1 - \frac{S_0}{2}(\mu_g(0) - \mu_g(d_g)) \quad \textbf{(6.16)}$$

where

$$\mu_g(d_g) = \frac{\mu_{ad}\beta(d_g)}{\mu(0)mg} \quad \textbf{(6.17)}$$

From Eq. (9) in (Mitani *et al.* 2006) and (6.16), the following equation is dervived:

$$\mu_g(d_g) = \mu_g(0) - \frac{2a}{S_0}\left(1 - e^{-\alpha \times d_g}\right). \quad \textbf{(6.18)}$$

Substituting (6.18) and (6.18) into (6.11), we have

$$F_r = \int_0^p \mu(0)mg\left\{\mu_g(0) - \frac{2a}{S_0}\left(1 - e^{-\alpha \times d_g(x)}\right)\right\}\omega dx. \quad \textbf{(6.19)}$$

We analyze the adhesion friction caused by a saw-tooth surface shown in Fig. 6.9. The local distance *dg(x),* as defined in Fig. 6.8, between the bottom surface of the micropart and the real saw-tooth surface is expressed as

$$d_g(x) = d - \frac{d}{p}x + \delta(x) \quad \textbf{(6.20)}$$

In Eq. (6.20), white noise, $\delta(x)$, is subject to a Gaussian distribution with a μ of zero and a σ^2 of 1.

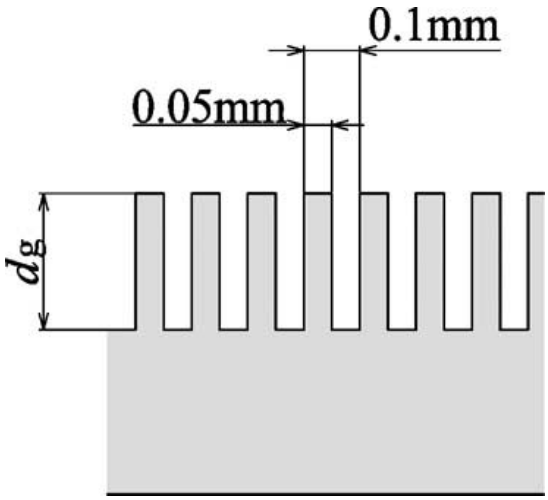

Figure 6.6 Cross section of the fabricated surface

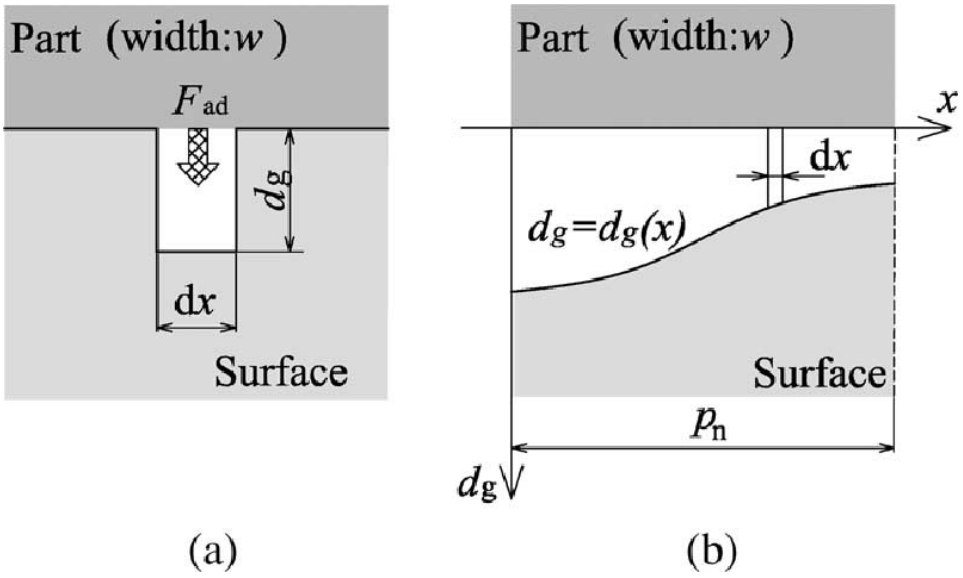

Figure 6.7 Adhesion friction model

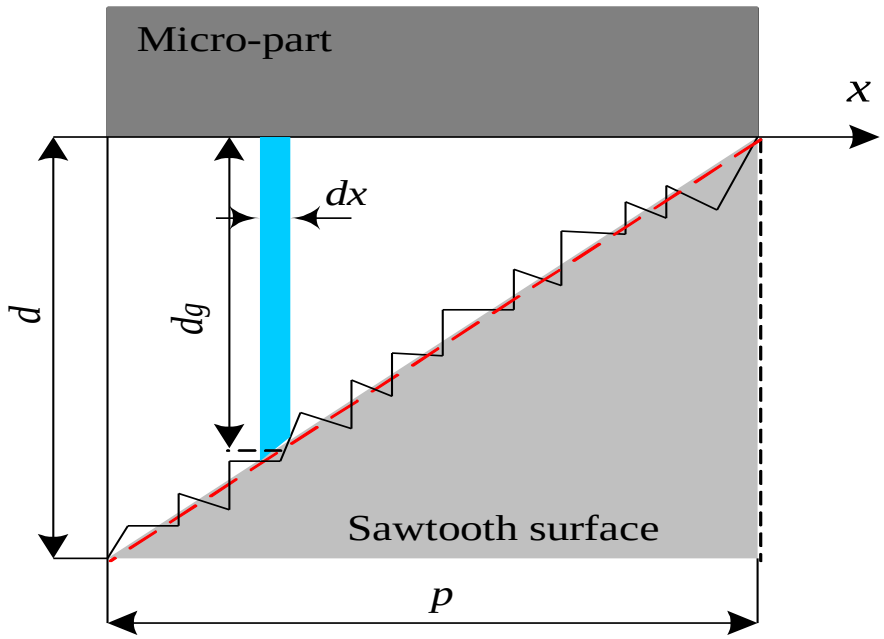

Figure 6.8 Model of adhesion force on saw-tooth

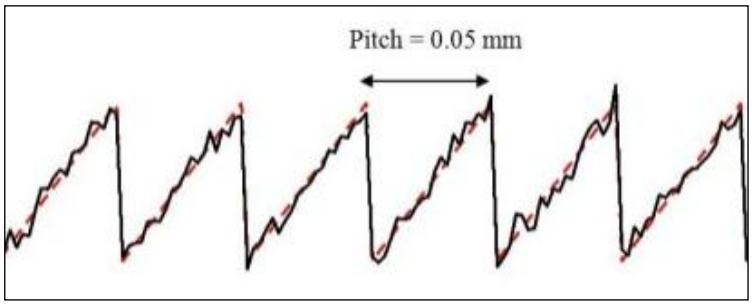

Figure 6.9 Approximate saw-tooth profile; dashed red line represents ideal saw profile; solid black line represents real saw-tooth profile approximated by adding white noise to ideal profile

6.1.6 Air Drag

The air drag force $\vec{F}_{drag}$ represents the drag due to the friction between the moving micropart with the surrounding air, which can be expressed as the below form

$$\vec{F}_{drag} = -\frac{1}{2} C_d A \rho \|v\| \vec{v}, \qquad \textbf{(6.21)}$$

where C_d is empirical drag coefficient, A denoted the cross-sectional area, and ρ is the air density.

6.2 Numerical Scheme using Matlab software

A set of ordinary differential equations, as shown in equation (6.2), is solved by a fifth-order Runge-Kutta method, as shown in Fig. 6.10, where x_s is the position of the saw-tooth in the *O-xy* coordinate system and v_s is the velocity of the saw-tooth surface. The excited frequency and amplitude of the surface vibration in the simulation are 15Hz and 0.5mm, respectively which are the same as the experiment parameters.

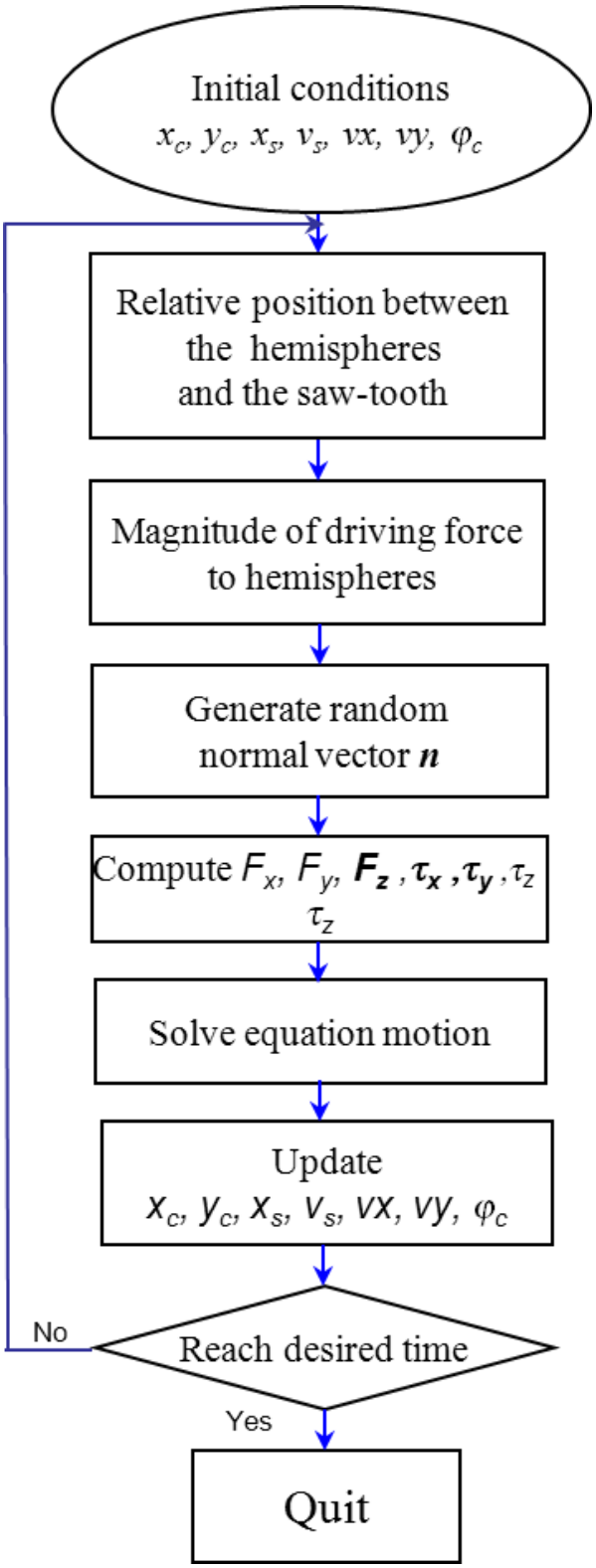

Figure 6.10 Flow chart for simulation of micropart motion

6.3 Comparison of experiments and simulation results

6.3.1 Comparison of experiments and simulation with the effect roughness of surface

We conducted the simulation for 2012-type capacitors, which were used in our previous study in Chapter 4, where the velocity and displacement of the capacitor were measured by the particle-tracking velocimetry (PTV) method. The planar motion of the capacitor is defined in the (x,y) plane where the vibration direction is along the x-direction. Herein after, the results are considered to be average representations of the repeated experiments.

Figure 6.11 shows the ensemble averaged velocity of micropart of several simulation runs with time. The micropart motion fluctuates significantly and varies along the surface profile. Furthermore, the motion is different for various simulations, which are not shown in the figure, in spite of having the same excitation frequency and initial orientation of the micropart. This implies that the model can consider the effect of uncertainties on the micropart motion that was observed in our previous experiment in Chapter 4.

Figure 6.12 shows the spectrum of a micropart velocity along the vibration direction determined by a fast Fourier transform. Although the motion of the micropart fluctuates for a wide range of frequencies, the first dominant frequency of the micropart on the surface is 15.1 Hz. In addition, the motion modes obtained by the simulation are in good agreement with those obtained in the experiment. The difference in the peaks at low frequencies may be due to the artificial low frequencies added by white noise.

The ensemble averaged displacement of a micropart along the x- and y-directions with respect to time is shown in Fig. 6.13 for the experiment and the simulation with and without the roughness effects. Good agreement between the experiment and simulation with the roughness effect is observed, whereas the simulation without the roughness effect is different from the experimental results in both the x and y motions. The figure also shows that the motion in the y-direction is significantly less than that in the x-direction. This implies that the feeder system can transport parts in one direction, which coincides with the vibration direction.

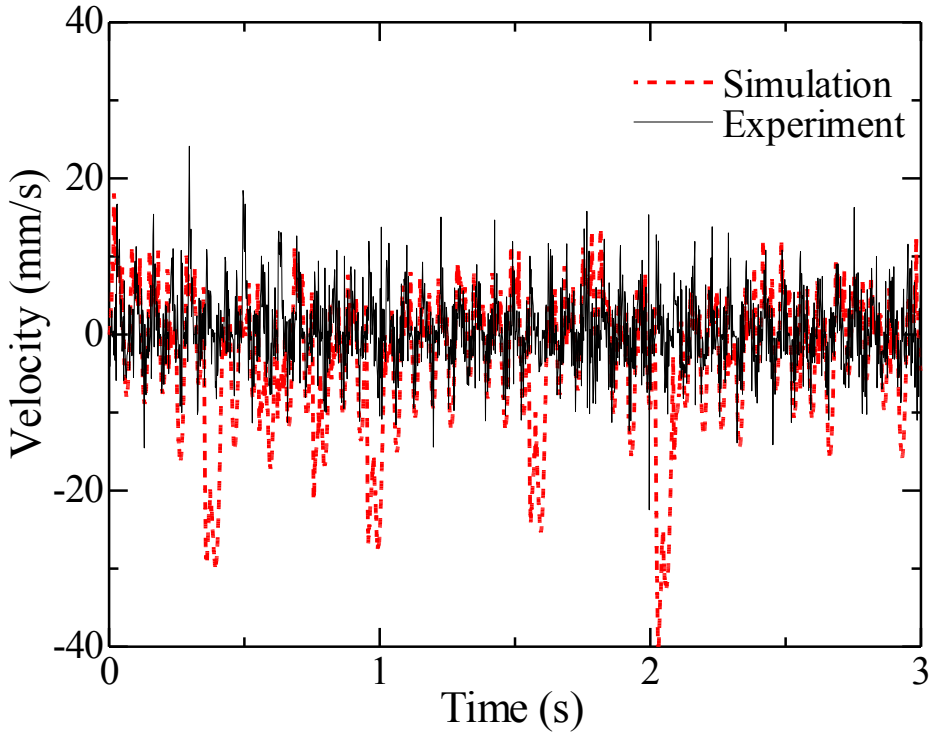

Figure 6.11 Velocity of micropart x-component with respect to time

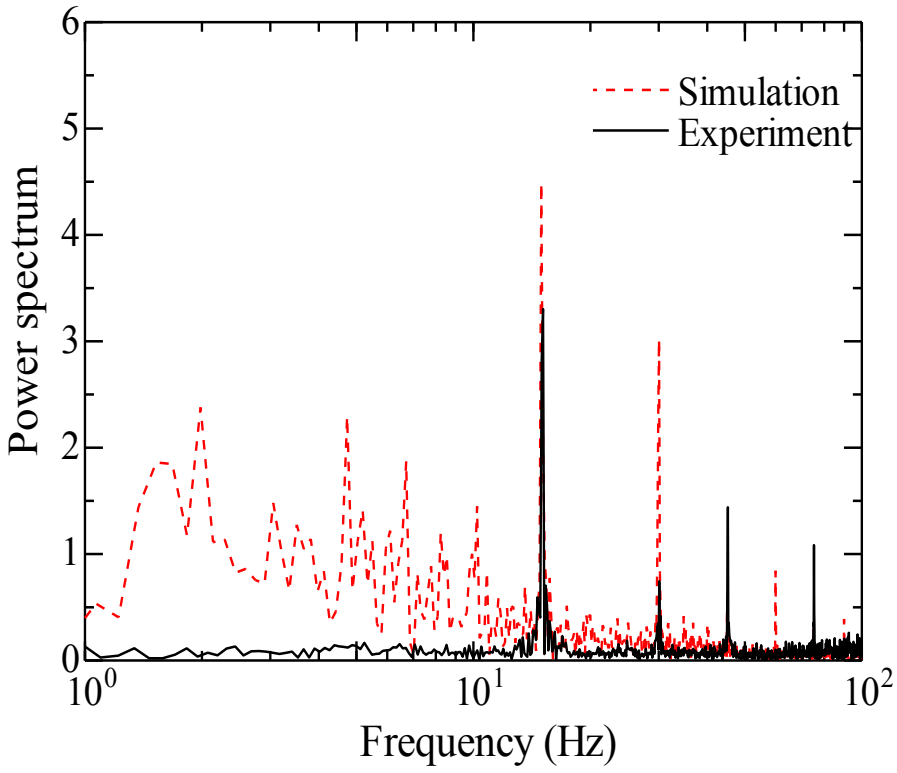

Figure 6.12 Spectrum of velocity along x-direction

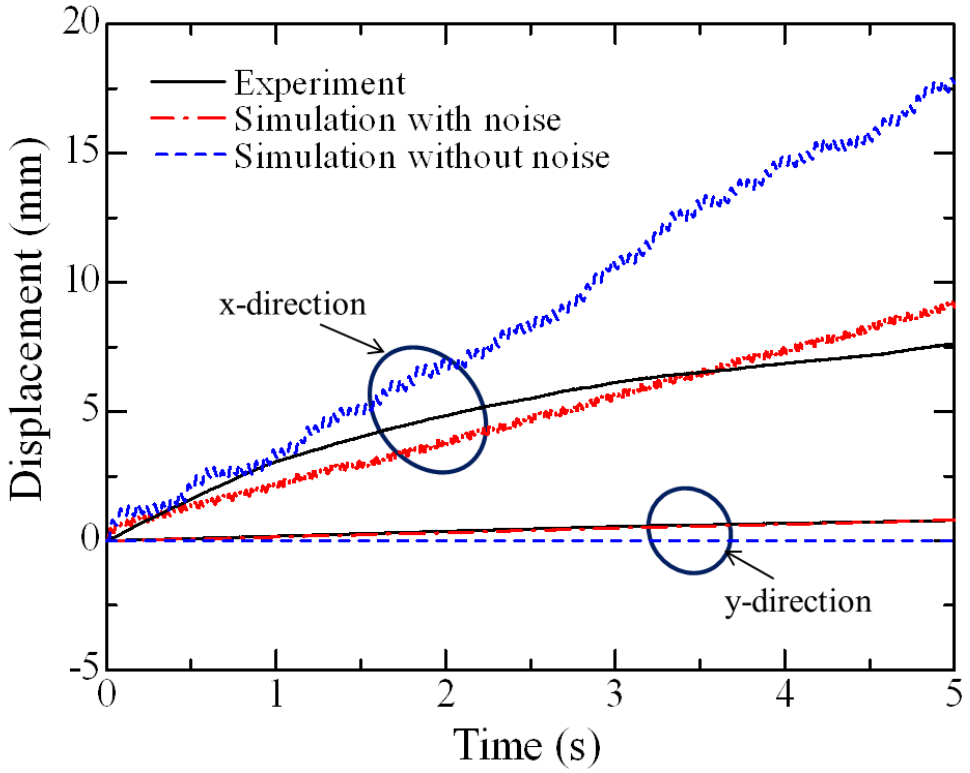

Figure 6.13 Ensemble averaged displacement of micropart with respect to time

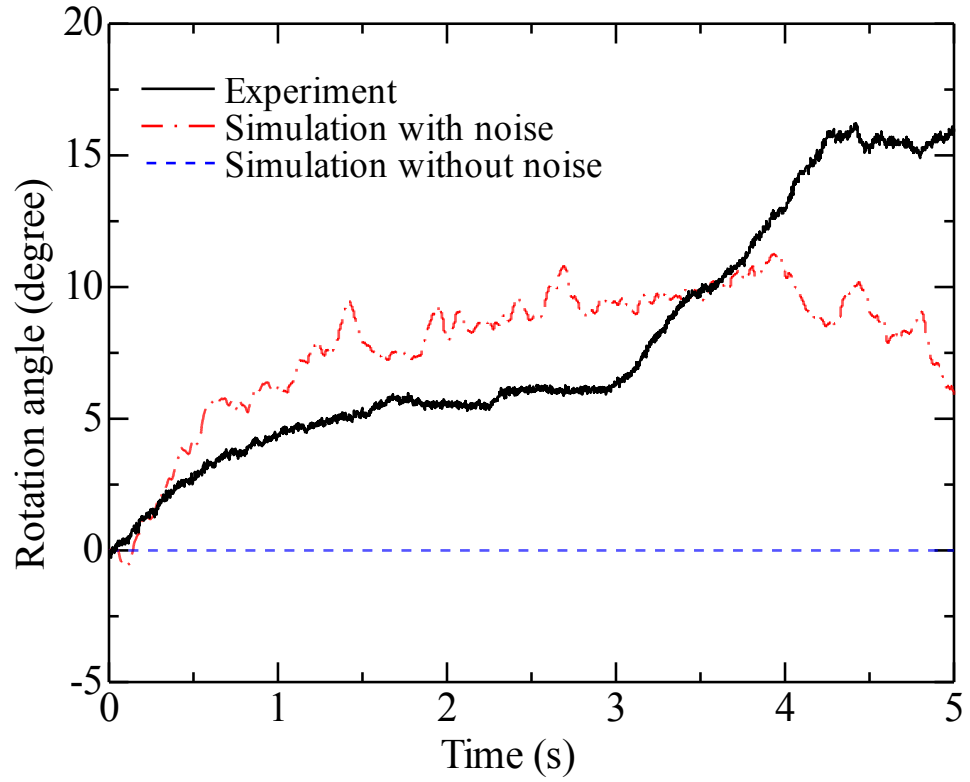

Figure 6.14 Ensemble averaged rotation angle of micropart in (x,y) plane

Since no force component exists in the *y*-direction and the force component in the *x*-direction is equal for the four hemispheres in the model without the roughness effect, the rotation angle of the micropart is zero, as shown in Fig. 6.14. In contrast, the model with the roughness effect predicts the orientation of the micropart well. The difference in the rotation angle between the simulation and experiment may be due to inaccurate modeling of the roughness of the saw-tooth surface.

6.3.2 Comparison of experiments and simulation with effect of air drag

We have numerically and experimentally showed that microparts can be transported in one direction on a symmetrically vibrated asymmetrical saw-tooth surface with effect of roughness surface. However, the simulation model overestimated the feeding velocity of the microparts, particularly for those that are sub-millimeter-sized. In this work, we include air drag and study its effect on feeding velocity of sub-millimeter-sized microparts. The amplitude of the symmetrical vibration applied to the surface as a function of exciting frequency for the model is empirically formulated from the experiment data. The model is applied to simulate the response of the microparts against the exciting frequency for several ratios of the microparts' length to the pitch of the saw-tooth. The attained results show that the model with air drag predicts well the behavior and magnitude of the feeding velocity in comparison with experiment data, while the model without air drag overestimates the velocity. We conclude that air drag plays important role in motion of microparts.

6.3.2.1 Amplitude of the vibrating saw-tooth surface

In the experiment equipment, the surface is vibrated by an actuator under sinusoidal voltage. To obtain the amplitude of the vibrating surface A, we attach a white point on the surface to track the motion of this point by PTV method in flow in Chapter 3. Figure 6.15 shows the time-dependent amplitude of the surface with the exciting frequency of 100 Hz. Although the driving voltage to the actuator is sinusoidal, the amplitude has numerous supposed frequencies. Therefore, it is difficult to accurately determine the amplitude by the direct observation from time-dependent series. Fortunately, by the use of Fourier transform shown in Fig. 6.16, we observe that the main contribution to the amplitude is from the frequency of 100 Hz and the other frequencies are the white noise.

It implies that the peak at 100 Hz is the amplitude, for instance, about 0.025 mm in this case.

Figure 6.17 plots the response of amplitude to the exciting frequency. The amplitude increases to a certain frequency and then decreases with increasing frequency. This behavior of the amplitude can be approximated as a mass-spring vibration as

$$A = \frac{C_1 \omega}{\sqrt{(\omega - \omega_0)^2 + (2C_2\omega)^2}}, \qquad \textbf{(6.22)}$$

where the coefficients C1, ω0, and C2 are the constants to determine, respectively, the amplitude, the resonant frequency, and damping of the response of the microparts. These coefficients are obtained by using a nonlinear curve fitting technique.

6.3.2.2 Response of feeding micropart velocity

In the following discussion, we consider only the time and ensemble averaged feeding velocity of the microparts, and for short: averaged velocity. To compute averaged velocity, the experiment for a certain frequency is repeated eight times. The empirical Eq. (6.22) is used to supply amplitude of the surface to evaluate driving force for the simulation model.

Figures 6.18 and 6.19 plot the variation of average velocity with driving frequency for the cases of the ratio *l/p* of 4 and 10, respectively. The solid, dashed, and dashed dot lines represent fitting data by Eq. (6.22) for the experiment and simulations with and without air drag, respectively. The simulation with air drag force predicts well the averaged velocity and resonant frequency in comparison with the experiment. For instance, the resonant frequencies about 125 Hz for both *l/p* values and the maximum velocities of 12.5 mm/s for *l/p* = 4 and 20.0 mm/s for *l/p* = 10 are obtained by both simulation and experiment. In contrast, the averaged velocities predicted by the simulation without air drag force for both *l/p* are larger by two and three times than experiment results. Furthermore, the resonant frequencies are overestimated by the model without air drag. These discrepancies imply that the air friction plays an important role for sub-millimeter-sized microparts.

Additionally, as shown in figures, the width of curves of the simulation with air drag are closer to those of the experiment, while the simulation without air drag produces a wider bandwidth. This indicates that simulation with air drag can predict well the damping behavior of the motion.

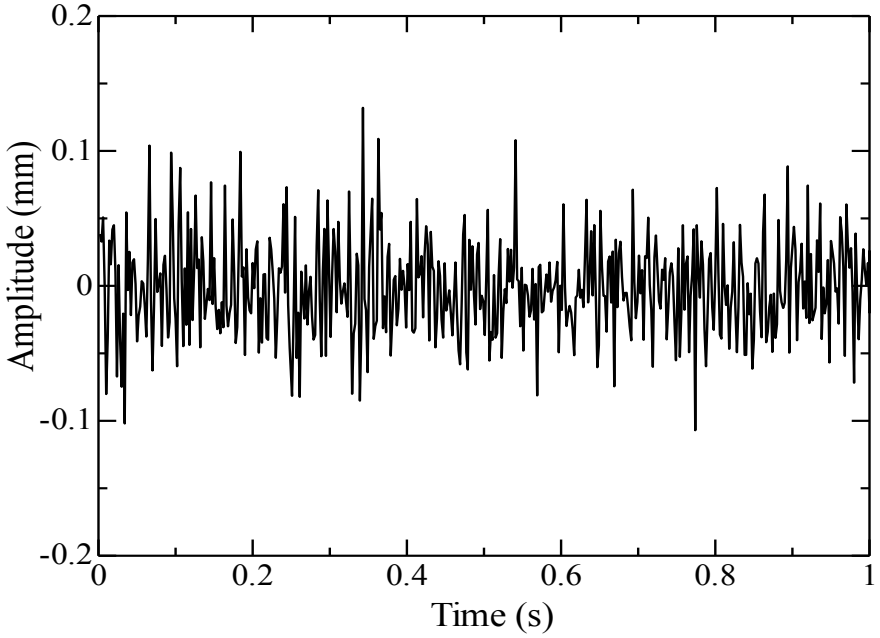

Figure 6.15 The experimental amplitude with time at 100 Hz

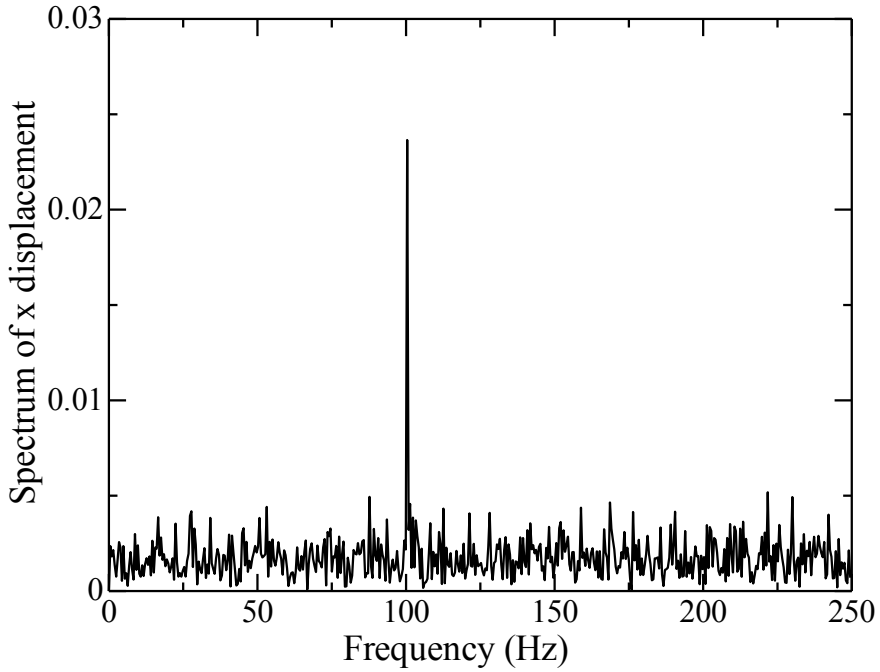

Figure 6.16 The spectrum of x displacement with frequencies at 100 Hz

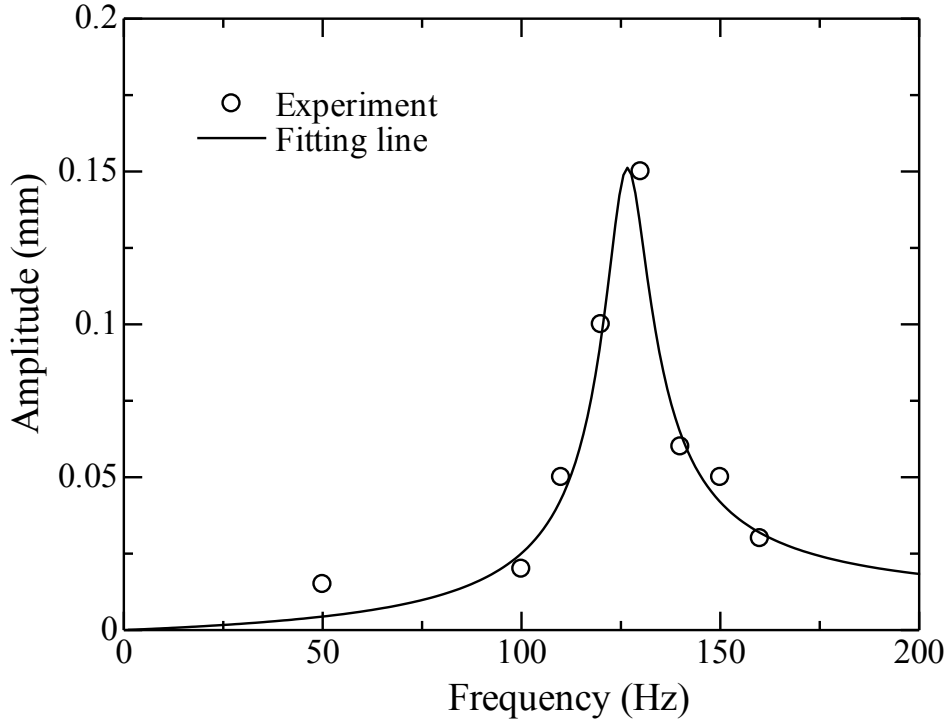

Figure 6.17 The experiment amplitude for range of frequency

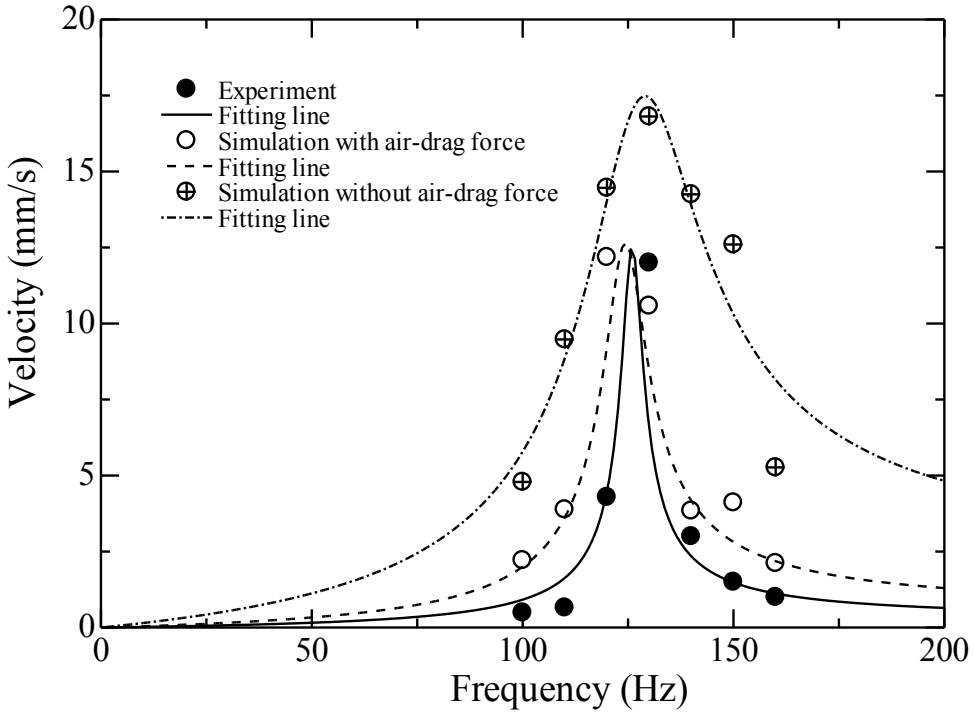

Figure 6.18 Variation of ensemble average velocity of micropart with frequency for $l/p = 4$

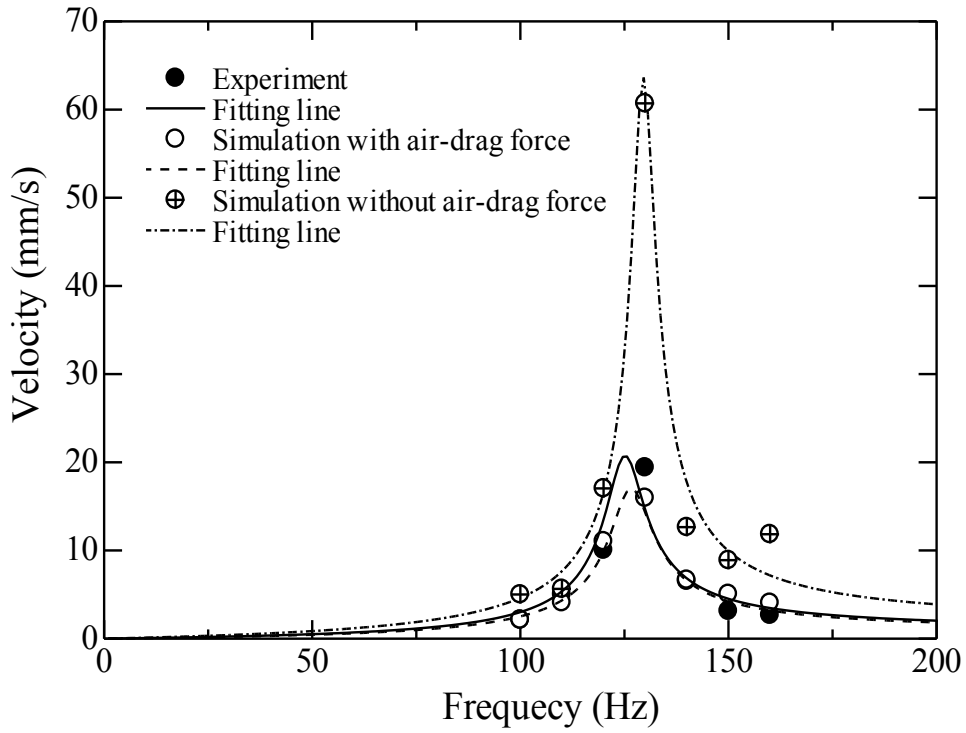

Figure 6.19 Variation of ensemble average velocity of microparts with frequency for l/p = 10

6.4 Closing remarks

In this chapter, a dynamic model which included the effect of the the roughness of the surface was developed to simulate the planar motion of a micropart. In the model, the contact between a micropart and saw-tooth surface was modeled as the contact between a number of hemispheres on the micropart and the surface. At each contact point, we generated a normal unit vector to indicate the direction of the contact force. Using this technique, the roughness effect on the motion of the micropart was considered. Additionally, by approximating a real saw-tooth profile, the effect of the saw-tooth surface roughness on adhesion was also included. The model with the roughness effect predicted well the linear motion and the orientation of the micropart. Since the present model proposed a simple method to take account the effect of surface roughness on contact force as well as adhesion force, the model could be straightforwardly applicable to the other microparts.

Moreover, a dynamic simulation model including the effect of surrounding fluid on the motion of sub-millimeter-sized micropart was also developed. The model was

verified by the comparison of feeding velocity with experiment data. The results showed that the model with fluid drag predicted well the response of micropart velocity in terms of velocity magnitude and damping behavior. In contrast, the simulation without fluid air drag overestimates the velocity of microparts and damping of the response. It indicated that the surrounding fluid plays a key role in sub-millimeter-sized microparts' motion, while the friction due to adhesion between the surface and micropart has minor contribution.

Chapter 7

Concluding Remarks and Future Work

7.1 Concluding remarks

Through this research, the use of asymmetry, anisotropic texture of the support plate in symmetry horizontal vibration as controllable small electronic components (microparts) to one direction was demonstrated. The analysis of dynamics motion of microparts along the two-dimensional asymmetric textured surface such as saw-tooth surface has been proven that the saw-tooth surface was a powerful transportation object in one direction in the micron scale world and promising applicable to automotive assembly and transportation in micro devices.

Chapter 2 introduced the experiment system as well as analyzed of micro-parts movement using the particle tracking velocimetry (PTV) method. To measure the dependent-time position and velocity of micro-parts on these surfaces, two segmentation techniques: Canny edge detection and Otsu thresholding are used in the particle tracking velocimetry method has been used.

In chapter 3, the basic principle of the asymmetric fabricated surfaces that can carry out micro-parts one direction was described.

Chapter 4 investigated the effect of surface material on the obtained the saw-tooth profile of surface and exciting frequencies on the motion of micro-parts. They are confirmed in experiment. The obtained results show that micro-parts can move better on the surfaces which have the asymmetrical structure profile closer to saw-tooth shape.

Chapter 5 studied the effect of relationship between geometry parameters of surfaces and micro-part on the motion of micro-parts. We found that the profiles of feeding micro-part against product of exciting frequency with pitch of saw-tooth are similar for

the same relative scale the length of micro-part and saw-tooth pitch. It indicates that smaller pitch maybe creates smaller asymmetric force on the micro-part.

Chapter 6 conducted the governing equations of dynamic motion micro-part on a saw-tooth surface. In a simulation, contact between the micro-part and the saw-tooth surface is assumed to be the contact between a number of hemisphere on the micro-part and the surface, which results in either a point contact or slope contact. The effect of the saw-tooth surface roughness on the contact force at each contact point is modeled as a field of random normal vectors. In addition, the effect of air drag is considered in the model to simulate for sub-millimeter sized part. The results show that the model can describe the motion modes of a micro-part. Furthermore, the numerically produced two linear motions agreed well with the experimental data.

7.2 Future work

7.2.1 Present research related to research plan

The development of the microparts feeder continues with the goal of automatic assembly and transportation on the microscale. For example, a prototype model of the medical microrobot has been developed by a researcher from Japan's Ritsumeikan University to cure cancer without surgery. To minimize the need for surgery, this surgical microrobot affixes diverse types of medical devices such as microcameras, micromanipulators, various sensors, and drug delivery injectors. Therefore, the research on the control microparts in any desired directions by a single vibration has high potential applications in the future. As in this thesis, the simulations and experiments were performed to understand the behavior of microparts during feeding and to simplify the control parameters, which affect the feeding of microparts. The research will be continued in cooperation with research members at Sapporo University and Hokkaido University for a wider range of saw-tooth profiles and other asymmetrical fabricated textures. A two-dimensional model of micropart dymanics with the effect of fluid drag was achieved, describing the motion of submillimeter microparts in our study. However, the motion of microparts is assumed to be planar. Therefore, simulations in future work should include six degrees of freedom of motion, and electrostatic forces in addition to the fluid drag. Additionally, with the development of MEMS technology, we have

continued to improve the smaller pitch of the saw-tooth shape, which will be helpful to verify the expanded simulation model for the microparts. Based on this achievement, we will also continue to cover the parameters affecting the dynamics of micropart motion to understand the interactions between the microparts surfaces and the feeder. This knowledge is critical to control the direction of the microparts by a single vibration. The present research aims to advance the quality to textured surfaces by developing an effective microtexture machining method that is easily adaptable to an industrial manufacturing environment.

7.2.2 Purpose of proposed research

The ultimate goal of this research is to develop an intelligent automatic micropart assembly system, including a surface that integrates high accuracy and simplicity to control functional surface depending on the desired target and direction of the micropart, as shown in Fig. 7.1. The system will assemble parts for various requirements in industry through computer control of the vibration amplitude/frequency of the texture.

Combining several textured shapes such as parallel, radial, and circular shapes with different pitches, multifunctional surfaces will be developed for an automatic assembly (Fig. 7.2).

For example, in station 1, the microparts move straight along aline. Next, when combined with an excited vibration feeder, the microparts can go – and – stop to an exact position in station 2 to perform automatic assembly tasks. Finally, the assemble microparts reach station 4 and turn in different directions for a designated application in industry.

The development of this automatic assembly system will fulfill the requirements of a high-flexibility and high-reliability system that has the following functionalities: controlling movements; allowing the microparts to separate from one another, and assembling with high-precision technologies for mini- and microparts. The system is easy to use and configure. Furthermore, the fabricated flexible textured surface using MEMS technologies allows for further applications of microparts feedings for large variety of components.

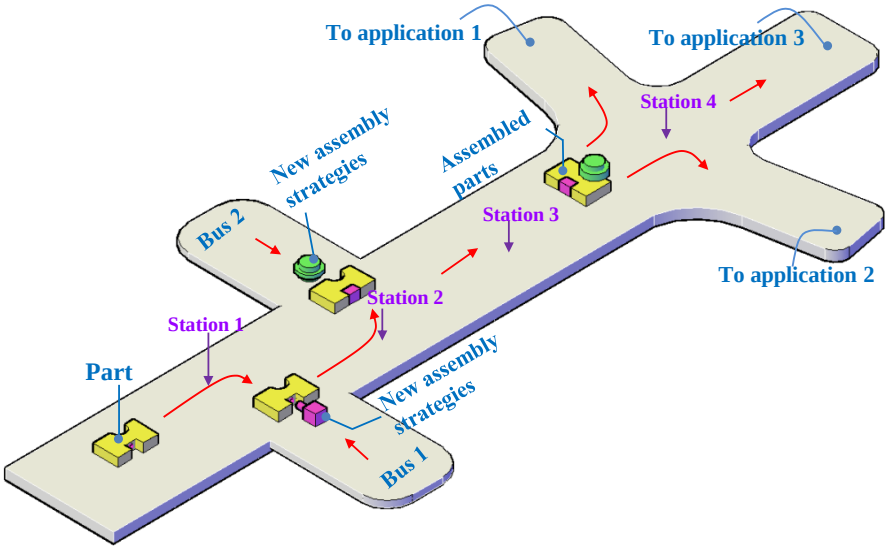

Figure 7.1 Automatic assembly system in industry

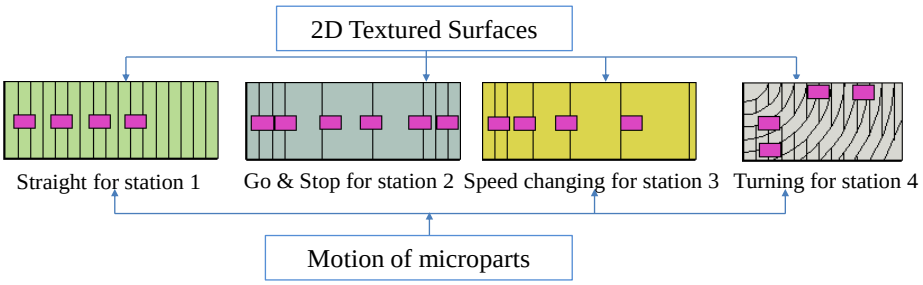

Figure 7.2 Development of multiple functional surfaces for microparts feeder with simple planar symmetric vibration.

Bibliography

B. K. A. Ngoi, L.E.N. Lim and S. S. G. Lee, 1995 “Analyzing the Natural Resting Aspects of a complex Part”, International Journal of Production Research, Vol. 33 No 11, pp. 3163-3172.

G. P. Maul and M. B. Thomas., 1997 “A systems model and simulation of the vibratory bowl feeder,” J. Manuf. Syst., vol. 16, no. 5, pp. 309–314.

S. Okabe and Y. Yokoyama., 1981 “Study on vibratory feeders: Calculation of natural frequency of bowl-type vibratory feeders,” ASME J. Mech. Des.,vol. 103, pp. 249–256.

D. Morrey and J. E. Mottershead., 1986 “Modelling of vibratory bowl feeders,” Proc. Inst. Mech. Eng. Part C, Mech. Eng. Sci., vol. 200, no. C6, pp. 431–437.

J. C. Levy., 2001 “Study of the Probabilities of the Natural Resting Aspects of Small Parts in a Bowl Feeder” Thesis M.S. University of Puerto Rico, Mayaguez

K.-F. Bohringer, and H. Choset, eds., 2000 Distributed Manipulation, Kluwer Academic Publishers.

R. N. Barnes., 1992 “A novel design of a vibratory feeder incorporating an integral cut off valve,” in Proc. Int. Conf. Bulk Mater. Handling Transp, pp. 315–319.

P. U. Frei., 2002 “An intelligent vibratory conveyor for the individual object transportation in two dimensions,” in IEEE/RSJ International Conference on Intelligent Robots and Systems, pp. 1832–1837.

P. Umbanhowar, K. M. Lynch., 2008 “Optimal vibratory stick-slip transport,”IEEE Transactions on Automation Science and Engineering, vol. 5, no. 3, pp. 537-544.

P. Umbanhowar, H. T. Vose, A. Mitani, S. Hirai and K. M. Lynch., 2012 “The effect of anisotropic friction on vibratory velocity fields”, IEEE International Conf. on Robotics and Automation, USA.

Bibliography

Y. Komari., 1993 “Characteristics of a Superconducting Linear Actuator Using High-T, superconductors and the Control for driving”. Cryogenic Engineering. pp.167-173, ~01.28, w0.3.

T. Iizuka *et al.*, 1994 “A Micro X-Y-theta Conveyor by Superconducting Magnetic Levitation,” in IEEE Symposium on Emerging Technologies and Factory Automation, ETFA’94, IIS The University of Tokyo, pp. 62–67.

Y. Fukuta *et al.*, 2003 “Pneumatic two-dimensional conveyance system for autonomous distributed MEMS,” in The 12th International Conference on Solid State Sensor, Actuor and Microsystems, Boston, pp. 1019–1022.

Y. Fukuta, Y.-A. Chapuis, Y. Mita, H. Fujita., 2006 “ Design, fabrication and control of MEMS-based actuator arrays for air-flow distributed micromanipulation,” IEEE Journal of Microelectromechanical Systems 15, pp. 912–926.

S. Konishi and H. Fujita, 1994 “A conveyance system using air flow based on the concept of distributed micro motion systems,” IEEE/ASME J. Microelectromech. Syst., vol. 3, no. 2, pp. 54–58.

S. Konishi *et al.*, 1998 “Experimental investigation of distributed conveyance system using air flow,” in Proc. Int. Symp. Micro Mech. Human Sci., pp. 195–200.

S. Konishi, Y. Mizoguchi, and K. Ohno, 1999 “Development of a non-contact conveyance system composed of distributed nozzle units,” in Proc. 7th Int. Workshop Emerging Technol. Factory Autom., pp. 593–598

M. Arai, Y. Fukuta, A. Tixier, Y. Mita and H. Fujita., 2002 “An air-flowactuator array realized by bulk micromachining technique,” in Proc. IEEJ 19th Sensor Symp., pp. 447–450.

F. M. Moesner and T. Higuchi., 1995 “Devices for Particle Handling by an AC Electric Field,” IEEE Micro Electro Mechanical Systems, MEM’s 95, Proceeding, pp 66-71.

G. Fuhr, R. Hagedorn, T. Muller ., 1999 “Linear motion of dielectric particles and living cells in microfabricated structures induced by traveling electric fields,” in Proc. IEEE Micro Electro Mech. Syst., pp. 259–264.

Bibliography

M. Paris, Y. Haddab, and P. Lutz., 2008 “Practical characterization of the friction force for the positioning and orientation of micro-components,” IEEE IROS, International Conference, pp. 931 – 936.

E. Benes, M. Gröschl, S. Radel, C. Hauser, H. Böhm, H. Nowotny., 2005 "New simple mathematical model for the separation performance of ultrasonic cell filters", Proc. 2nd Congress of Alps-Adria Acoustics Association and 1st Congress of Acoustical Society of Croatia, Opatija, Croatia, M. Horvat, K. Jambrosic, Eds., Acoustical Society of Croatia, Zagreb, pp. 14-17A.

A. Haake and J. Dual., 2003 “Particle positioning by a two- or three- dimensional ultrasound field excited by surface waves,” in WCU, Paris.

J. W. Suh, R. Bruce Darling, K. Bohringer, B. Donald, H. Baltes, and G. Kovacs., 1999 “CMOS Integrated ciliary actuato array as a general purpose micromanipulation tool for small objects,” Journal of Microelectromechanical Systems, vol. 8, no. 4, pp. 483–496.

J. Fleischer, S. Herder, U. Leberle., 2011 “Automated supply of micro parts based on the micro slide conveying principle,” CIRP Annals-Manufacturing Technology, vol. 60, issue 1, pp. 13-16.

Y. K. Kim, M. Katsurai, and H. Fujita., 1989 “A proposal for a superconducting actuator using the meissner effect,” Sens. Actuators, vol. 20, pp. 107–112.

S. H. Chang and T. W. Yang., 2000 “Dynamics of a piezoelectrically actuated vibratory feeder,” in Proc. ASME Des. Eng. Tech. Conf., pp. 341–347.

Y. Ting, H-C. Jar, C-Y. Lin, and J-S Huang., 2005 “A new type of parts feeder driven by bimorph piezo actuator,” Ultrasonics, vol. 43, pp. 566–573.

Y. Ting, H-C. Jar, C-Y. Lin, and J-S Huang., 2002 “Analysis and design of a four-bar linkage type of vibratory parts feeder driven by piezoelectric actuator,” in Proc. ASME Des. Eng. Tech. Conf., vol. 2, pp. 43–50.

W. Zesch, R. BLuchi, and R. Siegwart, 1995“Inertial mechanisms for positioning microobjects: Two novel mechanisms,” in Proc. SPIE Conf. Microrobots Micromech. Syst., pp. 80–88.

Bibliography

T. Higuchi, Y. Yamagata, K. Furutani, and K. Kudoh, 1990 “Precise positioning mechanism utilizing rapid deformations of piezoelectric elements,” in Proc. IEEE Micro Electro Mech. Syst., pp. 222–226.

A. Codourey *et al.*, 1995 “A robot system for automated handling in micro world,” in Proc. IEEE/RSJ Int. Conf. Intell. Robots Syst., vol. 3, pp. 185–190.

H. A. Francisco, K. Koeneke, and J. Wallace, 1991 “Correlation of surface contamination introduced by feeding equipment of electrical contact resistance,” in Proc. 37th IEEE Holm Conf. Oct. 6–9, pp. 261–270.

R.-P. Berretty *et al.* and K. Goldberg, 1999 “Trap design for vibratory bowl feeders,” in Proc. IEEE Int. Conf. Robot. Autom., vol. 4, May, pp. 2558–2563.

G. Maul and N. Jaksic, 1994 “Sensor-based solution to contiguous and overlapping parts in vibratory bowl feeders,” J. Manuf. Syst., vol. 13, no. 3, pp. 190–195.

S. Okabe, Y. Kamiya, K. Tsujikado, and Y. Yokoyama., 1985“Vibratory feeding by non-sinusoidal vibration-optimum wave form”, J. Vib. Acoust. Reliab. Des., Vol. 107, pp. 188-195.

D. Reznik and J. Candy., 1998 “A flat rigid plate is a universial planar manipulator,” in IEEE International Conference on Robotics and Automatic, pp. 1471-1477.

D. Reznik and J. Candy, 2011 “C’mon part, do the local motion!” in IEEE International Conference on Robotics and Automatic, pp. 2235-2242.

G. Boothroyd., 2005 “Assembly Automation and Product Design,” Marcel Dekker, Inc., pp 1992 – 413.

A. Mitani, N. Sugano, and S. Hirai., 2006 “Micro-parts feeding by a sawtooth surface”, IEEE/ASME Trans. Mechatronics, Vol. 11, No. 6, pp. 671-681.

A. Mitani, N. Sugano, and S. Hirai., 2007 “Feeding of submillimeter-sized microparts along a saw-tooth surface using only horizontal vibration: Analysis of convexities on the surface of microparts”, in Proc. IEEE/ASME Int. Conf. Automation Science and Engineering, Scottsdale, AZ, USA, pp. 69-76.

A. Mitani and S. Hirai., 2008 “Analysis of contact between feeder surface and microparts based on measurements for microparts feeder using an asymmetric

surface", in Proc. IEEE/ASME Int. Conf. Automation Science and Engineering, Key Bridge Marriott, Washington DC, USA, pp. 720-725.

A. Mitani and S. Hirai., 2009 "Evaluation of asymmetric microfabricated surfaces using femtosecond laser process for microparts feeding", in Proc. IEEE Int. Conf. Mechatronics, Malaga, Spain.

A. Mitani and S. Hirai., 2011 "Feeding submillimeter microparts using an asymmetric fabricated surface with symmetric vibrations: Examination of influence of feeder surface materials on feeding", www.scientific.net/KEM, Vol. 467-469, pp. 1297-1302.

A. Mitani and Y. Matsuo; 2011 "Feeding of Microparts Along an Asymmetric Surface Using Horizontal and Symmetric Vibrations – Development of Asymmetric Surfaces using Anisotropic Etching Process of Single-Crystal Silicon -", Procs. of IEEE International Conference on Robotics and Biomimmetics, DVD-ROM, TP-P291.

N. Otsu., 1979 "A Threshold Selection Method from Gray-Level Histograms," IEEE Transactions on Systems, Man, and Cybernetics, Vol. 9, No. 1, pp. 62-66.

P. K. William., "Digital Image Processing", Third Edition, pp. 597-605.